UNIVERSITY OF CALIFORNIA
RIVERSIDE

Impact of Fluid and Interaction Forces on the Fate and Transport of Nanomaterials and Bacteria in Aqueous Systems

A Dissertation submitted in partial satisfaction
of the requirements for the degree of

Doctor of Philosophy

in

Chemical and Environmental Engineering

by

Daniel White

September 2021

Dissertation Committee:
Dr. Sharon L. Walker, Chairperson
Dr. Cesunica E. Ivey
Dr. Marko Princevac
Dr. Kelley C. Barsanti

The Dissertation of Daniel White is approved:

_____

_____

_____

_____

Committee Chairperson

University of California, Riverside

Acknowledgements

I would like to thank my committee members: Professor Cesunica E. Ivey, Professor Marko Princevac, and Professor Kelley C. Barsanti. Dr. Ivey prepared studious questions for my advancement to candidacy exam that provided clarifying insight into merits and limitations of my research. She traversed social barriers to make herself available for professional guidance and emotional support. Dr. Princevac gave astute feedback on tedious details of my fluid dynamics simulations at a formative time in my research. He presented himself as an ally to me in a professional context where many professors might uphold their professional superiority. Dr. Barsanti was a gracious leader and filled important gaps in my professional experience.

I am especially thankful to the Chairperson of my committee, my advisor, Dean Sharon L. Walker. Without Dr. Walker's generous support, I likely would not have finished my PhD. Dr. Walker believed in me in spite of a rough start to my PhD, and she treated me like the professional that I would become one day. Dr. Walker's flexible leadership gave me the independence I needed to make abstract advances in my research, which are a major component of my research's intellectual merit. Her striking familiarity with my strengths and weaknesses was embodied in forward-looking advice on my professional pursuits. Dr. Walker's investments in me went far beyond supporting my technical training. She strived to create a comprehensive experience that would equip me to be a well-balanced PhD graduate.

I am tremendously grateful to Director Ian M. Marcus, who served as the direct supervisor for my dissertation research. Few PhD students receive the quality of training that Dr. Marcus gave me in writing, presentation, scientific investigation, and professional interactions. Dr. Marcus was a steady and reliable source of help when I found myself in unfamiliar or overwhelming situations. His mentorship and support were crucial to my success. His selfless devotion and our frank communication were lifelines that I utilized several times. I hope I can emulate Dr. Marcus' humility in my future leadership roles.

A special thanks goes to Professor M. Caroline Roper, who served as my co-advisor for over two years. Dr. Roper accepted me into her research group and provided valuable feedback on my research manuscripts. She contributed to my laboratory training, provided space for me to practice presenting my research, and provided administrative support for my non-traditional PhD studies. She organized several experiences that I had with practical aspects of crop diseases that I studied, including greenhouse work and a trip to a vineyard in Temecula. At the vineyard, I gained tangible experience that linked with what I read in research literature, and I interacted with European Scientists that are part of a growing field related to my research focus.

I am grateful to many staff and faculty that enhanced my time at UCR. The leaders in the NICE program that funded me supported my academic freedom and organized workshops for my professional development. I knew that I could go to Professor Eamonn Keogh, Professor Christian Shelton, or Melissa Jaunal if I needed help. The staff in Graduate Division and the Career Center provided great resources for my professional development. I feel much more confident as an emerging professional because of the

variety of valuable resources that I took advantage of in my time at UCR. Director Hillary Jenks and Coordinator Yelda Serin went above and beyond to support me. Thank you to the staff of the Grad Slam competition, which stands out as a particularly important professional development activity. Thank you to people in the Graduate Writing Center and Mitch Boretz, who have collectively helped me make great improvements to my writing skills: Kelly Bowker, Lauren Hammond, Christina Trujillo, Maxwell McCoy, William Ota, and Iris Blake. I am grateful to Associate Dean Ertem Tuncel for his diligence and patience in supporting the completion of my PhD. Thank you to the UCR Ombudsman for providing confidential and useful guidance. I highly recommend that other graduate students take advantage of this resource if there is any chance that the Ombudsperson could provide helpful advice.

I thank many colleagues, friends, and experienced scientists/professionals that have contributed to my journey. Present and former students and scholars from the Walker Lab have contributed to my journey: Dr. Drew Story, Julianne Rolf, Dr. Alicia Taylor, Professor Jacob Lanphere, Dr. Holly Mayton, Dr. Travis Waller, Dr. Chen Chen, and Dr. Nichola Kinsinger. Present and former students and scholars from the Roper Lab contributed to my journey: Christopher Drozd, Dr. Nichole Ginnan, Dr. Alex Blacutt, Dr. Flávia Campos Vieira, Gretchen Heimlich, Dr. Alicia Gómez, Dr. Jeannette Rapicavoli, Dr. Barbara Jablonska, Biagio DiSalvo, Polrit Viravathana, and Claudia Castro. I thank colleagues and senior scientists that I had valuable discussions with about my work: Professor Rodrigo Almeida, Dr. Elaine A. Backus, Professor Leonardo De La Fuente, Professor Andrew McElrone, David Haviland, and Nancy Walker. I thank present and

former members of the Elimelech Laboratory at Yale University: Professor Menachem Elimelech, Professor Mohan Qin and her husband Professor Haoran Wei, Cassandra Porter, and Masashi Kaneda. I thank Professor Haizhou Liu for being my first PhD advisor at UCR. I thank the chairs and co-chairs of the 2022 Gordon Research Conference and Seminar on Food/Ag/Nano for teaching me how to be a conference co-chair. I thank scientists from the 2018 Gordon Research Conference on Food/Ag/Nano whose interactions were particularly meaningful: Anthony Cartwright, Professor Yuxiong Huang, Dr. Ying Wang, Professor Paret Mathews, and Professor Joel Pedersen. I thank scientists and other professionals that have contributed to my journey: Dr. Gongde Chen, Cheng Tan, Touhid Bin Anwar, Professor Edward Jones (EJ), Professor Patricia Manosalva, Adrienne Thomas, Kathy Cocker, Deanna Vorhees, Professor Phillip Christopher, Professor Rana Tayyar, Professor Mary Legner, Professor Samantha (Sam) Ying, Professor Jirka Šimunek, John Clark, Professor Frederic Guittard, Professor Heather Smith, Dr. Nilwala Abeysekara, Aidan Shands, Paco Franco-Navarro, and Professor Wenbo Ma.

The text of this dissertation, in part, is a reprint of the material as it appears in the 2019 Environmental Science: Nano article titled *Influence of nano-CuO and-TiO_2 on deposition and detachment of Escherichia coli in two model systems* (H. M. Mayton, D. White, I. M. Marcus and S. L. Walker, *Environ. Sci.: Nano*, 2019, **6**, 3268 **DOI:** 10.1039/C9EN00857H adapted by permission of the Royal Society of Chemistry). This published article forms the basis of Chapter 2 and Appendix A of this dissertation, with modifications to make it fit into the formatting and structure of this dissertation. The first author Dr. Holly M. Mayton listed in that publication wrote most of the article text,

performed the parallel plate flow cell experiments, calculated the DLVO predictions, selected the nanoparticles and bacteria to be used in the experiments, performed some of the zeta potential measurements, and directed the SEM imaging. The co-author Daniel White performed the sand column experiments, performed some of the zeta potential measurements, and wrote much of the content about sand column experiments. The co-author Dr. Ian M. Marcus supervised research activities, provided administrative support, and edited the manuscript. The co-author Dr. Sharon L. Walker supervised research activities, provided administrative support, and edited the manuscript. The work was supported in part by the National Science Foundation IGERT: WaterSENSE - Water Social, Engineering, and Natural Sciences Engagement Program (award number GE-1144635), as well as NSF UC-CEIN award #1266377. The authors thank the staff of the Central Facility for Microscopy and Microanalysis at UC Riverside where scanning electron microscopy was performed.

The text of this dissertation, in part, is a reprint of the material as it appears in the 2021 Scientific Reports article titled *Functional foregut anatomy of the blue–green sharpshooter illustrated using a 3D model*. This published article forms the basis of Chapter 3 and Appendix C of this dissertation, with modifications to make it fit into the formatting and structure of this dissertation. Appendix B of this dissertation is based on material that was removed from an early draft of the same publication. The following is a quoted description of the author contributions listed in that publication (Daniel White = D.W., Elaine A. Backus = E.A.B., Ian M. Marcus = I.M.M., Sharon L. Walker = S.L.W., and M. Caroline Roper = M.C.R.): “D.W. created the 3D model and the code for model

visualization. D.W. and E.A.B. conceived and designed the study. S.L.W. and M.C.R. provided equipment for comfortable workflow. D.W. and E.A.B. conducted the literature searches, investigated the precedence of anatomical terminology, and co-wrote the manuscript. D.W., E.A.B., I.M.M., S.L.W., and M.C.R. conceptualized aspects of the manuscript and reviewed/edited the manuscript. E.A.B. validated methodologies. S.L.W. and M.C.R. administrated the cooperation of authors."

This work was supported by the National Science Foundation [Grant No. 1631776] and the United States Department of Agriculture National Institute of Food and Agriculture [Grant No. 2019-67014-29358]. The contributions of E. A. B. were made possible by in-house funds from USDA-ARS (appropriated Project No. 2034-22000-010-00D). Thank you to J. Rapicavoli for generously providing the SEM images showcased in Chapter 3 of this dissertation. One of these SEM images was adapted from a previous publication, as noted in the relevant figure captions (Reprinted with permission; copyright © American Society for Microbiology, [Appl. Environ. Microbiol. 81, no. 23 (2015): 8145–8154 10.1128/AEM.02383–15]). The image of an insect in one of the dissertation figures is a derivative of an image used under CC BY-NC (Emilie Bess, USDA APHIS PPQ, Bugwood.org). The microscope image in Appendix C was modified from a published article (From Purcell, A. H., Finlay, A. H. & McLean, D. L. Pierce's disease bacterium: mechanism of transmission by leafhopper vectors. *Science* 206, 839-841 (1979). Reprinted with permission from AAAS.). The micro-CT measurement in Appendix C was modified from a published article (Reprinted from Journal of Insect Physiology, Vol 120, Emanuele Ranieri, Gianluca Zitti, Paola Rioloa, Nunzio Isidoro, Sara Ruschioni, Maurizio Brocchini,

Rodrigo P.P. Almeida, Fluid dynamics in the functional foregut of xylem-sap feeding insects: A comparative study of two Xylella fastidiosa vectors, 103995, Copyright 2020, with permission from Elsevier.).

The text of Chapter 4 of this dissertation is based on a manuscript that is in preparation for submission. The first author Dr. Ian M. Marcus supervised the research, edited past drafts of the manuscript, and will write future drafts of the manuscript. The co-author Daniel White completed the simulations, created the figures, and wrote past drafts of the manuscript. The co-author Dr. Elaine A. Backus will edit future drafts of the manuscript. The co-author Dr. M. Caroline Roper supervised the research, edited past drafts of the manuscript, and will edit future drafts of the manuscript. The co-author Dr. Sharon L. Walker supervised the research and will edit future drafts of the manuscript. The colleague Dr. Rodrigo P. Almeida provided discussion about precibarial valve function, *Xylella fastidiosa* transmission, and the colonization maps that were derived from a paper he authored. The colleague David Haviland provided clarifying discussion about agricultural practices in vineyards. The colleague Dr. Andrew J. McElrone provided discussion about grapevine physiology. This work was supported by the National Science Foundation [grant number 1631776] and the United States Department of Agriculture National Institute of Food and Agriculture [grant number 2019-67014-29358].

ABSTRACT OF THE DISSERTATION

Impact of Fluid and Interaction Forces on the Fate and Transport of Nanomaterials and Bacteria in Aqueous Systems

by

Daniel White

Doctor of Philosophy, Graduate Program in Chemical and Environmental Engineering
University of California, Riverside, September 2021
Dr. Sharon L. Walker, Chairperson

Bacteria transport in aqueous environments is heavily influenced by nanoscale forces that govern deposition on and detachment from environmental surfaces. Surface interaction can prevent these species from being carried long distances by fluid flow. Nuances in deposition and detachment properties of waterborne pathogenic bacteria can mean the difference between life and death or serious economic losses. In this dissertation, deposition and detachment properties of the human pathogen *Escherichia coli* O157:H7 and the plant pathogen *Xylella fastidiosa* are analyzed using a variety of engineering tools. Sand column experiments, parallel plate experiments, and thermodynamic surface interaction predictions are used to study how nanoparticles could

affect the transport of *E. coli* O157:H7 in agricultural soils. Results indicate that the presence of titanium dioxide (TiO_2) nanoparticles in agricultural waters could increase *E. coli* O157:H7 soil transport, especially during rain events. However, the presence of copper oxide (CuO) nanoparticles may decrease *E. coli* O157:H7 transport. *Xylella fastidiosa* transport in an insect-plant system was studied *in silico*. Fluid flow fields in this system were simulated and integrated with custom-made MATLAB code to predict bacteria detachment under relevant environmental conditions. Results support a model of key fluid dynamic mechanisms involved in *X. fastidiosa* spread within plants and between plants. The model can be used to investigate potential targets for fighting costly crop diseases caused by *X. fastidiosa*. The application of computational and experimental tools in this dissertation demonstrate how engineering methods can enhance analyses of bacterial transport in diverse environmental systems.

Table of Contents

List of Figures

List of Tables

Chapter 1

Introduction

1.1 Background and Motivation

The transport properties of bacteria in aqueous environments can have drastic consequences on the environment, human health, and the economy. In the systems investigated as part of this dissertation research, changes in aqueous bacteria transport could mean the difference between life and death, or they could lead to millions of dollars in agricultural losses. According to the Centers for Disease Control and Prevention (CDC), outbreaks of the bacterium *Escherichia coli* O157:H7 in the United States in 2018 lead to 121 hospitalizations and 5 deaths[1,2]. On a similar note, the multicontinental plant pathogenic bacterium *Xylella fastidiosa* is estimated to cost California over $100 million per year[3], and it has the potential to cause billions of dollars of damage in Europe over the next 50 years[4]. The spread of each of these damaging bacteria is dependent on bacterial transport properties[5-7].

Investigations of bacterial transport properties often treat bacteria as colloidal particles for modeling purposes[8,9]. Colloidal particles are 'suspended' inanimate objects with at least one dimension that is less than 1,000 nanometers[10]. Colloidal particles are not 'suspended' in a usual sense, as their small size leads to slow settling rates, so the particles remain dispersed for long periods of time. Oftentimes, gravity is not the predominant driving force of colloidal particle transport, because gravitational forces acting on particles are proportional to particle mass, and thus the third power of particle size (diameter^3 for spherical particles). Meanwhile, fluid dynamic forces are roughly proportional to the second power of particle size (diameter^2) and surface interactions are proportional to the

first power of particle size (diameter[1])[10]. Thus, the smaller the particles, the more surface interactions play a role in their fate and transport (Figure 1.1).

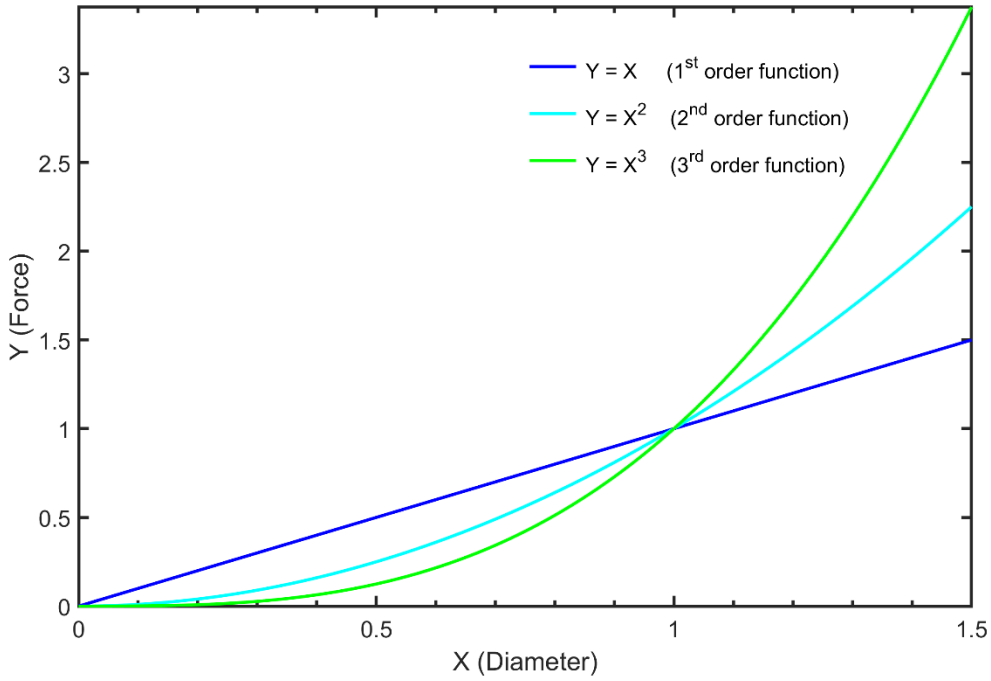

Figure 1.1 Illustration of reversing relative magnitudes among first order, second order, and third order functions. At small values of the independent variable *X*, the first order function has a larger value of *Y* than either the second order function or the third order function. In contrast, at large values of the independent variable *X*, the first order function has a smaller value of *Y* than the second order function and the third order function. This principle of reversing relative magnitudes is useful for understanding the magnitude of forces acting on colloidal particles, where the dependent variable is *Force* instead of *Y* and the independent variable is *Particle Size* instead of *X*. Since surface interaction forces are first order functions of particle size, their effects become relatively pronounced at smaller particle sizes in comparison to fluid drag forces and gravitational forces, which are roughly second order and third order functions of particle size, respectively.

Colloid surface interactions are often modeled using DLVO theory[11], which approximates particles as spheres with constant surface charges or constant surface

potentials[12]. Classic DLVO theory can be extended with additional parameters to provide better quantitative predictions of colloid adhesion[13], but DLVO theory already provides solid predictive capacity based on straightforward, fundamental experiments[10]. DLVO predictions calculate the balance between van der Waals attraction and electrical double layer repulsion (Figure 1.2A). These predictions help explain how stable colloids are kinetically stable, but not thermodynamically stable. If the stable colloidal particle in Figure 1.2B approaches within 1.1 nm of the surface, it is predicted to become kinetically unstable and undergo a thermodynamically irreversible adhesion process. However, an approach to 1.1 nm would require the particle to overcome a potential energy barrier, thus necessitating activation energy. The energy to overcome this barrier can be from various inputs into the system, including kinetic energy imparted by fluid dynamics acting on the particle. Also, this relationship between activation energy and surface interaction potential energy can be used to describe the interactions of different types of colloid-like particles, including bacteria[14].

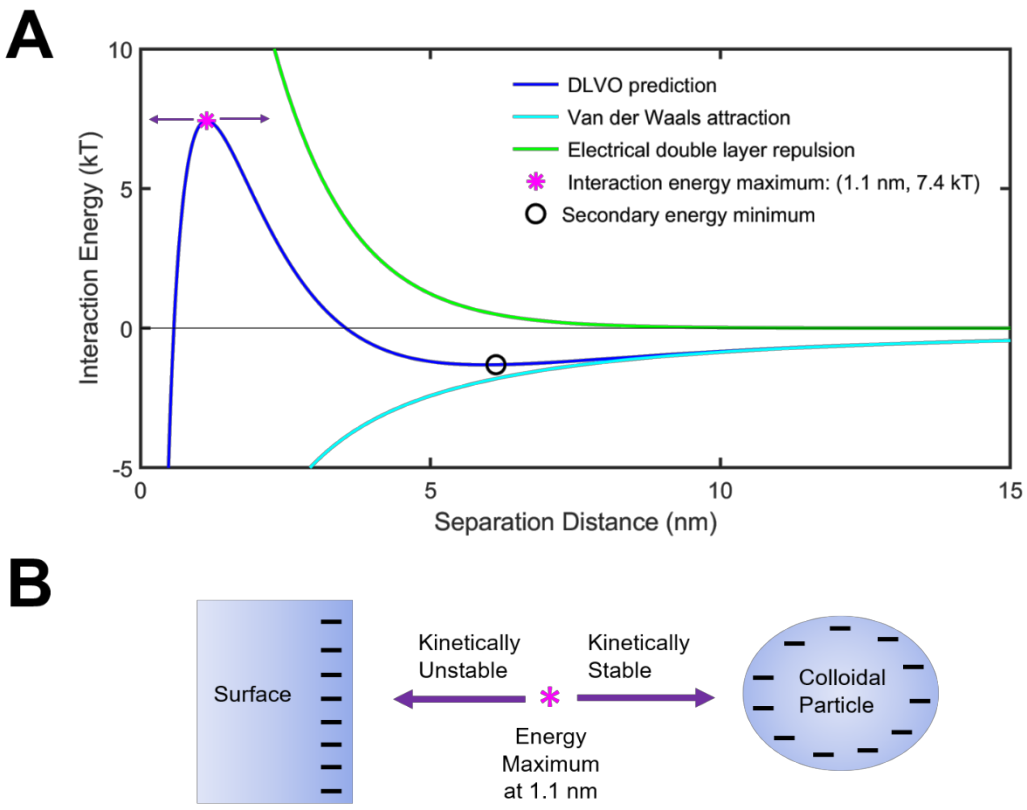

Figure 1.2 DLVO predictions calculate the balance between van der Waals attraction and electrical double layer repulsion. Potential energy is calculated for the interaction between a negatively charged colloidal particle and a negatively charged surface. A) The sum of van der Waals attraction and electrical double layer repulsion yields the predicted interaction energy as a function of separation distance. There is an interaction energy maximum and a secondary energy minimum. B) Stable colloidal particles are kinetically stable, but not thermodynamically stable. If the illustrated kinetically stable particle approaches within 1.1 nm of the illustrated surface by overcoming the interaction energy maximum (activation energy), it is predicted that the particle becomes kinetically unstable and adheres to the surface. For the sake of illustration, the following parameters were used for DLVO calculations in subfigure A: particle zeta potential = -35 mV; particle diameter = 500 nm; surface zeta potential = -45 mV; symmetric divalent salt concentration = 15 mM; Hamaker constant = $0.2*10^{-20}$ J. The equations used for the calculation are described in Appendix E.

Stagnation point flow cell experiments create conditions where fluid flow imparts kinetic energy into bacteria that enhances surface deposition (Figure 1.3A)[15]. Fluid flow in

a direction perpendicular to the deposition surface enhances both bacteria convection toward the surface and bacteria surface adhesion[16]. In contrast, parallel plate flow cell experiments promote fluid flow parallel to bacteria deposition surfaces (Figure 1.3B)[15]. This parallel flow can detach surface-adhered bacteria when kinetic energy in flowing fluid transfers to thermodynamically stable surface-adhered cells. The aforementioned bacteria transport mechanisms exemplify how kinetic and thermodynamic mechanisms involved in bacteria deposition and detachment are linked.

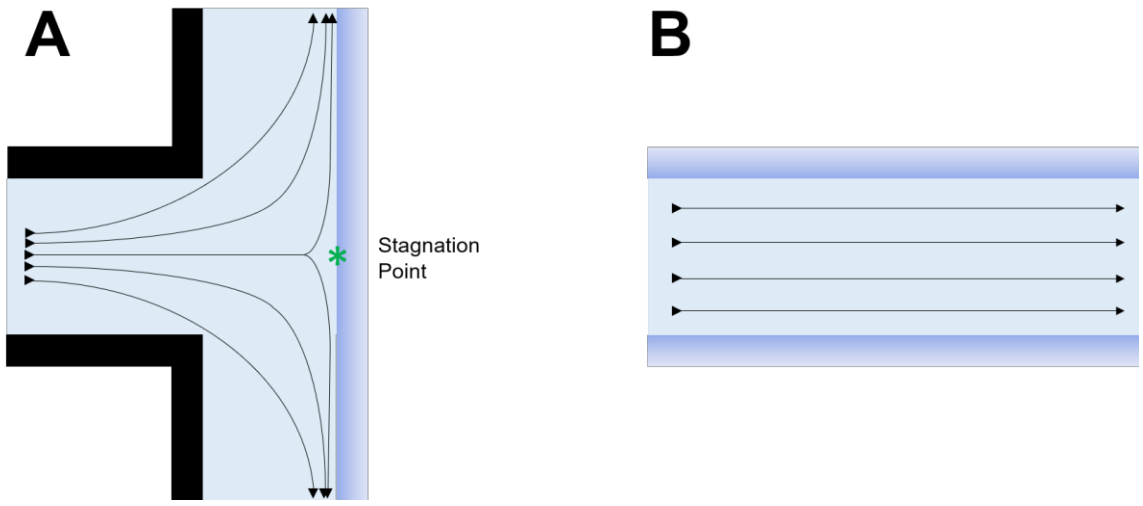

Figure 1.3 Illustration of fluid flow directions in stagnation point (A) and parallel plate (B) flow cells. In stagnation point flow cells, fluid flows toward the bacteria deposition surface. In parallel plate flow cells, fluid flows parallel to bacteria deposition surfaces.

Porous media sand column experiments involve a combination of the deposition and detachment mechanisms described above for stagnation point flow cells and parallel plate flow cells, as well as physical straining by the porous media. In sand columns at the micrometer scale, roughly spherical sand grains stack on top of each other to create

repeating geometric patterns (Figure 1.4A). These repeating geometric patterns lead to repeating patterns of fluid dynamics, which can be represented by a simplified illustration of fluid flow around a single grain of sand (Figure 1.4B). At the leading edge of the sand grain, conditions resemble those at the stagnation point in stagnation point flow cells. At the side edges of the sand grain, flow conditions resemble those in parallel plate flow cells. At the trailing edge of the sand grain, another stagnation point exists. At this trailing stagnation point, bacteria can remain loosely adhered to the sand grain if they are held in a secondary energy minimum, which can be predicted by utilizing DLVO theory (Figure. 1.2).

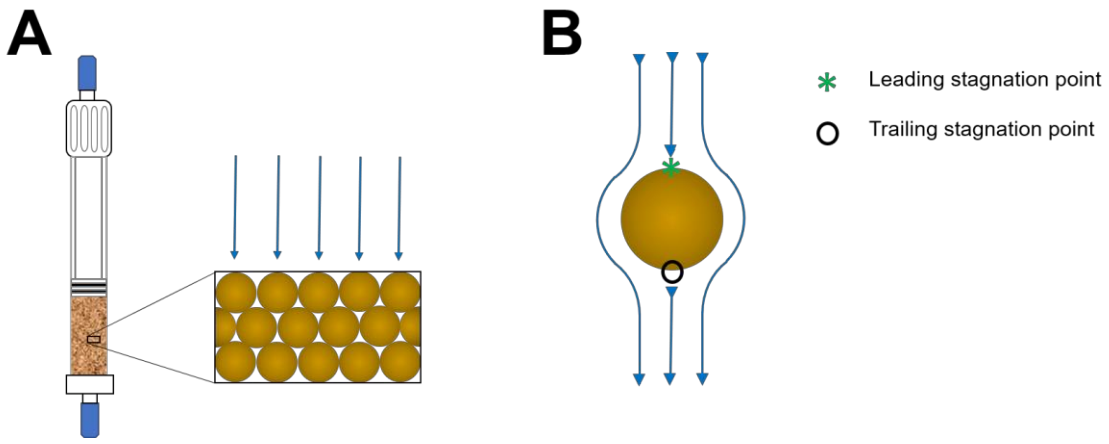

Figure 1.4 The repeating geometry (A) and simplified flow patterns (B) in sand columns. Fluid flow around roughly spherical sand grains can be roughly deconstructed because of the regularly repeating geometric packing of sand grains. At the leading edge of a sand grain, there is a stagnation point that resembles those in stagnation point flow cells. At the side edges of the sand grain, flow conditions resemble those in parallel plate flow cell experiments. At the trailing edge, there is an additional stagnation point where bacteria and nanoparticles can be retained in a secondary energy minimum, as described by DLVO theory. The leading and trailing stagnation points can also be referred to as the forward and rear stagnation points.

Thus, bacteria deposition in geometrically complex sand column experiments can be roughly estimated by summing the contributions of different transport mechanisms. This estimation can be supported through stagnation point flow cell studies, parallel plate flow cell studies, and DLVO analyses. In Chapter 2 of this dissertation, parallel plate flow cell experiment results and DLVO predictions are used to interpret the results of saturated sand column experiments. The estimation of transport mechanisms in sand column experiments in general is enhanced by regularly repeating geometric pattens in packed bed systems (Figure 1.4A).

In contrast, bacteria deposition and detachment mechanisms in systems with irregular geometries are more difficult to deconstruct into different transport mechanisms. In these cases, numerical simulations of fluid flow fields can be valuable for quantifying the forces acting on bacteria that result from fluid kinetic energy. In this dissertation, a geometrically irregular biological system is the focus of Chapters 3 & 4. In this biological system, planktonic bacteria are transferred between insects and plants via fluid flow. Blue-green sharpshooter insects feed on grapevine xylem, sucking in xylem sap and then spitting sap back into plants (Figure 1.5). Bacteria attachment to and detachment from insect and plant surfaces in this system are thought to affect the transmission of the plant pathogenic bacteria between plants and how quickly the bacteria spreads within plants.

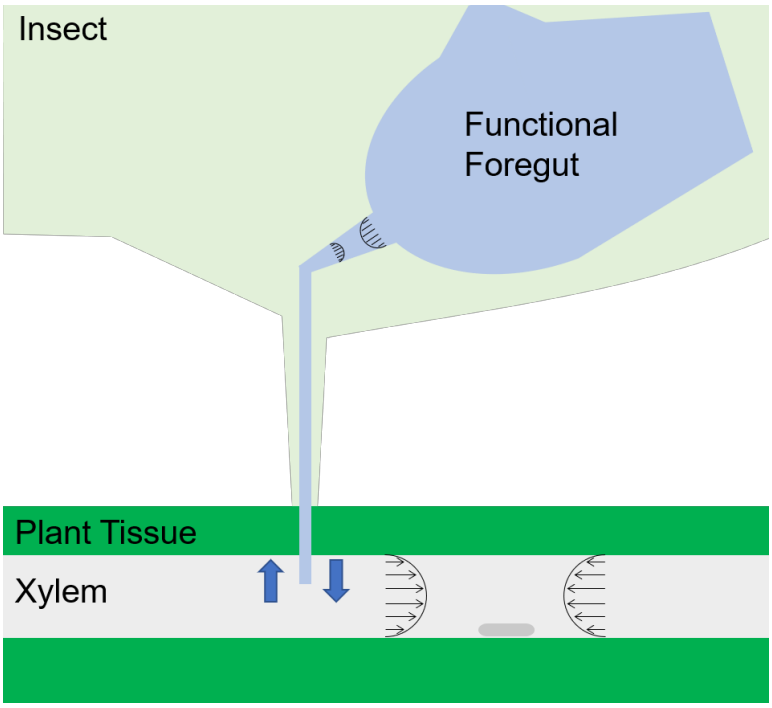

Figure 1.5 Illustration of the insect-plant system in Chapters 3 & 4. Insect vectors of *X. fastidiosa* feed on xylem sap of host plants. Bacteria cells are transported between insects and plants by fluid flow during feeding.

Prior to this dissertation research, plant pathologists and entomologists lacked tools for appreciating several of the effects of kinetics, thermodynamics, and transport phenomena on the system described in Figure 1.5. First, there was a lack of fine scale terminology for insect anatomy that could accommodate fine scale predictions of how bacteria attach and detach in this system. Second, the terminology that did exist was inconsistently used and confusingly, contained many synonyms for anatomical features. This lack of uniform terminology was a barrier to entry for researchers to contribute to the field if they were not experts in a particular subset of insect anatomy. Third, fluid dynamics simulation software that was used could not feasibly calculate drag forces acting on

surface-attached bacteria throughout an irregular geometry. This limitation hindered detachment analyses. Fourth, the same software could not create particle tracking simulations where particle-surface interaction forces work against fluid drag forces in deposition studies. In this dissertation research, a uniform terminology of insect anatomy was proposed using a one-term, one-meaning approach (Appendix B), the terminology was demonstrated to make it more accessible to multidisciplinary researchers (Chapter 3), detachment of bacteria from insect and plant surfaces was simulated (Chapter 4), and the backbone of a particle tracking simulation was created for predicting bacteria deposition considering bacteria-surface interactions applying the DLVO approach (Appendix E).

Overall, in the dissertation research presented herein, experimental and computational methods were applied to understand how bacteria fate and transport are affected by thermodynamics and kinetics, as well as momentum, mass, and heat transport. The research in Chapter 2 indicates that the presence of environmental nanoparticles could affect the distance that lethal bacteria transport in soil, possibly leading to increased or decreased contamination of water supplies in agricultural settings. DLVO predictions and sand column experimental results indicate that bacteria were retained at the trailing stagnation points of sand grains in the presence of titanium dioxide (TiO_2) nanoparticles, and that there was additional bacteria release during a simulated rain event due to altered surface interaction forces. Parallel plate experimental results and sand column experimental results suggest that bacteria deposited more readily in sand columns in the presence of copper oxide (CuO) nanoparticles, with minimal additional release during a simulated rain event. Bacteria transport was studied in a geometrically regular sand column

system in Chapter 2, while transport was studied in a geometrically irregular insect-plant system in Chapters 3 and 4 (Figure 1.5). In Chapter 3, a novel 3D model of the insect portion of the insect-plant system is illustrated. The 3D model is used to propose a uniform terminology of anatomy (Appendix B) that enhances the fine resolution bacteria detachment study in Chapter 4. Chapter 4 integrates fluid dynamic simulations, heat transfer simulations, published experimental bacteria detachment measurements, and custom-made MATLAB code to understand bacteria detachment in the insect-plant system. This contributes to a model of how fluid dynamics affect the transport of a plant pathogenic bacterium, which can be used to investigate potential targets for fighting costly crop diseases. This dissertation demonstrates how chemical engineering tools can be applied to study colloid transport in diverse environmental systems.

1.2 Aim & Scope

This dissertation research investigates how fluid dynamic and adhesive forces affect the aqueous transport of bacteria and nanoparticles in geometrically diverse 3D systems. Saturated sand column experiments were conducted to understand how nanoparticles affect the transport of *Escherichia coli* O157:H7 in agricultural soils, using DLVO predictions and parallel plate flow cell studies as guides (Chapter 2). A uniform terminology was assembled to simplify and expand insect anatomical descriptions (Appendix B), which would enhance later analysis of fluid dynamic simulation results (Chapter 4). The uniform terminology was illustrated using a newly created 3D model of insect anatomy to make the terminology more accessible to multidisciplinary scientists

(Chapter 3). The 3D model was also used to simulate fluid dynamics during insect feeding and estimate the drag forces acting on surface-attached bacteria (Chapter 4). Finally, a custom-made simulation was created using raw computer programming for future analyses of how kinetic and thermodynamic factors interact to affect bacterial surface deposition (Appendix E). The aims of this investigation are supported by the hypotheses and objectives presented in the next section.

1.3 Hypotheses and Objectives

Each of the three following hypotheses were investigated and/or supported in each of the three core chapters of this dissertation (Chapters 2 – 4), respectively:

Hypothesis 1: The presence of aqueous titanium dioxide or copper oxide nanoparticles affects the thermodynamics of deposition and retention of E. coli O157:H7 in model 2D and 3D systems.

As part of a joint project with my colleague, Dr. Holly Mayton, the presence of nanoparticles in agricultural waters was examined for its effects on the transport of pathogenic *E. coli* O157:H7 (hereafter referred to as *E. coli*). Nanoparticles are present in the environment, where they induce microbial stress[17,18]. In Chapter 2, environmentally relevant nanoparticle concentrations impacted *E. coli* transport in the model systems. CuO and TiO_2 nanoparticles were utilized because of their usage in agriculture[19,20]. Dr. Mayton used parallel plate flow cell experiments to study how *E. coli* transport is affected in the presence and absence of the nanoparticles as water flows across spinach leaf surfaces. I used saturated sand column experiments to study how *E. coli* transport is affected in soil

in the presence and absence of nanoparticles. Our analyses were informed by characterizations of fluid dynamics and surface interaction forces in these systems, as well as cross-analyses between the two systems. Results from this research indicate that the presence of TiO_2 and CuO nanoparticles at the tested conditions each affect *E. coli* O157:H7 transport in at least one of the model systems.

The presence of CuO increased bacteria attachment in parallel plate experiments and TiO_2 increased bacteria release in sand column experiments. The increase of *E. coli* attachment in the presence of CuO in parallel plate experiments was not predicted by DLVO theory and may have been a biological response to stress. The increase of *E. coli* release in the presence of TiO_2 during column experiments was partially supported by DLVO predictions, which suggests thermodynamic factors played a role. Colloidal particles were released from the column during the step where a solution containing *E. coli* and TiO_2 was pumped through the column, as well as during the following step where DI H_2O was pumped through the column. Most of the colloidal particles were retained in the column throughout both steps. DLVO predictions indicate that during the former step, there is a secondary energy minimum and a large interaction energy maximum. During the later step, a secondary energy minimum is no longer expected to be present. Based on these predictions, colloidal particles would be either retained at the trailing edges of sand grains or released during the former step. During the later step, any colloidal particles retained in the column would be released. Thus, DLVO theory predicted the observed release during the later step, but overpredicted the release during the former step. The overprediction of release was essentially an underprediction of colloidal particle deposition, which could

have been caused by a variety of factors. Potential factors include charge heterogeneity and hydrophobicity of colloidal particles, which affect thermodynamic surface interactions.

Hypothesis 2: Developing a uniform terminology of insect anatomy will make the terminology more accessible to multidisciplinary scientists.

The complexity of insect anatomy and the evolving nature of scientific research have led to inconsistencies and redundancies in anatomical terminology. In particular, the anatomy surrounding functional foreguts of sharpshooter insects was difficult for multidisciplinary scientists to navigate when studying *X. fastidiosa* transmission via insect vectors. In this context, there was a lack of fine-scale terminology for fully appreciating the effects of fluid dynamics on *X. fastidiosa* transmission. To alleviate these issues, a uniform terminology of functional foregut anatomy was developed in Chapter 3. This uniform terminology enhanced the analysis of *X. fastidiosa* transmission in Chapter 4 and made the analysis more accessible to multidisciplinary scientists.

Hypothesis 3: Fluid dynamic forces in insect functional foreguts and plant xylem are the main drivers of X. fastidiosa spread between plants and within plant xylem.

The spread of *X. fastidiosa* between plants and within plant xylem involves many steps, and multiple potential mechanisms for the bacterium's spread have been investigated. The spread between plants involves *X. fastidiosa* acquisition by insect vectors during feeding on infected plants, as well as inoculation into uninfected plants during vector feeding. Bacteria detachment from host plant xylem vessels is thought to be a step in the acquisition process, and bacteria detachment from vector functional foreguts is

thought to be a step in the inoculation process. Similarly, bacteria are thought to detach from xylem vessel walls as a part of the spreading process within plants.

A simplistic analysis might indicate that *X. fastidiosa* is primarily spread due to fluid drag forces that detach bacteria in these scenarios, but more complex hypotheses have been proposed. One published hypothesis states that enzymes in vector saliva degrade bacteria exopolysaccharides, decreasing bacteria surface adhesion[21]. Another hypothesis states that bacteria cells are temporarily suspended in a column of fluid in vector functional foreguts while the insects fly from infected plants to uninfected plants[22]. Thus, before this dissertation research, it was unclear how much of a role fluid drag forces play in *X. fastidiosa* acquisition, inoculation, and spread within xylem vessels.

In Chapter 4, fluid dynamic predictions were used to calculate drag forces acting on in-situ surface-attached cells and compare them to the forces required to detach cells from glass surfaces in laboratory experiments. Results indicate that fluid drag forces during vector feeding are large enough to drive detachment for acquisition and inoculation. Heat maps of fluid drag forces in functional foreguts mirror heat maps of how frequently bacteria colonize portions of the same space, with high drag forces corresponding with low frequencies of bacteria colonization and vice versa. Thus, fluid dynamic forces are expected to be sufficient for driving *X. fastidiosa* spread between plants. However, it is not as clear whether fluid dynamics drive spread within plants. Predicted drag forces in xylem in the absence of insect feeding are not large enough to detach individually surface attached cells, but they may be large enough to detach bacteria as aggregates from xylem wall

biofilms. The role of fluid drag forces in the spread of *X. fastidiosa* is further discussed in Chapter 4.

1.4 Experimental Approach

1.4.1 Chapter 2

In Chapter 2, saturated sand column experiment results explore effects of nanoparticle presence on *E. coli* O157:H7 transport in agricultural soils. Cultivated *E. coli* was washed and suspended in 10 mM KCl at a pH of 7, which is comparable to the chemistry of groundwater[23]. For the experiments that included nanoparticles, either TiO_2 or CuO was added to 10 mM KCl at the environmentally relevant concentrations of 10 mg/mL each, the solution was sonicated to disperse the particles, and the pH of the solution was adjusted to 7 before adding *E. coli.*

Then, the solution was pumped through a chromatography column filled with quartz sand that was previously sieved, cleaned, hydrated, and flushed with 10 mM KCl. The concentrations of *E. coli* and nanoparticles in the solution exiting the sand column were measured using an in-line UV-VIS detector that repeatedly measured absorbance at three different wavelengths throughout the experiment. The three wavelengths had different ratios of absorbance for *E. coli,* TiO_2, and CuO, allowing for inferences about effluent composition. After the *E. coli* solution was pumped through the column for 7.5 pore volumes at a rate that mimicked trickle flows through soil, a multivalve system was used to flush the column with 7.5 pore volumes of 10 mM KCl without introducing gas bubbles. Finally, DI water was flushed through the system for 5 pore volumes, which

simulated a rain event. Notably, the simulated rain event effectively caused retained colloidal particles to become more negatively charged by decompressing their electrostatic double layers, which decreased the depth of the secondary energy minima that would be predicted by DLVO theory[24]. This means that particles that had been loosely held at the trailing edge of sand grains by secondary energy minima are expected to have been released during this step and detected by the UV-VIS. Indeed, colloidal particles were detected in the fluid exiting the sand column during the simulated rain event in experiments with *E. coli* and TiO_2.

After these steps were completed, the sand column was disassembled for dissection experiments. One-centimeter portions of the water-saturated sand column were isolated and placed in separate beakers of DI water. The sand-water mixtures were mechanically agitated and allowed to settle. The absorbances of the supernatants were measured using a UV-VIS detector to determine the relative concentrations of *E. coli* cells and nanoparticles that were retained in each segment of the sand column. Measured concentrations were normalized by the weight of sand in the beakers after using an oven for drying.

DLVO predictions were used to gain insight into *E. coli* and nanoparticle retention and release in sand column experiments. The effective diameters and zeta potentials of *E. coli* cells, TiO_2 particles, and CuO particles were measured separately and in mixtures that mimicked those in column experiments and parallel plate experiments. The measurements were used to make DLVO sphere-plate predictions for the interaction potential energies between colloids and either sand grains or the surfaces in parallel plate experiments.

Parallel plate experiments were cross-analyzed with the sand column experiments to gain additional insights into *E. coli* transport. The parallel plate experiments had identical aquatic chemistry conditions to those in sand column experiments. Parallel plate flow conditions were comparable to those in sand column experiments, as confirmed by calculated particle Peclet numbers. SEM imaging of *E. coli* and nanoparticle mixtures also contributed to the Results and Discussion in Chapter 2.

1.4.2 Chapter 3

In Chapter 3, a uniform terminology of anatomy related to insect vector functional foreguts is illustrated using a novel 3D model and SEM images from a previous study. The 3D model was created in COMSOL Multiphysics® based on over 30 measurements made from published microscopy images of insect anatomy. The 3D model was exported from COMSOL in segments as STL files. Those STL files were imported to MATLAB® for illustration using built-in tools and tools obtained from MATLAB Central's File Exchange. These methods are further described in Chapter 3 and Appendix C.

1.4.3 Chapter 4

In Chapter 4, the fluid drag forces acting on surface-attached bacteria in insects and plants were calculated to study the spread of *X. fastidiosa*. These drag forces were compared with the drag forces required to detach bacteria from glass in published laboratory experiments, as well as spatial bacteria colonization patterns in insect functional

foreguts. Bacteria colonization patterns were synthesized into readily analyzable figures based on previously published work.

Fluid dynamic simulations were completed in COMSOL Multiphysics® and much of the data analysis was completed in MATLAB®. In particular, calculation of drag forces in insect simulations involved using MATLAB® to find thousands of points close to the simulation walls where fluid properties could be probed. Those properties were then used to calculate the drag forces acting on surface-attached bacteria by using a correlation between drag force, fluid velocity, and fluid shear rate (see Appendix D). The distance of the probed points from the walls of the simulations was decided based on an analysis of the fluid velocities and shear rates that would best correlate with drag forces acting on surface-attached bacteria, including both skin (surface) and pressure drag.

The boundary conditions in fluid dynamic simulations were based on published information about the insect-plant system. Simulations of fluid flow in plant xylem in the absence of insect feeding were based on published data about water potential gradients in grapevine xylem. This innovative simulation method is supported by a recent publication that compared *in vivo* grapevine xylem flowrates with those predicted *in silico* based on pressure gradients in xylem vessels[25].

Simulations of fluid flow in an insect functional foregut and plant xylem during insect feeding were based on estimated flowrates during insect feeding and a quasi-steady state assumption. Flowrates were calculated using estimates of the volume of xylem sap that an insect swallows at one time and how long it takes the insect to suck in that much xylem sap and swallow it. The estimate for the volume of swallowed xylem sap was

calculated based on a measurement of internal space in the 3D model of the insect. The estimates for the durations of sucking in and swallowing are based on published electropenetrography measurements of insect feeding behaviors.

The chosen sap temperature in insect simulations is a Fermi estimate based on heat transfer simulations and an analysis that accounts for sharpshooter feeding behavior. Heat transfer simulations between insects and xylem sap in COMSOL Multiphysics® demonstrated that xylem sap should reach the temperature of the insect by the time it reaches the insect functional foregut. A temperature sensitivity analysis of insect simulations revealed that differences in temperature did not substantially affect results.

Another boundary condition in insect simulations was the slip length at the walls, due to their hydrophobicity and smoothness. Slip length was decided based on a published measurement of the slip length of a surface that is expected to have similar hydrophobicity and smoothness to the insect functional foregut surface. In xylem simulations, the slip length was assumed to be zero.

Mesh refinement studies were completed for both xylem simulations and insect simulations to ensure proper simulation parameters were chosen. The viscosity of xylem sap was assumed to be the same as that of water. Xylem sap was assumed to be an incompressible Newtonian fluid that can be modeled by the Navier-Stokes equations at the size scale of interest. The flow in xylem and insect simulations was confirmed to be laminar based on Reynolds number calculations.

1.5 Organization of the Dissertation

The first and last chapters of this dissertation tie together three manuscripts that have resulted from this research. Chapter 1 serves as an introduction to the themes of the three manuscripts. Chapter 2 is a reformatted version of a paper that was published in *Environmental Science: Nano* (full citation below). Chapter 3 is a reformatted version of a paper that was published in *Scientific Reports* (full citation below). Chapter 4 is a reformatted version of a paper that is in preparation for submission. Chapter 5 summarizes the salient findings from Chapters 2 – 4 and comments on future research directions.

1. Mayton, H. M., White, D., Marcus, I. M., & Walker, S. L. (2019). Influence of nano-CuO and -TiO_2 on deposition and detachment of *Escherichia coli* in two model systems. *Environmental Science: Nano*, 6(11), 3268-3279.
2. White, D., Backus, E. A., Marcus, I. M., Walker, S. L., & Roper, M. C. (2021). Functional foregut anatomy of the blue–green sharpshooter illustrated using a 3D model. *Scientific reports*, 11(1), 1-12.

1.6 References

1 Centers for Disease Control and Prevention. Multistate Outbreak of E. coli O157:H7 Infections Linked to Romaine Lettuce (Final Update). (National Center for Emerging and Zoonotic Infectious Diseases (NCEZID), Division of Foodborne, Waterborne, and Environmental Diseases (DFWED), cdc.gov, 2018).

2 Centers for Disease Control and Prevention. Outbreak of E. coli Infections Linked to Romaine Lettuce. (National Center for Emerging and Zoonotic Infectious Diseases (NCEZID), Division of Foodborne, Waterborne, and Environmental Diseases (DFWED), cdc.gov, 2019).

3 Tumber, K., Alston, J. & Fuller, K. Pierce's disease costs California $104 million per year. *California Agriculture* **68**, 20-29 (2014).

4 Schneider, K. *et al.* Impact of Xylella fastidiosa subspecies pauca in European olives. *Proceedings of the National Academy of Sciences* **117**, 9250-9259 (2020).

5 Mayton, H. M., Marcus, I. M. & Walker, S. L. Escherichia coli O157: H7 and Salmonella Typhimurium adhesion to spinach leaf surfaces: Sensitivity to water chemistry and nutrient availability. *Food microbiology* **78**, 134-142 (2019).

6 Kim, H. N., Bradford, S. A. & Walker, S. L. Escherichia coli O157: H7 transport in saturated porous media: Role of solution chemistry and surface macromolecules. *Environmental science & technology* **43**, 4340-4347 (2009).

7 Rapicavoli, J. N. *et al.* O antigen modulates insect vector acquisition of the bacterial plant pathogen Xylella fastidiosa. *Applied and environmental microbiology* **81**, 8145-8154 (2015).

8 Ubbink, J. & Schär-Zammaretti, P. Colloidal properties and specific interactions of bacterial surfaces. *Current Opinion in Colloid & Interface Science* **12**, 263-270 (2007).

9 Carniello, V., Peterson, B. W., van der Mei, H. C. & Busscher, H. J. Physico-chemistry from initial bacterial adhesion to surface-programmed biofilm growth. *Advances in colloid and interface science* **261**, 1-14 (2018).

10 Elimelech, M., Gregory, J. & Jia, X. *Particle deposition and aggregation: measurement, modelling and simulation*. (Butterworth-Heinemann, 2013).

11 Bin, G., Cao, X., Dong, Y., Luo, Y. & Ma, L. Q. Colloid deposition and release in soils and their association with heavy metals. *Critical Reviews in Environmental Science and Technology* **41**, 336-372 (2011).

12 Verwey, E. J. W. Theory of the stability of lyophobic colloids. *The Journal of Physical Chemistry* **51**, 631-636 (1947).

13 Liu, H. H., Lanphere, J., Walker, S. & Cohen, Y. Effect of hydration repulsion on nanoparticle agglomeration evaluated via a constant number Monte–Carlo simulation. *Nanotechnology* **26**, 045708 (2015).

14 Walker, S. L. *Mechanisms of bacterial adhesion to solid surfaces in aquatic systems*. (Yale University, 2005).

15 Bakker, D. P., Busscher, H. J. & van der Mei, H. C. Bacterial deposition in a parallel plate and a stagnation point flow chamber: microbial adhesion mechanisms depend on the mass transport conditions. *Microbiology* **148**, 597-603 (2002).

16 Walker, S. L., Redman, J. A. & Elimelech, M. Influence of growth phase on bacterial deposition: Interaction mechanisms in packed-bed column and radial stagnation point flow systems. *Environmental Science & Technology* **39**, 6405-6411 (2005).

17 Keller, A. A. & Lazareva, A. Predicted releases of engineered nanomaterials: from global to regional to local. *Environmental Science & Technology Letters* **1**, 65-70 (2014).

18 Mayton, H. M., White, D., Marcus, I. M. & Walker, S. L. Influence of nano-CuO and-TiO 2 on deposition and detachment of Escherichia coli in two model systems. *Environmental Science: Nano* **6**, 3268-3279 (2019).

19 Yang, F. *et al.* The improvement of spinach growth by nano-anatase TiO 2 treatment is related to nitrogen photoreduction. *Biological trace element research* **119**, 77-88 (2007).

20 Ayoub, H. A., Khairy, M., Elsaid, S., Rashwan, F. A. & Abdel-Hafez, H. F. Pesticidal activity of nanostructured metal oxides for generation of alternative pesticide formulations. *Journal of agricultural and food chemistry* **66**, 5491-5498 (2018).

21 Backus, E. A. *et al.* Salivary enzymes are injected into xylem by the glassy-winged sharpshooter, a vector of Xylella fastidiosa. *Journal of insect physiology* **58**, 949-959 (2012).

22 Backus, E. A., Shugart, H. J., Rogers, E. E., Morgan, J. K. & Shatters, R. Direct evidence of egestion and salivation of *Xylella fastidiosa* suggests sharpshooters can be “flying syringes”. *Phytopathology* **105**, 608-620 (2015).

23 Kinsinger, N., Honda, R., Keene, V. & Walker, S. L. Titanium dioxide nanoparticle removal in primary prefiltration stages of water treatment: role of coating, natural

organic matter, source water, and solution chemistry. *Environmental Engineering Science* **32**, 292-300 (2015).

24 Redman, J. A., Walker, S. L. & Elimelech, M. Bacterial Adhesion and Transport in Porous Media: Role of the Secondary Energy Minimum. *Environmental Science & Technology* **38**, 1777-1785, doi:10.1021/es034887l (2004).

25 Bouda, M., Windt, C. W., McElrone, A. J. & Brodersen, C. R. In vivo pressure gradient heterogeneity increases flow contribution of small diameter vessels in grapevine. *Nature communications* **10**, 1-10 (2019).

Chapter 2

Transport of *Escherichia coli* Bacteria in Two Model Systems

Mayton, H. M., White, D., Marcus, I. M., & Walker, S. L. (2019). Influence of nano-CuO and-TiO_2 on deposition and detachment of *Escherichia coli* in two model systems. *Environmental Science: Nano*, 6(11), 3268-3279.

Abstract

Growing evidence suggests that agricultural water quality is closely tied to food safety risks. Therefore, the presence of nanoparticles in environmental waters due to utilization as pesticides and fertilizers may have unintended consequences, as the effects of their interactions with foodborne bacteria are not well understood. This investigation utilizes a 2D parallel-plate flow cell and a 3D saturated sand column to systematically examine changes in bacterial transport trends due to nano-bio interactions under dynamic flow conditions. Two *Escherichia coli* species, O157:H7 and 25922, exposed to nano-CuO (<50 nm) and nano-TiO_2 (<150 nm), were used to mimic agriculturally relevant conditions. In flow cell experiments, the presence of nano-CuO increased deposition and minimized release of pathogenic *E. coli* O157:H7 on a model spinach surface, while nano-TiO_2 had no significant effects ($p > 0.05$). Attachment and detachment – as quantified by mass transfer rate coefficients – of *E. coli* 25922 from the leaf surface were not impacted by the presence of nanoparticles. No breakthrough was observed in the column experiments, with the exception of nano-TiO_2 eluted in the presence of *E. coli* O157:H7. However, column dissection revealed higher proportions of suspended particles retained in the upper portion of the column when either nanoparticle was present. This provides further evidence that nanoparticles affect bacterial deposition and release, potentially promoting biofilm formation and foodborne illness risks.

2.1 Introduction

Within the United States and globally, a significant portion of foodborne illness outbreaks are related to microbial contamination of fruits and vegetables[1, 2]. This is often caused by irrigation and washing processes, where water potentially harbors harmful bacteria, leading to microbial cross contamination[3-5]. *Escherichia coli* (*E. coli*) O157:H7 is a pathogenic bacteria of particular interest due to two 2018 foodborne illness outbreaks associated with romaine lettuce, in which at least 112 people were hospitalized and 5 deaths were reported due to contamination that was found in irrigation water[6]. The fate of pathogens within produce irrigation, washing, and processing steps remains of interest for public health, as several recent studies have raised concerns about the efficacy of common rinsing and disinfection procedures[7-9].

In parallel with modern food safety challenges, nanoparticles are increasingly common in agricultural waters and are being widely considered for application as pesticides and soil amendments in agricultural operations[10-15]. Fungicide formulations containing copper (I) oxide have been employed in the U.S. since the 1950s, and in recent years nanoscale copper oxide (CuO) has gained attention for its potential to serve as a more cost-efficient and environmentally-friendly pesticide[16, 17]. For example, Ayoub et al. (2018) demonstrated that nano-CuO could effectively control the viability of cotton leafworm[18]. Other agricultural applications of nano-CuO have included inhibition of pathogenic wheat isolates and control of fungal infections of tomato plants[19, 20]. Similarly, titanium dioxide (TiO_2) nanoparticles have demonstrated potential as pesticides and as plant growth supplements[21-25]. For example, nano-TiO_2 has been shown to enhance the growth of

spinach leaves, as well as improve seed germination and seedling growth for wheat and parsley[21, 22, 24]. More recently, Mattiello and Marchiol (2017) demonstrated that nano-TiO_2 can positively promote vegetative growth and enhance nutritional value of barley grains when applied throughout the plant growth process[25].

Efficient use of these nanofertilizers and nanopesticides may increase crop yields and provide complementary or replacement technologies for conventional chemical inputs, reducing agricultural runoff and resulting environmental impacts[13,15]. However, further research is needed to improve our understanding of the variety of mechanisms in which nanomaterials suppress disease and enhance plant growth, which can have unintended consequences. For example, many nanoparticles, including CuO and TiO_2, have been shown to induce stress and affect quorum sensing for microbes in environmentally relevant conditions, which can influence the cells' likelihood of adhesion and ability to form biofilms[26-28]. A review of several copper-based nanomaterials described toxic effects on some strains of *E. coli* and other microbes at concentrations as low as 4 ppm in aquatic environments[29]. Interactions between nano-TiO_2 and *E. coli* were studied previously in quartz sand column transport experiments, which found that the presence of *E. coli* reduced deposition of industrial grade nano-TiO_2[30]. However, few studies have utilized and compared applicable nanoparticles in agriculturally relevant scenarios, which include their interactions with non-targeted bacteria[30, 31].

The work presented herein contributes to the understanding of aqueous interactions and transport of a specific foodborne pathogen (*E. coli* O157:H7) and metal oxide nanoparticles, specifically nano-CuO and nano-TiO_2 in agricultural systems. Non-

pathogenic *E. coli* 25922, which is a quality control strain commonly employed by the agricultural industry, is also used for comparison to the pathogen in this study. A 2D parallel-plate flow cell and 3D saturated sand column were used to systematically examine changes in bacteria deposition and detachment trends as a result of nano-bio interactions under dynamic flow conditions on model leaf and mineral surfaces. By studying these idealized systems in tandem, the results provide unique insights into how physiochemical parameters of colloids affect their interactions with more complex real-life environments[30, 32].

2.2 Materials and Methods

2.2.1 Nanoparticle selection and characterization.

Copper oxide (CuO) was selected as a model nanoparticle for this study because of its use in agriculture as an herbicide[18-20]. Nano-CuO was purchased from Sigma Aldrich (St. Louis, MO) and was reported to have a primary particle size of <50 nm. Food grade (FG) TiO_2 (anatase, E171, Arizona State University) was selected as the other model nanoparticle with a primary particle size of 122 ± 48 nm, as measured by electron microscopy in Yang et al. (2014)[33]. Anatase TiO_2 was chosen due to its promising agricultural applications, such as a fungicide and a plant growth enhancer[34, 35]. On account of the photocatalytic activity of nano-TiO_2, all suspensions were kept wrapped in foil to minimize UV light exposure during preparation.

Stock solutions were prepared using dry nanoparticle powder and sonicated for 30 min in 10 mM KCl. Then the pH of the solution was adjusted to 7.0 using KOH and HCl, followed by 30 sec of sonication[36]. For experiments with *E. coli*, concentrated bacteria

stock was then added. With or without bacteria, nanoparticle solutions were gently shaken for 40 min to allow aggregation to occur and stabilize. Both nanoparticles were used at a concentration of 10 mg/mL, corresponding to 10^9 and at least 10^{10} primary particles/mL for TiO_2 and CuO, respectively. The reported ranges of concentrations of nanoparticle formulations for agricultural applications are from 0.005 – 50 mg/mL for TiO_2 and 0.01 – 10 mg/mL for CuO[18-25, 34, 35]. Therefore, a nanoparticle concentration of 10 mg/mL was chosen, within the aforementioned environmentally relevant range, to maximize observable effects while remaining below previously observed toxic concentrations of nano-TiO_2 and nano-CuO[37, 38].

Zeta potential and hydrodynamic diameter were determined for each nanoparticle suspension using a ZetaPALS analyzer and dynamic light scattering (DLS), respectively (Brookhaven Instruments Corp., Holtsville, NY)[39].

2.2.2 Bacteria selection and characterization.

E. coli O157:H7 and 25922 (ATCC 43888 and 25922) were chosen as model bacteria for this study to represent a pathogenic and non-pathogenic strain, respectively. The strains were acquired from the USDA (USDA-ERS-FAESR, Bowling Green, KY). *E. coli* O157:H7 has been recently implicated in several major foodborne illness outbreaks associated with leafy greens[40], while *E. coli* 25922 is a commonly used surrogate for assessing efficacy of food safety processes in the agricultural industry[41]. *E. coli* cells were cultured overnight in Luria-Bertani (LB) broth (Fisher Scientific, Fair Lawn, NJ) at 37 °C. The overnight culture was then diluted 1:100 in fresh LB, incubated at 37 °C for 3.5 hours,

and harvested at the mid-exponential cell growth phase[42]. Bacteria were suspended in 10 mM KCl (with or without nanoparticles) at a concentration of 10^9 cells/mL, and zeta potentials and hydrodynamic diameters were also determined, both separately and in the presence of nanoparticles. For all transport experiments with each of the two strains, scenarios tested were either suspensions of cells only, cells with CuO, or cells with TiO_2.

2.2.3 Parallel-plate experiments.

In a parallel plate flow cell (GlycoTech, Rockville, MA), deposition and release of the model *E. coli* on a spinach leaf surface was directly observed using an inverted microscope (BX-52, Olympus) and digital camera (Demo Retiga EXI Monochrome, QImaging) as previously described[7, 43, 44]. All baby spinach leaves used in this study were pre-washed, bagged spinach from the same brand and purchased from the same local grocery store. As detailed in Mayton et al. (2019), epicuticle films were isolated from the spinach leaf surface through a freeze embedding technique and transferred to a polycarbonate substrate, which were stored at 4 °C for up to one week before use in the parallel-plate flow cell[45].

Cell suspensions were allowed to attach to the leaf surface at a flow rate of 0.1 mL/min using a syringe pump over 30 min. This flow rate creates non-turbulent flow conditions and simulates expected conditions in a gentle produce washing process or rain event[46]. After a 5 min rinse with sterile 10 mM KCl to remove reversibly attached cells, deionized (DI) water was injected into the flow cell for 25 min to observe detachment. Over the course of the 60 min experiment, photos were taken every 30 sec and a code

developed using Matlab (Mathworks, Natwick, MA) was used to quantify the number of cells attached or detached from the surface over time. Enumeration of cells was then used to calculate attachment and detachment mass transfer rate coefficients (k_{att} and k_{det}, respectively) as a function of bacteria flux (J, cells s^{-1} m^{-2}) and concentration of cells in suspension (C_0, cells/mL), where

$$k = \frac{J}{C_0}$$

Detachment is also reported as a percentage of cells removed based on the number of counted cells in the last frame of the attachment phase. Additionally, the duration of detachment (before the slope of cells vs. time reaches zero) varied and is therefore also presented in this study. Experimental scenarios with each combination of bacteria and nanoparticle, as well as each individual bacteria strain, were conducted in triplicate and statistical analysis was performed using a statistical single-factor ANOVA test for confidence intervals of 95% and 99% ($p < 0.05$ and $p < 0.01$, respectively).

2.2.4 Saturated sand column experiments.

In the 3D transport experiments through a quartz packed bed, the movement of *E. coli* and metal oxide nanoparticles in saturated soil conditions was observed using an in-line UV-VIS detector, as previously described[47, 48] and documented in the supplementary information (Appendix A). Briefly, the packed columns were primed with 10 mM KCl, before the aforementioned suspensions were pumped into the column at 2 mL/min for approximately 7.5 pore volumes (PV), followed by approximately 7.5 PV of 10 mM KCl, and 5 PV of DI water. This flow rate was chosen to mimic slow sand grain filtration and

trickle flows through soil[31]. The column effluent flowed through a UV-VIS detector (TURNER SP-890) with an in-line cuvette. Absorbance measurements were taken every 30 sec at a wavelength of 600 nm to monitor the presence of nanoparticles and bacteria, and to generate breakthrough curves (see Appendix A for further information). Scenarios included *E. coli* O157:H7 alone, with CuO, and with TiO_2, and were each conducted in triplicate. One control was conducted with *E. coli* 25922 in the absence of nanoparticles as a control experiment.

Column dissections were performed once for each experimental scenario to elucidate differences in retention that may not be apparent from breakthrough curves[49]. Using a modified method from Lanphere *et al.* (2013) to minimize disruption of bacterial cells, sand was removed from the column in one centimeter increments[49]. The optical density (OD) of the supernatant extracted from each sand segment was measured at 600 nm and normalized based on the weight of the sand in the tube and the proportion to the total absorbance of all five, 1 cm sections.

2.2.5 Scanning electron microscopy.

Scanning electron microscopy (SEM) was utilized to visualize each bacterium and their interactions with nanoparticle suspensions in order to corroborate and provide further insight into the size distribution measured using dynamic light scattering described in Section 2.1. A MIRA3 GMU field emission SEM (TESCAN, Brno, Czech Republic) was used to acquire at least 5 images of suspensions from each experimental condition (cells only or cells plus nanoparticles). For imaging by SEM, 15 μL of each sample (10× diluted

to 1 mM KCl) was dispensed and dried onto polycarbonate coupons, sputter coated with gold/palladium, and analyzed at 15 kV accelerating voltage, using low vacuum mode at a working distance of 4.80 mm.

2.3 Results and Discussion

2.3.1 Critical observations and implications for pathogen fate.

The results gleaned from this study provide insight into deposition and detachment trends of agriculturally relevant bacteria and nanomaterial mixtures by using fundamental 2D and 3D transport models. The 2D model spinach environment (parallel plate flow cell) provided a physically simple, but chemically heterogeneous, environment for direct observation of cell attachment and detachment. Meanwhile, the 3D packed bed provided a physically complex, but chemically simple environment where cell attachment and detachment were indirectly observed. Both systems involved negatively charged collector surfaces, but the hydrodynamics of the two systems have been demonstrated to foster different modes of colloidal deposition[40]. However, the particle Peclet numbers in the column and parallel plate chamber are comparable, and are expected to be within the diffusion-limited regime[39, 47]. Together, the 2D and 3D systems provide corroborating evidence of the role of irreversible attachment in bacterial fate and transport in the simulated agriculturally relevant scenarios.

In the results presented below, the presence of 10 mg/mL of nanoparticle food grade TiO_2 particles resulted in a steady or slightly increased release of pathogenic *E. coli* O157:H7 from leaf and sand surfaces. This suggests that the application of TiO_2 may promote reversible bacterial attachment and presents a safety consideration due to bacteria

release that can cause cross contamination during a food rinsing process or rain event. The presence of nano-CuO lead to an increase in bacterial attachment and decrease in detachment on both leaf and sand surfaces, possibly fostering increased food illness risk by enhancing irreversible attachment, a critical early stages of the biofilm formation process[50, 51].

The effects of these nanoparticles were observed to be more pronounced on the transport of *E. coli* O157:H7 than the common non-pathogenic quality control strain, *E. coli* 25922, as transport of the more neutrally charged pathogen may be more sensitive to changes in the suspension fluid. This may lead to underestimation of changes in microbial risks through the food system as a result of using nanomaterials in agricultural operations. Also of environmental relevance is the observed decrease in deposition of TiO_2 in clean bed filtration in the presence of bacteria. This may be due to increased stability associated with extracellular polymeric substances (EPS) on the nanoparticle surface, and may lead to enhanced transport of TiO_2 in soils. The influence of nano-bio interactions on bacterial transport in agricultural scenarios varied by cell type and nanoparticle type: copper oxide nanoparticles increased irreversible pathogen attachment, while titanium dioxide nanoparticles slightly increased pathogen transport. The results of this work contribute to greater understanding of the associated food safety and environmental risks.

2.3.2 Nanoparticle and bacteria characterization.

2.3.2a Physiochemical characterization.

The electrophoretic mobility and average effective diameter of suspensions comprised of each type of nanoparticles, *E. coli*, and the relevant mixtures are displayed in Table 1. At pH 7, CuO is near its isoelectric point and therefore - under the solution chemistry conditions of this study - the particles are close to neutrally charged (-6.11 ± 3.6 mV)[52]. TiO_2 is far from its isoelectric point and therefore is more negatively charged at the test pH of 7 in these suspensions (-34.5 ± 9.6 mV)[53]. Due to the greater magnitude of charge of TiO_2, these particles are more repulsive and therefore form smaller aggregates relative to their primary particle size (758 ± 111 relative to approximately 120 nm) than CuO (468 ± 28 relative to <50 nm). For the nanoparticles alone, the calculated zeta potential and effective diameter are similar to those of previous work with these metal oxide particles[52-54].

In agreement with previous studies, both bacteria cells are negatively charged in these conditions, with *E. coli* 25922 highly negatively charged (-44.4 ± 2.1), while *E. coli* O157:H7 is close to neutral (-3.4 ± 0.3)[41, 55]. Comparing the hydrodynamic diameters, *E. coli* 25922 cells are 1821 ± 125 nm while *E. coli* O157:H7 cells are smaller at 1410 ± 161 nm. With the addition of 10 mg/mL of each nanoparticle, the relative proportion of bacterial cells to nanoparticles (in numbers) was on the order of 1:1 for nano-TiO_2 and 1:10 for nano-CuO (Table S1). The net charge of the particles in suspension, as measured by zeta potential, was not significantly affected with CuO in suspension ($p > 0.05$), but measurements showed significantly more negatively charged colloids with TiO_2 present (p

< 0.01). The measured effective hydrodynamic diameter of the suspensions was apparently reduced by the presence of nanoparticles, compared to the bacteria alone.

Table 2.1 Characterization of each bacteria, nanoparticle, and combination.

Bacteria	Nanoparticle	Effective diameter (nm)[a]	Zeta potential (mV)[b]
E. coli O157:H7	--	1410 ± 161	-3.4 ± 0.3
E. coli O157:H7	CuO	1221 ± 155	-4.0 ± 0.6
E. coli O157:H7	TiO_2	608 ± 71	-10.0 ± 0.4
E. coli 29522	--	1821 ± 125	-44.4 ± 2.1
E. coli 29522	CuO	1327 ± 38	-44.9 ± 1.2
E. coli 29522	TiO_2	1209 ± 205	-45.1 ± 1.1
--	CuO	468 ± 28	-6.1 ± 3.6
--	TiO_2	758 ± 111	-34.5 ± 9.2

[a] Measured using dynamic light scattering (DLS)
[b] Measured using ZetaPALS via electrophoretic mobility

2.3.2b SEM images.

To corroborate size and surface charge results, SEM images were taken of the bacteria and nanoparticle mixtures (Figure 2.1). Overall, nanoparticles are well-incorporated in bacteria aggregates for both strains of *E. coli*. Nanoparticle aggregation up to approximately 1 μm diameter aggregates is evident in these conditions for both CuO and TiO_2. This result is slightly larger than what is expected based on dynamic light scattering results in Table 1, as well as previous work with these nanoparticles in low ionic strength and pH 7 solutions[29,30]. For *E. coli* O157:H7, images show well-defined cells and nanoparticle aggregates. In contrast, obtaining sharp and clear photos of nanoparticle aggregates in the *E. coli* 25922 mixture was more difficult since 25922 has visibly more EPS than O157:H7, prepared at the same conditions (Figure 2.1). These images provide evidence that EPS can cover some portion of the nanoparticle surface in suspension.

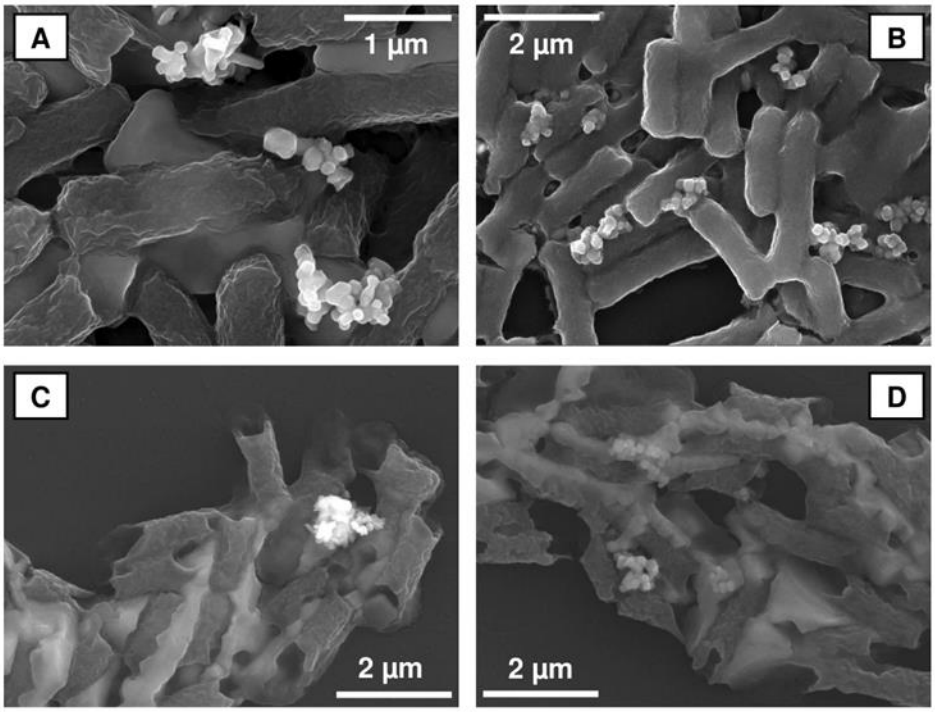

Figure 2.1 SEM images of *E. coli* O157:H7 (A, B) and *E. coli* 25922 (C, D). Images were captured after suspensions with 10 mg/mL of either CuO (A, C) or TiO_2 (B, D) in 10 mM KCl were deposited and dried on polycarbonate coupons using a modified version of the methods previously described by Chowdhury et al. (2012)[30].

Given that the maximum ratio of bacteria cells to nanoparticles was 1:20, it is not surprising to see that most bacteria are not coated in nanoparticles. However, SEM images show interactions in which nanoparticles are often positioned tightly between two or more bacteria. This is notable because physical interactions have been shown to be one of the primary mechanisms by which nanoparticles induce stress in bacteria cells[18, 56, 57]. For example, previous work with antibacterial silver nanoparticles found that electrostatic forces were a primary mechanism of nanoparticle adsorption to bacteria surfaces[58]. Studies with both nano-CuO and -TiO_2 have documented the importance of proximity to the cell

surface to induce the toxic effects of copper ions and reactive oxygen species on gram positive and gram negative bacteria[57].

2.3.2c DLVO predictions.

Colloidal size and surface charge results were used to predict the electrostatic and van der Waals forces between particles and cells, and between heteroaggregates and collector surfaces, using Derjaguin-Landau-Verwey-Overbeek (DLVO) theory[59]. Traditional electrokinetic characterization and application of DLVO theory provides insight into the interactions between cells and nanoparticles, as well as with the plant and mineral surfaces. Non-pathogenic *E. coli* 25922 cells had a greater magnitude of measured zeta potential than the pathogenic strain (O157:H7) (-44.4 ± 2.1 and -3.4 ± 0.3 mV, respectively), which resulted in greater predicted repulsive forces between cells and other negatively charged surfaces. Therefore, it was anticipated that the non-pathogen cells would be more stable in the environment than the pathogen, which was expected to be more adhesive, and therefore less mobile. With addition of nanoparticles in suspension that may associate with the bacteria surface, the overall effective shape of a cell with a nanoparticle adhered to its surface was considered unchanged. Using this assumption, one would not expect to observe significant differences in bacterial transport with the addition of nanoparticles based on DLVO. However, significant impacts are observed in 2D and 3D transport scenarios, suggesting that other mechanisms may be involved. Additionally, the potential formation of irregularly shaped bacteria-nanoparticle aggregates and their interactions with the leaf and grain surfaces presents a challenge to the usefulness of DLVO

in describing this complex system. More details on DLVO calculations are provided in the Appendix A.

2.3.3 Observations and mechanisms of deposition and detachment on spinach leaf surfaces.

Deposition of *E. coli* O157:H7 and *E. coli* 25922 cells was investigated for each strain on its own, and in the presence of each of the two nanoparticles. The average number of cells observed per experiment across all attachment and detachment scenarios was 177 ± 58. Presence of nano-CuO increased *E. coli* O157:H7 adhesion to spinach epicuticle surfaces by nearly 50%, from 14.50 ± 2.39 to 28.11 ± 2.77 × 10^{-8} m/s, as shown in Figure 2.2a. There was no significant difference between *E. coli* O157:H7 adhesion alone or in the presence of TiO_2 (16.57 ± 4.72 × 10^{-8} m/s) ($p > 0.05$). Figure 2.2b summarizes adhesion of *E. col*i 25922 to the epicuticle surface, which was not significantly impacted by the presence of either nanoparticle (15.36 ± 1.43, 12.71 ± 4.29, and 15.55 ± 2.32 × 10^{-8} m/s for *E. coli* alone, with CuO, and with TiO_2, respectively) ($p > 0.05$). This may be attributed to its observed high EPS production and agglomeration that screen the impact of nanoparticles on the cell, which is further discussed in Section 3.5.

Detachment from the epicuticle surface is presented as detachment rate coefficients, in Figure 2.2a and Figure 2.2b. Detachments rates of *E. coli* O157:H7 in every scenario were similar, and less than half of the magnitude of the attachment rate coefficients, ranging from -6.05 ± 2.62 to -7.46 ± 0.89 × 10^{-8} m/s. While no detachment of *E. coli* 25922 was observed over the period of time tested. Additionally, this outcome was not impacted by the presence of either nanoparticle. However, when detachment was normalized by the

total cells observed at the end of the attachment phase, nuances in the trends became apparent (Figure 2.3). Only 5 % of *E. coli* O157:H7 cells in the presence of CuO detached, while 14 % and 18 % of cells were removed when *E. coli* O157:H7 attached alone and in the presence of TiO_2, respectively. The amount of time over which detachment was observed is referred to as "Time to plateau" in Figure 2.3. This refers to the point in which no additional cells are being removed from the epicuticle surface during the 30 min rinse with DI water. This length of time varied between scenarios, with *E. coli* O157:H7 alone detaching over 13.5 min, O157:H7 with TiO_2 detaching over 14.5 min, and O157:H7 with CuO detaching over just 7.0 min. These results imply that CuO not only increases deposition rates of *E. coli* O157:H7, but also increases the amount of irreversibly attached cells.

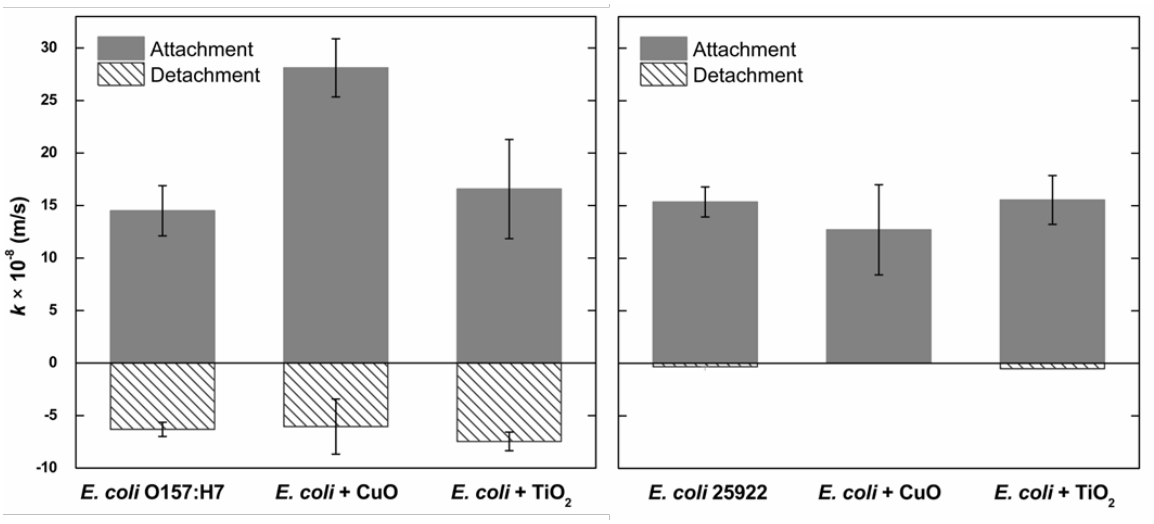

Figure 2.2 Bacterial adhesion and detachment on spinach surface. Attachment (top) and detachment (bottom) mass transfer rate coefficients for *E. coli* O157:H7 (left) and *E. coli* 25922 (right) in 10 mM KCl on spinach leaf surfaces. Error bars represent on standard deviation from 3 replicates.

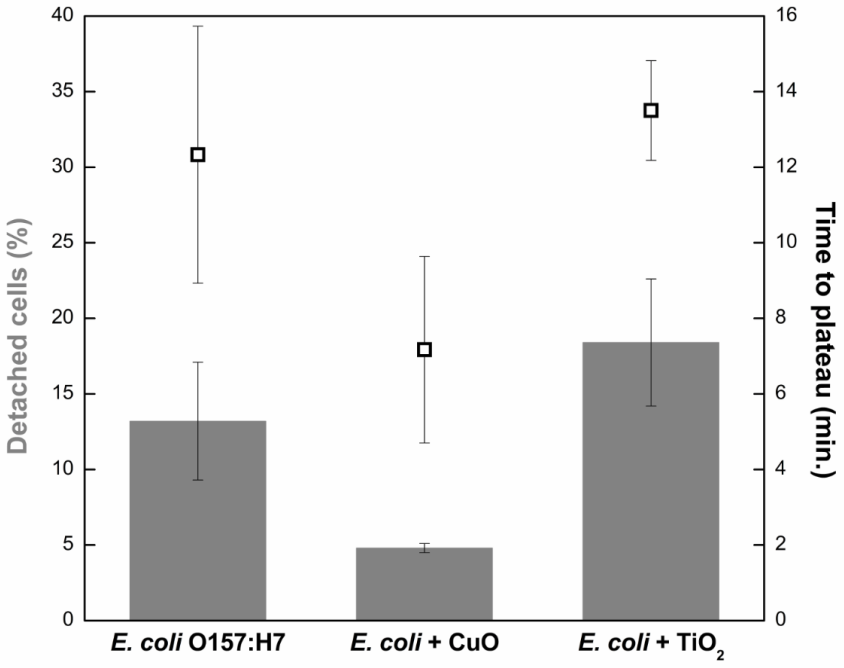

Figure 2.3 Pathogen detachment from spinach leaf surface. Percentage of *E. coli* O157:H7 cells detached over 30 min with DI water rinse (gray bars, left axis) and time over which the rate of detachment is greater than zero (□, right axis). Error bars represent the standard deviation calculated from 3 replicates.

2.3.4 Observations and mechanisms of deposition and release in the packed bed column.

For column experiments, breakthrough curves were generated to represent elution of the *E. coli* strains and nanoparticles from the packed bed. Removal of *E. coli* O157:H7 alone and in the presence of nano-CuO was essentially complete (100.0 ± 0.4% and 100.0 ± 0.6%, respectively). These scenarios showed minimal release in the phase of the experiment in which the column is flushed (rinsed) with DI H_2O (1.2 ± 0.4% and 1.5 ± 0.6%) (Figure 2.4). Conversely, significantly higher release of 7.5 ± 2.6% was observed with *E. coli* O157:H7 in the presence of TiO_2 ($p < 0.01$).

In addition to the observed reduction in removal of *E. coli* O157:H7 in the column with TiO_2, breakthrough of TiO_2 particles was also observed in this scenario (Figure 2.5). This result is in contrast with control experiments with each nanoparticle alone. In the control experiments, complete removal was observed for both nanoparticles in the simple electrolyte background (data not shown), despite significant repulsive forces between TiO_2 and quartz predicated by particle-plate DLVO modeling. It is hypothesized that interactions between *E. coli* O157:H7 cells and TiO_2 in suspension results in increased stability for TiO_2 particles in suspension due to extracellular polymers that have been demonstrated to increase steric hindrance[30, 60]. Specifically, Chowdhury et al. (2012) utilized TiO_2 in a similar column apparatus under similar conditions (pH 7, 10 mg/mL TiO_2, 10 mM KCl) and also found that particle transport increased in the presence of *E. coli* due to increased electrosteric repulsion[30].

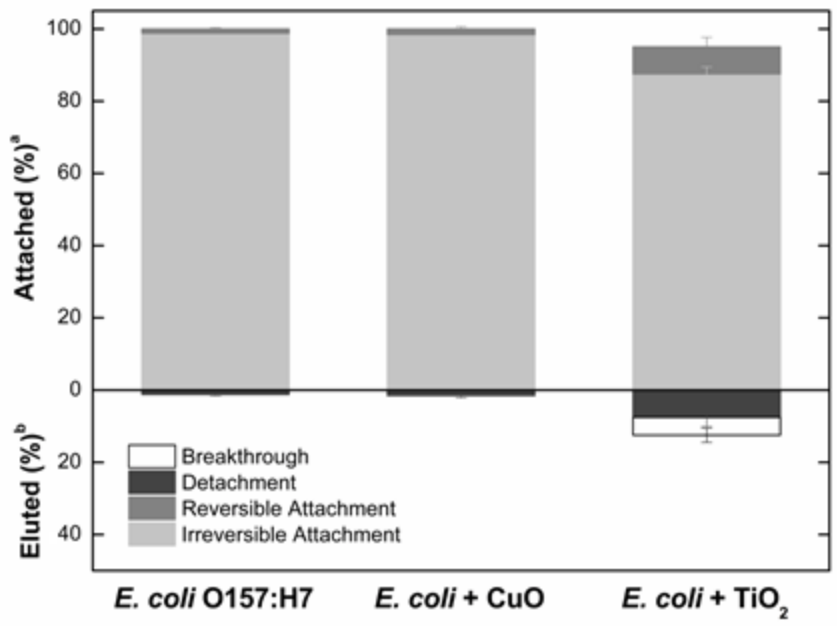

Figure 2.4 *E. coli* O157:H7 removal and release in the saturated sand column. Breakthrough and release values were calculated by integrating under the breakthrough and DI rinse curves, respectively. Deposition values were calculated using the breakthrough and release values and mass balances. Error bars represent one standard deviation from three replicates. [a] Calculated based on mass balances. [b] Calculated based on UV-VIS absorbance.

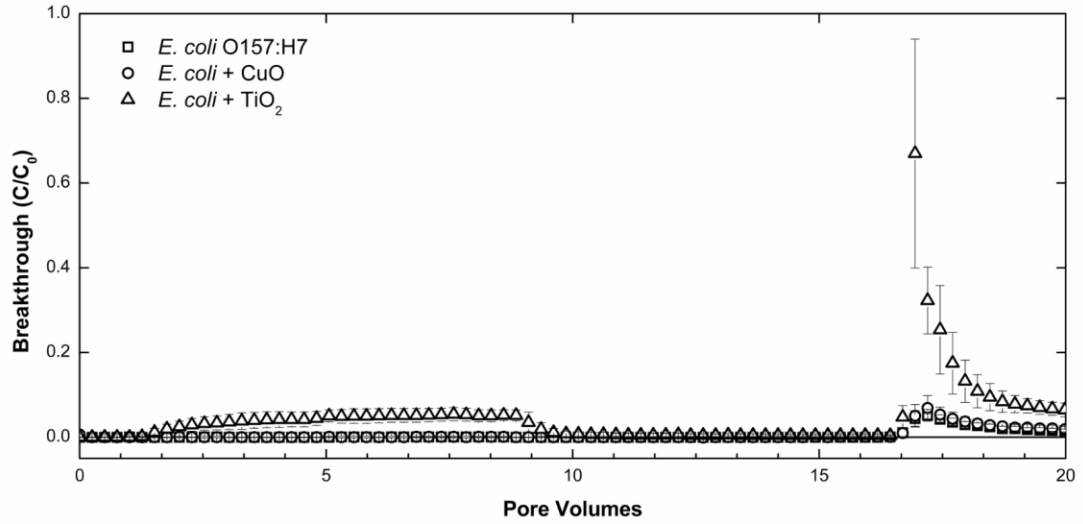

Figure 2.5 Breakthrough curves for saturated sand column transport experiments with *E. coli* O157:H7. Columns were injected with 10^9 cells/mL in 10 mM KCl electrolyte at pH 7, with or without 10 mg/mL of nanoparticle. Error bars represent one standard deviation from three replicates. Experimental conditions: Darcy velocity = 1 cm/min, Reynolds = 0.1, bed length = 5 cm, bed diameter = 1.5 cm, porosity = 0.45, average grain diameter = 275µm.

Column retention profiles were created to further elucidate retention trends between these three scenarios (Figure 2.6). The trends for the suspension of *E. coli* with nanoparticles is based on absorbance values at 600 nm, and is therefore expected to be an indicator of bacterial retention, since cells have higher absorbance than either CuO or TiO_2 particles at the concentrations used in this study (see Appendix A for additional details). The retention curves for the pathogen with nanoparticles show exponential decay in the concentration of retained particles with increasing depth of the column, which is expected based on clean bed filtration theory that is governed by first-order attachment[55]. The shape of the retention curve in for the *E. coli* O157:H7 and TiO_2 suspension suggests that the first 2 cm of the column became saturated with retained particles. In the absence of

nanoparticles, nearly linear decay of pathogen retention is observed. This trend is characteristic of zeroth order deposition kinetics, which are not expected for deposition driven by DLVO forces and implies that bacterial retention may be dominated by other mechanisms, such as limited cell surface sorption sites.

The presence of nanoparticles appears to increase the retention of suspension species in the porous media. This is suggested by a greater fraction of retention in the upper portion of the column (CC/CN = 0.3, 0.4, and 0.5 at the inlet for *E. coli* O157:H7 alone, with TiO_2, and with CuO, respectively). Specifically, the presence of CuO had a pronounced effect on the retention profile of the *E. coli* O157:H7-nanoparticle suspension. This mirrors the observed increase in bacterial attachment rates to spinach leaf surfaces in the presence of CuO.

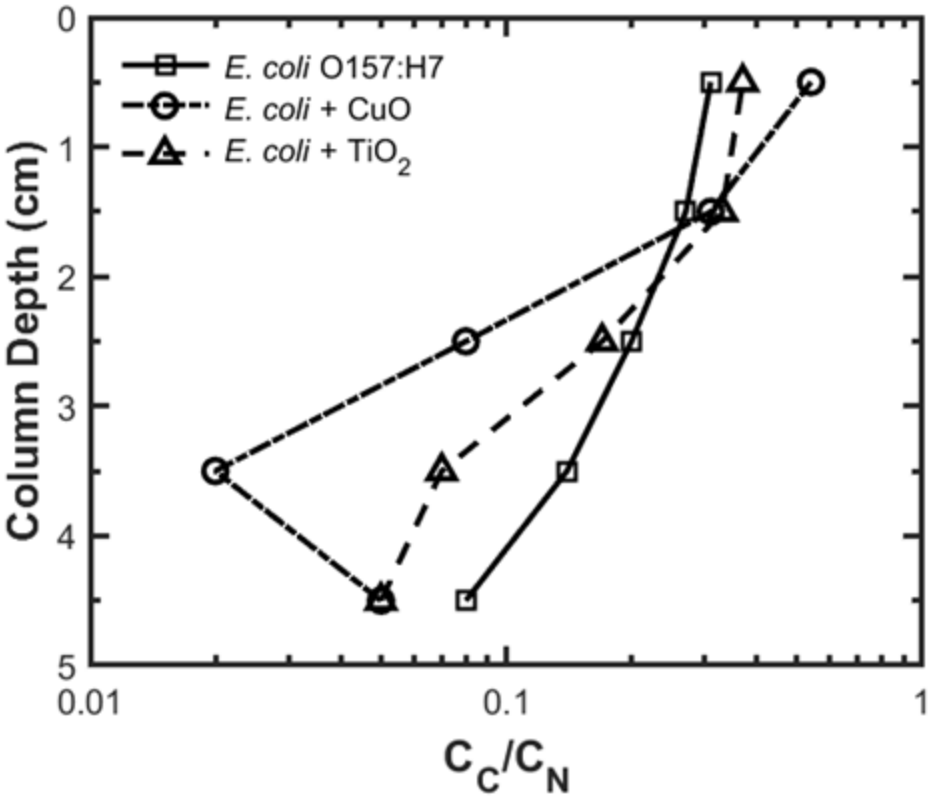

Figure 2.6 Column retention profiles. Column retention profiles of *E. coli* O157:H7 alone and with each nanoparticle. C_C and C_N are defined as concentration of recovered particles and the sum of concentrations of recovered particles for a given suspension, respectively. A depth of 0 cm corresponds to the entrance of the column.

2.3.5 Nanoparticle impacts on bacteria fate.

By utilizing and comparing 2D and 3D transport models, the impacts of sub-lethal concentrations of nano-CuO and -TiO_2 on bacterial fate in simplified agricultural environments have been demonstrated. Notably, minimal changes were observed when using *E. coli* 25922 in the presence of nanoparticles. This may be attributed to the highly negative surface charge and greater EPS production of *E. coli* 25922 cells, which is supported by previous studies that have demonstrated enhanced resistance to nanomaterial

toxicity by cells that overproduce EPS[61, 62]. Non-pathogenic *E. coli* 25922 has been utilized in many studies on microbial transport, fate, and influence in agricultural environments as a model microorganism, under the assumption that the results can apply to pathogen fate and thus inform decision-making about associated food safety risks[41, 63-70]. However, these results make it clear that employing only this non-pathogen surrogate species would drastically underestimate the influence of nanoparticles on bacteria in these environments. In contrast to *E. coli* 25922, the observed changes in fate and transport trends of pathogenic *E. coli* O157:H7 cells were significant and varied by nanoparticle type.

Specifically, nano-CuO caused an increase in irreversible *E. coli* O57:H7 attachment to both leaf and sand surfaces, potentially fostering increased food illness risk by enhancing the early stages of the biofilm formation process. Previous studies have indicated that small amounts of copper-based nanomaterials, on the order of the concentrations employed in this study, can induce stress responses in bacterial cells[18, 71, 72]. The small primary particle size and near neutral zeta potential may allow nano-CuO particles to interact strongly with the cell surface, or even enter the cell18. Additionally, CuO can dissolve into copper ions in suspension, which are highly toxic to bacteria[18, 73]. At these experimental conditions, nano-CuO was demonstrably stable in solution, as expected based on previous work that found nano-CuO aggregation rates to be correlated with increasing ionic strength[52]. Adeleye et al. (2014) found that the presence of bacterial EPS in suspension further increased stability, which lead to increased dissolution of CuO nanoparticles over long term studies in 10 mM NaCl at pH 7 and caused more oxidative stress[74]. One common stress response in bacteria is the overproduction of EPS and

increased adhesion to surfaces, in order to begin the process of forming a protective biofilm[75]. Once formed, mature biofilms have been shown to protect *E. coli* O157:H7 cells from several common disinfectants used in the food industry[76, 77].

In many ways, nano-TiO_2 is similar to nano-CuO. It has also been demonstrated to have increasingly stability in the presence of organic matter[30] and to induce stress in several types of bacteria[78-80]. However, nano-TiO_2 had no significant impact on the deposition and detachment of *E. coli* on the spinach surface, and even reduced irreversible deposition on quartz collectors. This is similar to work by Jomini et al. (2015), which observed an increase in planktonic, versus adhered, environmental bacteria over long term exposure to nano-TiO_2[81]. One important difference between the two studied nanoparticles is that of size: smaller particles tend to be more toxic than larger counterparts[82, 83], potentially making the antibacterial influence of primary TiO_2 nanoparticles (~122 nm) less than that of CuO nanoparticles (<50 nm). Further, as evidenced by the SEM images in Figure 2.1, the studied nanoparticles are likely to interact with bacteria cells in the form of larger homoaggregates at the tested experimental conditions. Nano-CuO is expected to aggregate to approximately 500 nm, while nano-TiO_2 aggregates should be significantly larger at approximately 800 nm (Table 1).

At these solution conditions, TiO_2 is also considerably more negatively charged than CuO (-34.5 versus -6.11 mV, respectively). While this does not make it significantly less likely to interact with the *E. coli* O157:H7 cells based on DLVO predications, it does result in substantial energy barriers between nano-TiO_2 and the spinach and quartz surfaces, which may reduce opportunities for particles to interact with adherent bacteria.

Further, the antibacterial activity of nano-TiO_2 is largely attributed to reactive oxygen species produced through photocatalysis. Leung et al. (2016) previously observed that light penetration was significantly inhibited by bacteria in suspension at 10^8 cells per mL[84], resulting in reduced toxicity of TiO_2 particles that may explain the lesser impact on bacterial transport, in comparison with nano-CuO.

Low concentrations of nanoparticles have been consistently predicted and monitored in environmental waters around the world, on the order of 0.01 – 1 μg/L[85]. However, studies that demonstrate the efficacy of these nanoparticles as pesticides and fertilizers have applied concentrations between 1 and 1000 mg/L[18-25]. Therefore, our utilization of 10 mg/L nano-CuO and –TiO_2 likely overestimates the influence of nanoparticles in raw environmental waters, but may underestimate the effects of direct aqueous applications to leaves and soil in agriculture. Agricultural environments are also likely to have significant amounts of natural organic matter (NOM), unlike the simple systems that were used here. Metal oxide nanoparticles, including nano-CuO and -TiO_2, have been shown to be increasingly stable in the presence of NOM[30, 54]. This reduction in nanoparticle aggregation could result in greater toxicity and thus more pronounced effects on bacterial cells than observed in this study.

Overall, the results of this work elucidate some impacts of the complex physiochemical interactions between nanoparticles and bacteria by using model systems to simulate aqueous agricultural environments and identify potential food safety risks. While nanoparticles had no significant effects on *E. coli* 25922, nano-CuO increased irreversible attachment rates of *E. coli* O157:H7 cells and nano-TiO_2 slightly reduced irreversible

deposition on quartz surfaces. However, these results are based on just two nanoparticle species, as well as one non-pathogen surrogate and one foodborne pathogen serovar. It is essential that further research is conducted with additional types of nanoparticles, bacteria, and environmental conditions to inform decision-making that aims to manage microbial risks throughout the food production and transport system that may result from increased use of nanoparticles in agricultural operations.

2.4 References

1. Interagency Food Safety Analytics Collaboration. Foodborne illness source attribution estimates for Salmonella, *Escherichia coli* O157 (*E. coli* O157), Listeria monocytogenes (Lm), and Campylobacter using outbreak surveillance data. 2016.

2. World Health Organization (WHO). WHO estimates of the global burden of foodborne diseases: foodborne disease burden epidemiology reference group 2007-2015. 2015.

3. A.N. Olaimat and R.A. Holley, Factors influencing the microbial safety of fresh produce: A review, Food Microbiology, 2012, 32, 1-19.

4. S.A. Bradford and R.W. Harvey, Future research needs involving pathogens in groundwater, Hydrogeology Journal, 2017, 25, 931-938.

5. M. Jongman and L. Korsten, Irrigation water quality and microbial safety of leafy greens in different vegetable production systems: A review, Food Reviews International, 2018, 34, 308-328.

6. Centers for Disease Control and Prevention (CDC). Multistate Outbreak of *E. coli* O157:H7 Infections Linked to Romaine Lettuce (Final Update), 2018 Outbreaks, https://www.cdc.gov/ecoli/2018/o157h7-04-18/index.html, (accessed 2018-11-15)

7. N.M. Kinsinger, H.M. Mayton, M.R. Luth, and S.L. Walker, Efficacy of post-harvest rinsing and bleach disinfection of *E. coli* O157: H7 on spinach leaf surfaces, Food Microbiology, 2017, 62, 212-220.

8. Y. Luo, X. Nou, Y. Yang, I. Alegre, E. Turner, H. Feng, M. Abadias, and W. Conway, Determination of free chlorine concentrations needed to prevent *Escherichia coli* O157: H7 cross-contamination during fresh-cut produce wash, Journal of Food Protection, 2011, 74, 352-358.

9. C. Goodburn and C.A. Wallace, The microbiological efficacy of decontamination methodologies for fresh produce: a review, Food Control, 2013, 32, 418-427.

10. A.A. Keller and A. Lazareva, Predicted releases of engineered nanomaterials: From global to regional to local, Environmental Science & Technology Letters, 2014, 1, 65-70.

11. M. Kah and T. Hofmann, Nanopesticide research: Current trends and future priorities, Environment International, 2014, 63, 224-235.

12. B. Asadishad, S. Chahal, A. Akbari, V. Cianciarelli, M. Azodi, S. Ghoshal, and N. Tufenkji, Amendment of agricultural soil with metal nanoparticles: Effects on soil

enzyme activity and microbial community composition, Environmental Science & Technology, 2018, 52, 1908-1918.

13. C.O. Dimkpa and P.S. Bindraban, Nanofertilizers: new products for the industry?, Journal of Agricultural and Food Chemistry, 2017.

14. I. Iavicoli, V. Leso, D.H. Beezhold, and A.A. Shvedova, Nanotechnology in agriculture: Opportunities, toxicological implications, and occupational risks. Toxicology and applied pharmacology, 2018, 329, 96–111. doi:10.1016/j.taap.2017.05.025

15. I.O. Adisa, V.L. Reddy Pullagurala, J.R. Peralta-Videa, C.O. Dimkpa, W.H. Elmer, J.L. Gardea-Torresdey, and J.C. White, Recent advances in nano-enabled fertilizers and pesticides: a critical review of mechanisms of action. Environmental Science: Nano, 2019, Advance Article. doi: 10.1039/C9EN00265K

16. University of Hertfordshire, Copper (1) Oxide, Pesticide Properties Database (PPDB). https://sitem.herts.ac.uk/aeru/ppdb/en/Reports/176.htm (accessed 6-25-2019).

17. L. Kiaune and N. Singhasemanon, Pesticidal copper (I) oxide: environmental fate and aquatic toxicity, Reviews of Environmental Contamination and Toxicology, 2011, 213, 1-26.

18. H.A. Ayoub, M. Khairy, S. Elsaid, F.A. Rashwan, and H.F. Abdel-Hafez, Pesticidal Activity of Nanostructured Metal Oxides for Generation of Alternative Pesticide Formulations, Journal of Agricultural and Food Chemistry, 2018, 66, 22, 5491-5498. doi: 10.1021/acs.jafc.8b01600

19. Z. Zabrieski, E. Morrell, J. Hortin, C. Dimkpa, J. McLean, D. Britt, A. Anderson, Pesticidal activity of metal oxide nanoparticles on plant pathogenic isolates of Pythium, Ecotoxicology, 2015, 24, 1305-1314. doi:10.1007/s10646-015-1505-x

20. K. Giannousi, I. Avramidis, and C. Dendrinou-Samara, Synthesis, characterization and evaluation of copper based nanoparticles as agrochemicals against Phytophthora infestans, RSC Advances, 2013, 3, 21743-21752.

21. F. Yang, C. Liu, F. Gao, M. Su, X. Wu, L. Zheng, F. Hong, and P. Yang, The improvement of spinach growth by nano-anatase TiO_2 treatment is related to nitrogen photoreduction. Biological Trace Element Research, 2007, 119, 77-88.

22. H. Feizi, P.R. Moghaddam, N. Shahtahmassebi, and A. Fotovat, Impact of bulk and nanosized titanium dioxide (TiO_2) on wheat seed germination and seedling growth. Biological Trace Element Research, 2012, 146, 101-106.23. A. Servin, W. Elmer, A. Mukherjee, R. De la Torre-Roche, H. Hamdi, J.C. White, P. Bindraban, and C.

Dimkpa, A review of the use of engineered nanomaterials to suppress plant disease and enhance crop yield, Journal of Nanoparticle Research, 2015, 17, 92.

24. M. Qi, Y. Liu, and T. Li, Nano-TiO_2 Improve the Photosynthesis of Tomato Leaves under Mild Heat Stress, Biological Trace Element Research, 2013, 156, 323-328. doi:10.1007/s12011-013-9833-2

25. A. Mattiello and L. Marchiol, Application of Nanotechnology in Agriculture: Assessment of TiO_2 Nanoparticle Effects on Barley, Application of Titanium Dioxide, IntechOpen, doi: 10.5772/intechopen.68710

26. G. Applerot, J. Lellouche, A. Lipovsky, Y. Nitzan, R. Lubart, A. Gedanken, and E. Banin, Understanding the antibacterial mechanism of CuO nanoparticles: Revealing the route of induced oxidative stress, Small, 2012, 8, 3326-3337.

27. K. Naik and M. Kowshik, Anti-quorum sensing activity of AgCl-TiO_2 nanoparticles with potential use as active food packaging material, Journal of Applied Microbiology, 2014, 117, 972-983.

28. B.R. Singh, B.N. Singh, A. Singh, W. Khan, A.H. Naqvi, and H.B. Singh. Mycofabricated biosilver nanoparticles interrupt Pseudomonas aeruginosa quorum sensing systems, Scientific Reports, 2015, 5, 13719.

29. A.A. Keller, A.S. Adeleye, J.R. Conway, K.L. Garner, L. Zhao, G.N. Cherr, J. Hong, J.L. Gardea-Torresdey, H.A. Godwin, S. Hanna, Z. Ji, C. Kaweeteerawat, S. Lin, H.S. Lenihan, R.J. Miller, A.E. Nel, J.R. Peralta-Videa, S.L. Walker, A.A. Taylor, C. Torres-Duarte, J.I. Zink, and N. Zuverza-Mena, Comparative environmental fate and toxicity of copper nanomaterials, NanoImpact, 2017, 7, 28-40.

30. I. Chowdhury, D.M. Cwiertny, and S.L. Walker, Combined factors influencing the aggregation and deposition of nano-TiO_2 in the presence of humic acid and bacteria. Environmental Science & Technology, 2012, 46, 6968-6976.

31. T.J. Battin, F.V. Kammer, A. Weilhartner, S. Ottofuelling, and T. Hofmann, Nanostructured TiO_2: Transport behavior and effects on aquatic microbial communities under environmental conditions, Environmental Science & Technology, 2009, 43, 8098-8104.

32. J.A. Redman, S.L. Walker, and M. Elimelech, Bacterial adhesion and transport in porous media: Role of the secondary energy minimum, Environmental Science & Technology, 2004, 38, 1777-1785.

33. Y. Yang, K. Doudrick, X. Bi, K. Hristovski, P. Herckes, P. Westerhoff, and R. Kaegi, Characterization of food-grade titanium dioxide: the presence of nanosized particles, Environmental Science & Technology, 2014, 48, 6391-6400.

34. F. Hong, J. Zhou, C. Liu, F. Yang, C. Wu, L. Zheng, and P. Yang, Effect of nano-TiO_2 on photochemical reaction of chloroplasts of spinach, Biological Trace Element Research, 2005, 105, 269-279.

35. M.L. Paret, G.E. Vallad, D.R. Averett, J.B. Jones, and S.M. Olson, Photocatalysis: Effect of light-activated nanoscale formulations of TiO_2 on Xanthomonas perforans and control of bacterial spot of tomato, Phytopathology, 2013, 103, 228-236.

36. I. Chowdhury, Y. Hong, and S.L. Walker, Container to characterization: Impacts of metal oxide handling, preparation, and solution chemistry on particle stability, Colloids and Surfaces A: Physicochemical and Engineering Aspects, 2010, 368, 91-95.

37. L.K. Adams, D.Y. Lyon, P.J.J. Alvarez. Comparative eco-toxicity of nanoscale TiO_2, SiO2, and ZnO water suspensions, Water Research, 2006, 40, 3527-3532.

38. O. Bondarenko, K. Juganson, A. Ivask, K. Kasemets, M. Mortimer, and A. Kahru, Toxicity of Ag, CuO and ZnO nanoparticles to selected environmentally relevant test organisms and mammalian cells in vitro: a critical review, Archives of Toxicology, 2013, 87, 1181-1200.

39. T, Waller, I.M. Marcus, and S.L. Walker, Influence of septic system wastewater treatment on titanium dioxide nanoparticle subsurface transport mechanisms. Analytical and Bioanalytical Chemistry, 2018, p. 1-8.

40. Centers for Disease Control and Prevention (CDC), Reports of Selected *E. coli* Outbreak Investigations: September 20, 2018, https://www.cdc.gov/ecoli/outbreaks.html, 2018-11-15

41. K.L. Cook, E.C. Givan, H.M. Mayton, R.R. Parekh, R. Taylor, and S.L. Walker, Using the agricultural environment to select better surrogates for foodborne pathogens associated with fresh produce, International Journal of Food Microbiology, 2017, 262, 80-88.

42. B. Haznedaroglu, H. Kim, S. Bradford, and S.L. Walker, Relative transport behavior of *Escherichia coli* O157: H7 and Salmonella enterica serovar pullorum in packed bed column systems: Influence of solution chemistry and cell concentration, Environmental Science & Technology, 2009, 43, 1838-1844.

43. J.W. McClaine and R.M. Ford, Characterizing the adhesion of motile and nonmotile *Escherichia coli* to a glass surface using a parallel-plate flow chamber. Biotechnology and Bioengineering, 2002, 78, 179-189.

44. G. Chen, D.E. Beving, R.S. Bedi, Y.S. Yan, and S.L. Walker, Initial bacterial deposition on bare and zeolite-coated aluminum alloy and stainless steel, Langmuir, 2009, 25, 1620-1626.

45. H.M. Mayton, I.M. Marcus, and S.L. Walker, *Escherichia coli* O157:H7 and Salmonella Typhimurium adhesion to spinach leaf surfaces: Sensitivity to water chemistry and nutrient availability, Food Microbiology, 2019, 78, 134-142.

46. K. Huang, Y. Tian, D. Salvi, M. Karwe, and N. Nitin, Influence of exposure time, shear stress, and surfactants on detachment of *Escherichia coli* O157:H7 from fresh lettuce leaf surfaces during washing process, Food Bioprocess Technology, 2017, 11, 621-633.

47. H.N. Kim, S.L. Walker, and S.A. Bradford, Macromolecule mediated transport and retention of *Escherichia coli* O157: H7 in saturated porous media, Water Research, 2010, 44, 1082-1093.

48. Y. Hong, R.J. Honda, N.V. Myung, and S.L. Walker, Transport of iron-based nanoparticles: role of magnetic properties, Environmental Science & Technology, 2009, 43, 8834-8839.

49. J.D. Lanphere, C.J. Luth, and S.L. Walker, Effects of solution chemistry on the transport of graphene oxide in saturated porous media, Environmental Science & Technology, 2013, 47, 4255-4261.

50. J. Palmer, S. Flint, and J. Brooks, Bacterial cell attachment, the beginning of a biofilm, J Ind Microbiol Biotechnol, 2007, 34, 577-588.

51. P.M. Stanley, Factors affecting the irreversible attachment of Pseudomonas aeruginosa to stainless steel, Canadian Journal of Microbiology, 1983, 29, 1493-1499.

52. J.R. Conway, A.S. Adeleye, J.L. Gardea-Torresdey, and A.A. Keller, Aggregation, dissolution, and transformation of copper nanoparticles in natural waters. Environmental Science & Technology, 2015, 49, 2749-2756.

53. C. Chen, I.M. Marcus, T. Waller, and S.L. Walker, Comparison of filtration mechanisms of food and industrial grade TiO_2 nanoparticles, Analytical and Bioanalytical Chemistry, 2018, 1-8.

54. A.A. Keller, H. Wang, D. Zhou, H.S. Lenihan, G. Cherr, B.J. Cardinale, R. Miller, and Z. Ji, Stability and aggregation of metal oxide nanoparticles in natural aqueous matrices, Environmental Science & Technology, 2010, 44, 1962-1967.

55. S.A. Bradford, J. Simunek, and S.L. Walker, Transport and straining of *E. coli* O157: H7 in saturated porous media, Water Resources Research, 2006, 42.

56. A. Thill, O. Zeyons, O. Spalla, F. Chauvat, J. Rose, M. Auffan, and A.M. Flank, Cytotoxicity of CeO2 nanoparticles for *Escherichia coli*: Physico-chemical insight of the cytotoxicity mechanism, Environmental Science & Technology, 2006, 40, 6151-6156.

57. M.J. Hajipour, K.M. Fromm, A.A. Ashkarran, D.J. de Aberasturi, I.R. de Larramendi, T. Rojo, V. Serpooshan, W.J. Parak, and M. Mahmoudi, Antibacterial properties of nanoparticles, Trends in Biotechnology, 2012, 30, 499-511.

58. S.S. Khan, A. Mukherjee, and N. Chandrasekaran, Studies on interaction of colloidal silver nanoparticles (SNPs) with five different bacterial species, Colloids and Surfaces B: Biointerfaces, 2011, 87,129-138.

59. B. Derjaguin and L. Landau, Theory of the stability of strongly charged lyophobic sols and of the adhesion of strongly charged particles in solutions of electrolytes, Progress in Surface Science, 1993, 43, 30-59.

60. D. Lin, S.D. Story, S.L. Walker, Q. Huang, W. Liang, and P. Cai, Role of pH and ionic strength in the aggregation of TiO_2 nanoparticles in the presence of extracellular polymeric substances from Bacillus subtilis, Environmental Pollution, 2017, 228, 35-42.

61. Y. Liu, J. Li, X. Qiu, and C. Burda, Bactericidal activity of nitrogen-doped metal oxide nanocatalysts and the influence of bacterial extracellular polymeric substances (EPS), Journal of Photochemistry and Photobiology A: Chemistry, 2007, 190, 94-100.

62. N. Joshi, B.T. Ngwenya, and C.E. French, Enhanced resistance to nanoparticle toxicity is conferred by overproduction of extracellular polymeric substances, Journal of Hazardous Materials, 2012, 241, 363-370.

63. G. Feng, Y. Cheng, S. Wang, D.A. Borca-Tasciuc, R.W. Worobo, and C.I. Moraru, Bacterial attachment and biofilm formation on surfaces are reduced by small-diameter nanoscale pores: how small is small enough?, npj Biofilms and Microbiomes, 2015, 1, 15022.

64. L. Gao, J. Hu, X. Zhang, L. Wei, S. Li, Z. Miao, and T. Chai, Application of swine manure on agricultural fields contributes to extended-spectrum β-lactamase-producing *Escherichia coli* spread in Tai'an, China, Frontiers in Microbiology, 2015, 6, 313.

65. R.S. Suresh Kumar, P.J. Shiny, C.H. Anjali, J.Jerobin, K.M. Goshen, S. Magdassi, A. Mukherjee, and N. Chandrasekaran, Distinctive effects of nano-sized permethrin in the environment, Environmental Science and Pollution Research, 2013, 20, 2593-2602.

66. N. Talebian, M.R. Nilforoushan, and E.B. Zargar, Enhanced antibacterial performance of hybrid semiconductor nanomaterials: ZnO/SnO2 nanocomposite thin films, Applied Surface Science, 2011, 258, 547-555.

67. H. Olmez and S.D. Temur, Effects of different sanitizing treatments on biofilms and attachment of *Escherichia coli* and Listeria monocytogenes on green leaf lettuce, LWT - Food Science and Technology, 2010, 43, 964-970.

68. W.K. Jung, H.C. Koo, K.W. Kim, S. Shin, S.H. Kim, and Y.H. Park, Antibacterial Activity and Mechanism of Action of the Silver Ion in Staphylococcus aureus and *Escherichia coli*, Applied and Environmental Microbiology, 2008, 74, 2171-2178.

69. P. Roslev, L.A. Bjergbaek, and M. Hesselsoe, Effect of oxygen on survival of faecal pollution indicators in drinking water, Journal of Applied Microbiology, 2004, 96, 938-945.

70. N. Aligiannis, E. Kalpoutzakis, S. Mitaku, and I.B. Chinou, Composition and Antimicrobial Activity of the Essential Oils of Two Origanum Species, Journal of Agricultural and Food Chemistry, 2001, 49, 4168-4170.

71. L.M. Gaetke and C.K. Chow, Copper toxicity, oxidative stress, and antioxidant nutrients, Toxicology, 2003, 189, 147-163.

72. O. Bondarenko, A. Ivask, A. Käkinen, and A. Kahru, Sub-toxic effects of CuO nanoparticles on bacteria: Kinetics, role of Cu ions and possible mechanisms of action, Environmental Pollution, 2012, 169, 81-89.

73. Y.W. Baek and Y.J. An, Microbial toxicity of metal oxide nanoparticles (CuO, NiO, ZnO, and Sb2O3) to *Escherichia coli*, Bacillus subtilis, and Streptococcus aureus, Science of the Total Environment, 2011, 409, 1603-1608.

74. A.S. Adeleye, J.R. Conway, T. Perez, P. Rutten, and A.A. Keller, Influence of extracellular polymeric substances on the long-term fate, dissolution, and speciation of copper-based nanoparticles, Environmental Science & Technology, 2014, 48, 12561-12568.

75. P. Landini, Cross-talk mechanisms in biofilm formation and responses to environmental and physiological stress in *Escherichia coli*, Research in Microbiology, 2009, 160, 259-266.

76. B.A. Niemira and P.H. Cooke, *Escherichia coli* O157: H7 biofilm formation on romaine lettuce and spinach leaf surfaces reduces efficacy of irradiation and sodium hypochlorite washes, Journal of Food Science, 2010, 75, 270-277.

77. E.B. Somers, J.L. Schoeni, and A.C. Wong, Effect of trisodium phosphate on biofilm and planktonic cells of Campylobacter jejuni, *Escherichia coli* O157:H7, Listeria monocytogenes and Salmonella typhimurium, International Journal of Food Microbiology, 1994, 22, 269-276.

78. A. Kumar, A.K. Pandey, S.S. Singh, R. Shanker, and A. Dhawan, Engineered ZnO and TiO_2 nanoparticles induce oxidative stress and DNA damage leading to reduced viability of *Escherichia coli*, Free Radical Biology and Medicine, 2011, 51, 1872-1881.

79. G. Zavilgelsky, V.Y. Kotova, and I. Manukhov, Titanium dioxide (TiO_2) nanoparticles induce bacterial stress response detectable by specific lux biosensors, Nanotechnologies in Russia, 2011, 6, 401-406.

80. N. von Moos and V.I. Slaveykova, Oxidative stress induced by inorganic nanoparticles in bacteria and aquatic microalgae–state of the art and knowledge gaps, Nanotoxicology, 2014, 8, 605-630.

81. S. Jomini, H. Clivot, P. Bauda, and C. Pagnout, Impact of manufactured TiO_2 nanoparticles on planktonic and sessile bacterial communities, Environmental Pollution, 2015, 202, 196-204.

82. A. Ivask, I. Kurvet, K. Kasemets, I. Blinova, V. Aruoja, S. Suppi, H. Vija, A. Käkinen, T. Titma, and M. Heinlaan, Size-dependent toxicity of silver nanoparticles to bacteria, yeast, algae, crustaceans and mammalian cells in vitro, PloS One, 2014, 9, e102108.

83. S. Nair, A. Sasidharan, V.D. Rani, D. Menon, S. Nair, K. Manzoor, and S. Raina, Role of size scale of ZnO nanoparticles and microparticles on toxicity toward bacteria and osteoblast cancer cells, Journal of Materials Science: Materials in Medicine, 2009, 20, 235.

84. Y.H. Leung, X. Xu, A.P.Y. Ma, F. Liu, A.M.C. Ng, Z. Shen, L.A. Gethings, M.Y. Guo, A.B. Djurišić, P.K.H. Lee, H.K. Lee, W.K. Chan, and F.C.C. Leung, Toxicity of ZnO and TiO_2 to *Escherichia coli* cells, Scientific Reports, 2016, 6, DOI: 10.1038/srep35243

85. F. Gottschalk, T.Y. Sun, B. Nowack, Environmental concentrations of engineered nanomaterials: Review of modeling and analytical studies, Environmental Pollution, 2013, 181, 287-300.

Chapter 3

Creating a 3D Model of the Blue-Green Sharpshooter Functional Foregut

White, D., Backus, E. A., Marcus, I. M., Walker, S. L., & Roper, M. C. (2021). Functional foregut anatomy of the blue–green sharpshooter illustrated using a 3D model. *Scientific reports*, 11(1), 1-12.

Abstract

Sharpshooter leafhoppers (Hemiptera: Cicadellidae: Cicadellinae) are important vectors of the plant pathogenic bacterium *Xylella fastidiosa* Wells et al. (Xanthomonadales: Xanthomonadaceae). This pathogen causes economically significant diseases in olive, citrus, and grapes on multiple continents. Bacterial acquisition and inoculation mechanisms are linked to *X. fastidiosa* biofilm formation and fluid dynamics in the functional foregut of sharpshooters, which together result in egestion (expulsion) of fluids likely carrying bacteria. One key *X. fastidiosa* vector is the blue-green sharpshooter, *Graphocephala atropunctata* (Signoret, 1854). Herein, a 3D model of the blue-green sharpshooter functional foregut is derived from a meta-analysis of published microscopy images. The model is used to illustrate preexisting and newly defined anatomical terminology that is relevant for investigating fluid dynamics in the functional foregut of sharpshooters. The vivid 3D illustrations herein are suitable resources for multidisciplinary researchers who may be unfamiliar with insect anatomy. The 3D model can also be used in future fluid dynamic simulations to better understand acquisition, retention, and inoculation of *X. fastidiosa.* Improved understanding of these processes could lead to new targets for preventing diseases caused by *X. fastidiosa*.

3.1 Introduction

Sharpshooter leafhoppers (Hemiptera: Cicadellidae: Cicadellinae) feed on plant tissues using their piercing-sucking mouthparts, termed stylets [1]. They transmit (acquire, retain, and inoculate) the xylem-limited bacterial pathogen *Xylella fastidiosa* Wells et al. (Xanthomonadales: Xanthomonadaceae) during feeding [2]. This invasive, pathogenic bacterium causes $100's of millions in agricultural losses annually worldwide from plant diseases on multiple continents, including olive quick decline syndrome in South America and Europe, citrus variegated chlorosis in South America, and Pierce's disease of grape in North America [3]. The state of California alone spends $104 million a year to control *X. fastidiosa* [4]. Of the 2,313 catalogued sharpshooter species worldwide, 35 are reported vectors of *X. fastidiosa* [5]. A native California vector, the blue-green sharpshooter, *Graphocephala atropunctata* (Signoret, 1854), has been used in several studies on the mechanism of *X. fastidiosa* transmission [2,6-8]. Thus, this vector species is used as a model for the present study.

When sharpshooters ingest (take up through the stylets and swallow) xylem sap from an infected grapevine using their stylets, *X. fastidiosa* bacteria are acquired as fluid passes through and resides in the functional foregut, eventually to attach and form a biofilm. *Xylella fastidiosa* is later inoculated via egestion when the vector feeds on healthy grapevine xylem [9,10]. Both the acquisition and inoculation mechanisms involve fluid dynamics in the functional foregut (the narrow precibarium leading to the wider cibarium or food pump) during feeding behaviors [2,11,12]. Better understanding of these mechanisms will aid in interpretation of electropenetrography (EPG) data that is being used to select

and breed crop varieties that can resist inoculation of the bacterium by its vectors (Backus, *unpublished data*).

Previous studies have modeled fluid flow in the sharpshooter functional foregut. Early attempts at modeling relied on average daily excretion rate as a proxy for ingestion, for both blue-green sharpshooters and glassy-winged sharpshooters [6,13]. Velocities in the precibaria of these sharpshooters were estimated by dividing time-averaged feeding/excretion rates by representative cross-sectional areas of the precibaria. Rapicavoli et al. provided a more precise spatial resolution in the functional foregut by creating a simple two-dimensional model of the precibarium and cibarium of the blue-green sharpshooter [14]. Ranieri et al. created three-dimensional (3D) models of the stylet food canal and precibarium of both spittlebugs and sharpshooters [12]. They modeled the precibarium with finer spatial fidelity than any previously published model by using sequential concentric cylindrical segments of variable diameter. This increased spatial resolution was coupled with increased temporal resolution by using EPG data for estimates of ingestion flowrates. However, their model assumed a continuous distribution of bacterial biofilm.

Herein we propose a 3D model of the blue-green sharpshooter functional foregut that further enhances capabilities for modeling fluid flow through the critical bottleneck for flow, the precibarium. The model is based on a meta-analysis of previously published microscopy images of sharpshooters, incorporating over 30 dimensions of the functional foregut collected from the literature. Our model incorporates complex geometries that provide greater morphological fidelity to the actual functional foregut, especially the

precibarium, than previous models. The morphological fidelity of the present model allows for modeling the flowrates close to the precibarial walls in places where the walls curve and bend in ways that are not easily modeled using a cylinder/cone-based 3D model. This will permit assessment of how flow affects surface-attached bacteria at these locations, which will be more relevant for understanding *X. fastidiosa* acquisition, retention, and inoculation.

The anatomical complexity of the sharpshooter functional foregut requires intricate understanding and logical terminology to communicate results effectively [6,7,15-18]. Various terms for the anatomy of the functional foregut, sometimes conflicting, were introduced in previous papers. Therefore, we also seek herein to clarify terms for the anatomical parts and their corresponding regions in the model.

In all hemipterans, the stylet fascicle is the set of mouth parts that are inserted into the plant during feeding. The food canal, formed by grooves in the maxillary stylets, conveys fluid from the plant into the head of the insect, wherein the complete foregut takes over fluid transport. The functional foregut is the segment of the complete foregut that conveys fluid from the proximal opening of the stylet food canal through the precibarium into the cibarium (the sucking pump); the precibarium is also the functional mouth. Fluid then is swallowed through the true mouth (the opening from the cibarium into the pharynx) into the true foregut, consisting of the pharynx then esophagus. Thus, in sharpshooters and other auchenorrhynchan hemipterans, the functional foregut comprises the precibarium and cibarium, while the true foregut comprises the pharynx and esophagus [19,20]. In sharpshooters and other auchenorrhynchan hemipterans, the functional foregut is shaped

like a wineglass (i.e., acetabular), whereas in sternorrynchans and heteropterans, it is tubular in shape[19].

The cibarium functions to both take up fluid from the stylet tips and to swallow fluid past the true mouth into the true foregut (the pharynx and esophagus) [19]. Swallowing of fluid is also termed ingestion [20]. The walls of both the precibarium and cibarium are formed by the apposition of hypopharynx (or hypopharyngeal plate), epipharynx (or epipharyngeal plate), and, in the case of the cibarium, the membranous cibarial diaphragm (the lid of the pump). These walls can be visualized upon dissection of sharpshooter heads, as illustrated previously [7,17,18,21]. Some authors have used the term cibarium chamber for the lumen (cavity) enclosed by these walls [7]. The cibarial walls are composed of the cibarial diaphragm and cibarium bowl [10] . The cibarial diaphragm contains the apodemal groove and pockets of the apodemal groove [15,16].

The precibarium has complex morphology in a small space. There are four anatomical/functional areas that were originally named in sharpshooters based on SEM of the structures in the lumen (that is, they are lumenal structures) [17]. Progressing distally from the opening of the cibarium to the precibarium, the anatomical structures of the precibarium are the: 1) trough, 2) basin (which houses, in order, the H- [hypopharyngeal] sensilla on that side of the basin, then on the epipharyngeal side, the P [proximal]-sensilla, precibarial valve/flap, and its precibarial pit/ring, 3) D (distal)-sensilla field, and 4) hypopharyngeal extension that inserts into the stylet food canal (HEF) [7,11,17]. The blue-green sharpshooter precibarium contains twenty precibarial chemosensilla, split into six groups that each serve as separate, bilaterally symmetrical gustatory organs. Organ status

is based on the arrangement of their neuron cell bodies and the axons/nerve bundles that arise at the precibarium and terminate in the frontal ganglion. The proximal organs each consist of three P-sensilla: one set on the left side of the basin, the other set on the right [18]. The ten D-sensilla are in the D-sensilla field distal to the valve/flap on the epipharyngeal side; again, they comprise two, bilaterally symmetrical organs of five sensilla each. The two H-sensilla are each a separate gustatory organ because their neuron cell bodies and axons are in a separate plate in the head, the hypopharynx [11,18].

Because of the incomplete list of precise descriptive terms for areas of the functional foregut on a fine resolution scale, researchers investigating *X. fastidiosa* biofilm spatial patterns are often left with ambiguous terms to describe biofilm locations, such as "proximal region of precibarium canal," "medial region of the proximal precibarium on the epipharynx," "area on the epipharynx with sutures," and "opening into the cibarium" [11,22]. In particular, the epipharyngeal basin lacks precise descriptive terms. Its portions have been described as the "groove of the basin," "top of the precibarial valve," "top of the valve near the precibarial pit," and "distal extremity of the precibarial valve" [11,22]. Furthermore, anatomical segments are often not clearly delimited in sharpshooter literature. Therefore, we developed new terms that consider biologically relevant delineations of the precibarial and cibarial structures to describe our 3D model of the functional foregut in *G. atropunctata*, particularly in the context of *X. fastidiosa* colonization.

Accordingly, the objectives of this paper are two-fold. First, we introduce and describe a new, 3D anatomical model correlated with microscopy images. Second, the model is used to synthesize anatomical terminology for the complex parts of the functional

foregut, with several proposed anatomical terms. Our larger goal is to better serve future multidisciplinary studies of *X. fastidiosa* acquisition, retention, and inoculation by sharpshooters.

3.2 Results

3.2.1 Illustration of the 3D model

The 3D model mimics the curvature of the blue-green sharpshooter functional foregut with a precision absent in previous models. It incorporates complex morphologies and over 30 dimensions measured from published microscope images. The published microscopy images are of blue-green sharpshooters from different geographical regions and likely different sexes. Segments of the 3D model are illustrated in Figure 3.1, together with the dimensions that are described in Table C.1.1 in Appendix C. The dimensions are indexed based on the subfigure in which they appear. For example, A7 is the seventh dimensional measurement that is illustrated in Figure 3.1a. The 3D model segment color coding is explained in Figure 3.2 and Figure 3.3.

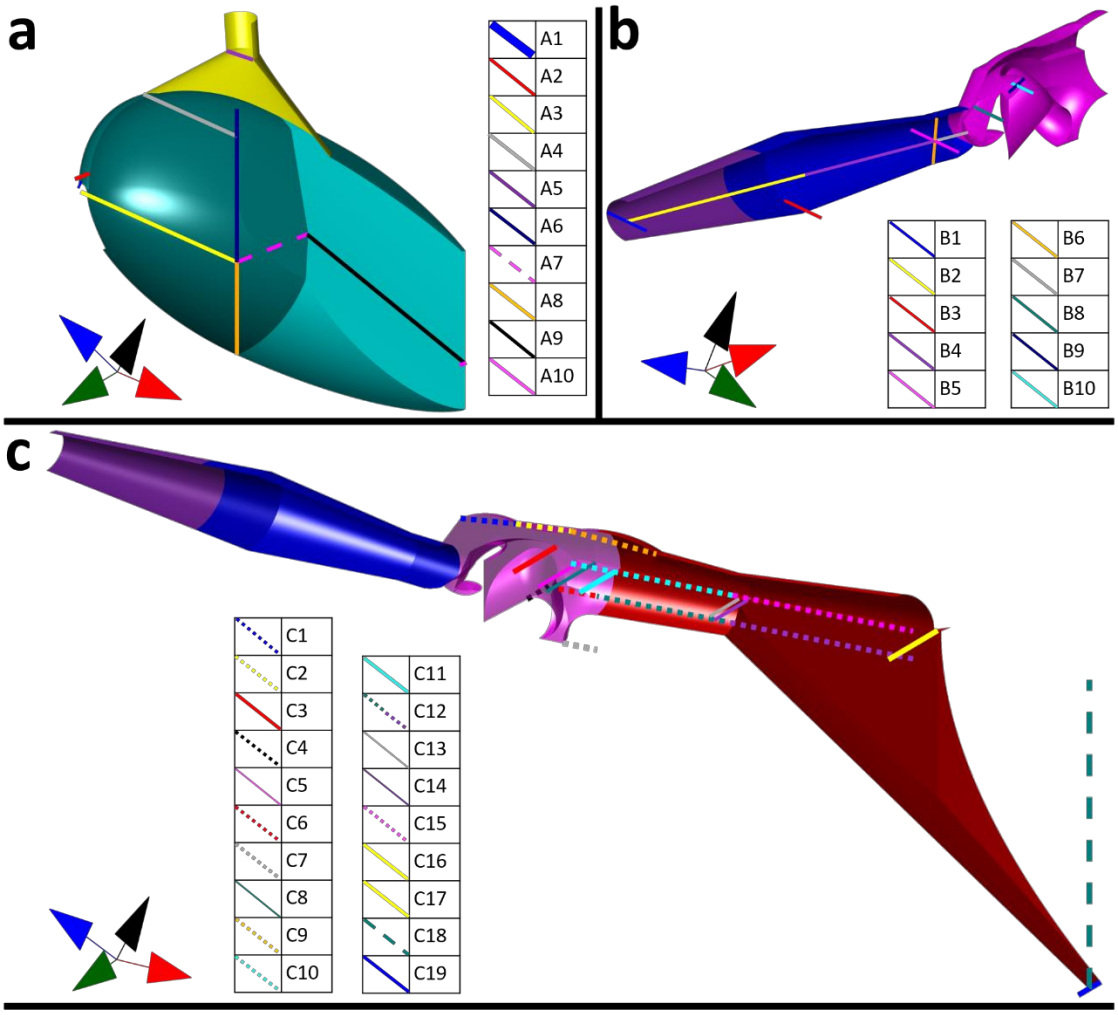
a
A1
A2
A3
A4
A5
A6
A7
A8
A9
A10
b
B1
B2
B3
B4
B5
B6
B7
B8
B9
B10
c
C1
C2
C3
C4
C5
C6
C7
C8
C9
C10
C11
C12
C13
C14
C15
C16
C17
C18
C19

Figure 3.1 Dimensions of the 3D model for the functional foregut of the blue-green sharpshooter, as detailed in Appendix C (Table C.1.1). All views shown are internal (concave). A) Left half of the true mouth (yellow) and cibarium (teal). B) Left half of the HEF (purple), distal enclosure (blue), and basin (magenta). C) Left half of the precibarium. The basin is partially translucent to make dimension C4 visible. The coordinate axes indicate anterior → posterior, distal → proximal (for the trough), ventral → dorsal, and left → right. The dimensions are indexed based on the subfigure in which they appear. For example, A7 is the seventh dimensional measurement that is illustrated in Figure 3.1a. The 3D model segment color coding is explained in Figure 3.2 and Figure 3.3. HEF: hypopharyngeal extension that inserts into the stylet food canal.

The entire 3D model is illustrated in Figure 3.2a. This view of the model has a different viewpoint than the concave microscope images from which it was derived (Appendix C, Table C.1.1). The walls of the model represent walls of the precibarium, cibarium, and true mouth as they would be in undissected sharpshooters, where the hypopharynx and epipharynx are apposed and the cibarial diaphragm is attached to the cibarium bowl. Also, the 3D model is viewed from an imagined exterior of the functional foregut (convex), rather than the interior (concave). The approximate location of the 3D modeled anatomy in a blue-green sharpshooter is shown in Figure 3.2a as if the viewer could see through the insect head. The cibarial diaphragm of the 3D model is fully extended as if the cibarial dilator muscles were fully contracted, pulling the cibarial diaphragm into the head to allow for complete filling of the cibarium. Figure 3.2a is used to define directional coordinate axes that are used in the rest of the 3D model figures. These coordinate axes are species-dependent, due to different orientations of the functional foregut in different sharpshooter species. For example, the 3D model of the functional foregut in Figure 3.2a would need to be rotated around 30 degrees clockwise relative to the

coordinate axes for these terms to be appropriately applied to the cibarium of the glassy-winged sharpshooter, *Homalodisca vitripennis* (Germar, 1821).

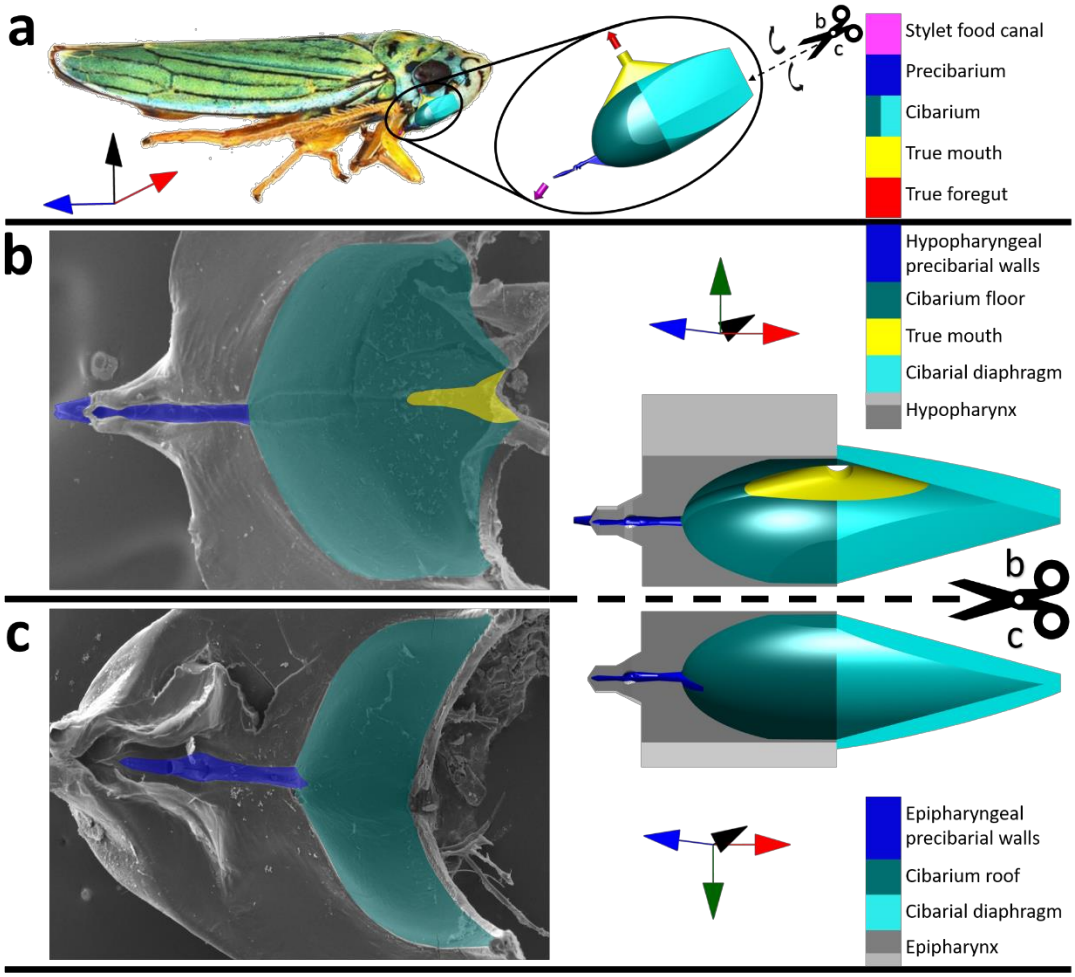

Figure 3.2 Functional foregut (precibarium and cibarium) of the blue-green sharpshooter, with segments of the 3D model labeled with broad terminology. A) Approximate location/orientation of the functional foregut inside the insect. The 3D model shows an external view of the walls of the precibarium, cibarium, and true mouth, as if the rest of the epipharynx, hypopharynx, and cibarial diaphragm did not exist (convex). The image of the insect is used with the permission of the photographer Emilie Bess (EC Bess, USDA APHIS PPQ). B) Hypopharynx electron microscope image (left) and 3D model segment (right, concave, internal) for comparison. The electron microscope image was adapted from a previous publication (Reprinted with permission; copyright © American Society for Microbiology, [*Appl. Environ. Microbiol.* 81, no. 23 (2015): 8145-8154 10.1128/AEM.02383-15]). C) Epipharynx electron microscope image (left) and 3D model segment (right, concave, internal) for comparison. The coordinate axes indicate anterior → posterior, distal → proximal (for the trough), ventral → dorsal, and left → right. The relationship between the functional foregut and coordinate axes is different for different sharpshooter species. The scissors and dotted lines indicate where the 3D model in subfigure a would be split to obtain the 3D model segments in subfigures b and c. The associated black curved arrows in subfigure a indicate that the two halves of the split 3D model segment would need to be hinged outward to obtain the views in subfigures b and c. The gray 3D parts of subfigures b and c are semi-abstract representations of the epipharynx and hypopharynx that serve for comparison with their corresponding electron microscope images.

If the 3D model were split open and its two halves hinged outward, its relation to microscopy images would be more intuitive, as shown in Figure 3.2b and Figure 3.2c. In these subfigures, semi-abstract 3D representations of the epipharynx and hypopharynx (gray in the figures) are illustrated together with the 3D model halves on the right side for comparison with their corresponding SEM images on the left side. Segments of the model halves are shown as concave depressions in the epipharynx and hypopharynx. The adjacent SEMs show the natural, concave view of the functional foregut structure. They are color coded to correspond with color coding in the 3D model halves.

Figure 3.2 is useful for understanding how the epipharynx, hypopharynx, and cibarial diaphragm form the walls of the 3D model. Figure 3.3 is similar to Figure 3.2,

except it focuses on the precibarium. In Figure 3.3a, the precibarial segment of the 3D model in Figure 3.2a is shown up close from an external view as a convex tube-like structure. In the following subfigures, the 3D precibarium exterior is split into its two halves and hinged outward. The concave halves of the precibarium are illustrated as depressions in the semi-abstract representations of the epipharynx and hypopharynx. The four main segments of the precibarium are color coded in both the 3D model and the corresponding SEMS.

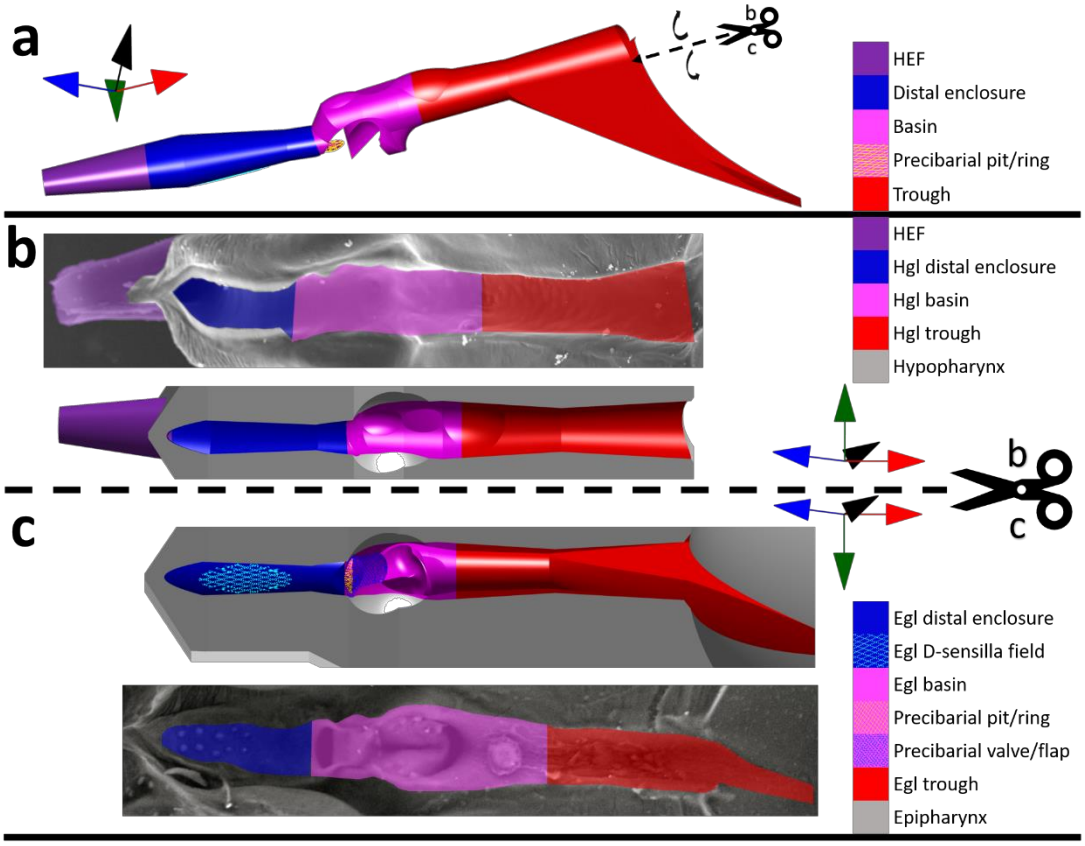

Figure 3.3 Close-up segments of the precibarium of the blue-green sharpshooter, labeled with broad terminology. A) Precibarium 3D model segment. It shows an external view of the walls of the precibarium, as if the rest of the epipharynx and hypopharynx didn't exist (convex). B) Hypopharyngeal precibarial walls (colored, concave) in electron microscope image of a segment of the hypopharynx (top, internal) and equivalent view of the 3D model segment (bottom, concave) for comparison. C) Epipharyngeal precibarial walls 3D model segment (top, mostly concave) and an equivalent electron microscope image (bottom, mostly concave) for comparison. The coordinate axes indicate anterior → posterior, distal → proximal (for the trough), ventral → dorsal, and left → right. The scissors and dotted lines indicate where the 3D model segment in subfigure a would be split to obtain the 3D model segments in subfigures b and c. The associated black curved arrows indicate that the two halves of the split 3D model segment would need to be hinged outward to obtain the views in subfigures b and c. The gray 3D parts of subfigures b and c are semi-abstract representations of the epipharynx and hypopharynx, which serve for comparison with their corresponding electron microscope images. Hgl: hypopharyngeal; egl: epipharyngeal; HEF: hypopharyngeal extension that inserts into the stylet food canal.

The terminology illustrated in Figure 3.2 and Figure 3.3 explains our 3D model and is also helpful for gaining a broad sense of sharpshooter functional foregut anatomy. Figure 3.2 illustrates how the cibarium roof in blue-green sharpshooters is more ventral than the cibarium floor, which is counter-intuitive for non-entomologists because of the opisthognathous (posteriorly directed) orientation of mouthparts in leafhoppers. Figure 3.3 illustrates how the precibarium is broadly made of four segments, one of which is previously un-named. We propose the name "distal enclosure" for the previously un-named region of the precibarial walls that includes the D-sensilla field (Figure 3.3a – c). This is because the term "D-sensilla field" is an abbreviation for "distal precibarial chemosensilla field" and having a shorter name for this segment will make it easier to describe.

3.2.2 Morphological Accuracy of the 3D Model

The model is designed for a balance between precision of fluid dynamic modeling and time costs associated with creating and using a complex 3D model. The model incorporates morphological features that are important for fluid dynamics studies, while ignoring morphologies that are less important for such studies. The primary example of this is the shape of the cibarium model, particularly the ratio of the cibarium floor radius to the cibarium roof radius (Figure 3.1, Dimensions A6 and A8). This ratio is 1.7 in our model, based on a previously published microscope image that shows a blue-green sharpshooter cibarium bowl from a viewpoint similar to that in Figure 3.4a [6]. However, micro-CT measurements in a recently published study show a ratio that is closer to 2.2. [12]. See Figure C.2.1 in Appendix C. The discrepancy between these ratios appears to be due to biological variability, possibly based on the geographically different populations from

which blue-green sharpshooters were obtained. Thus, future studies with larger insect sample sizes than those available for the meta-analysis would be helpful in determining the extent to which cibarium fluid dynamics are affected by cibarium shape variability. In contrast, blue-green sharpshooter precibarium length appears to have smaller variability, with a reported standard deviation of only 6.9% [12].

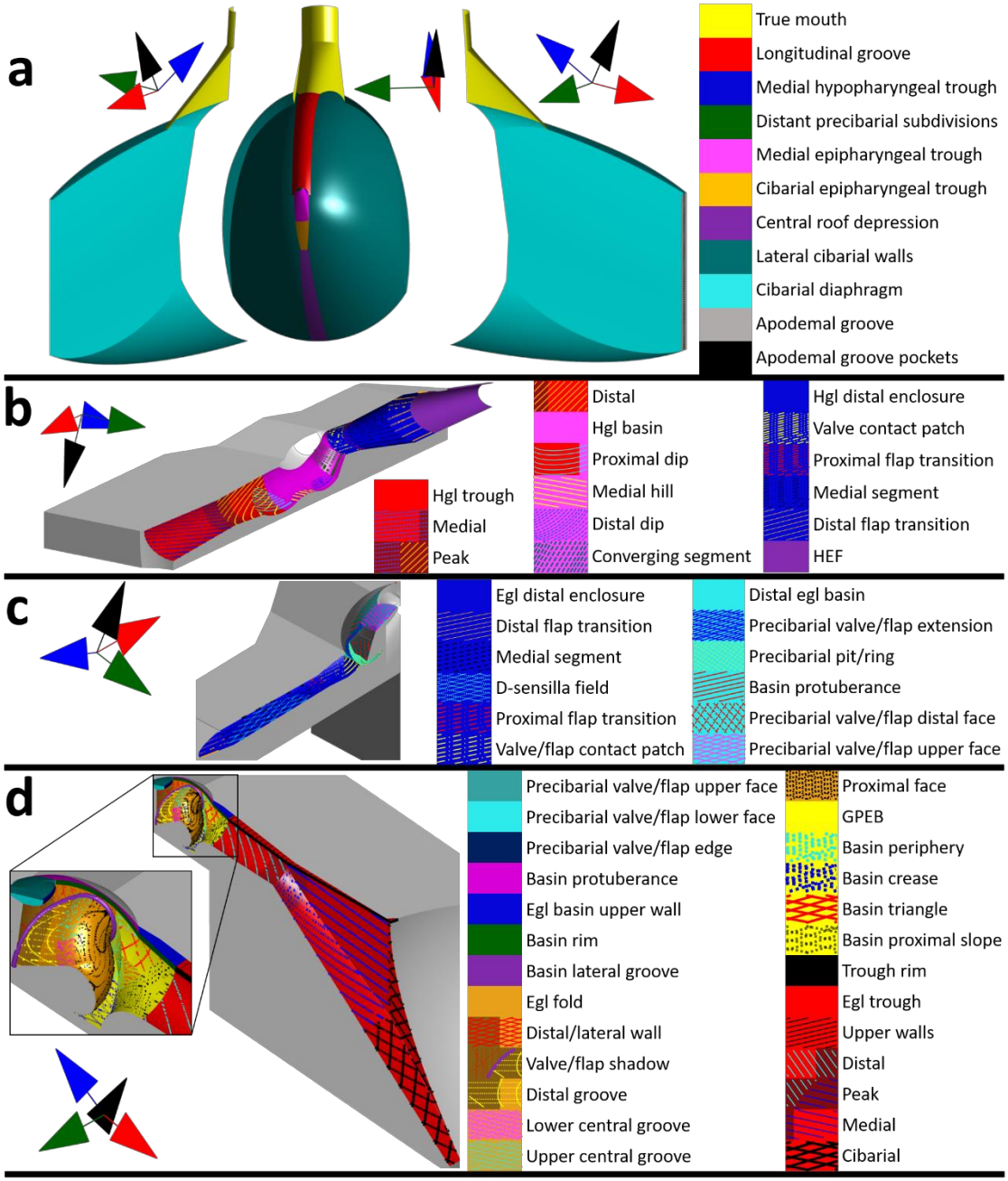
a
True mouth
Longitudinal groove
Medial hypopharyngeal trough
Distant precibarial subdivisions
Medial epipharyngeal trough
Cibarial epipharyngeal trough
Central roof depression
Lateral cibarial walls
Cibarial diaphragm
Apodemal groove
Apodemal groove pockets
b
Hgl trough
Medial
Peak
Distal
Hgl basin
Proximal dip
Medial hill
Distal dip
Converging segment
Hgl distal enclosure
Valve contact patch
Proximal flap transition
Medial segment
Distal flap transition
HEF
c
Egl distal enclosure
Distal flap transition
Medial segment
D-sensilla field
Proximal flap transition
Valve/flap contact patch
Distal egl basin
Precibarial valve/flap extension
Precibarial pit/ring
Basin protuberance
Precibarial valve/flap distal face
Precibarial valve/flap upper face
d
Precibarial valve/flap upper face
Precibarial valve/flap lower face
Precibarial valve/flap edge
Basin protuberance
Egl basin upper wall
Basin rim
Basin lateral groove
Egl fold
Distal/lateral wall
Valve/flap shadow
Distal groove
Lower central groove
Upper central groove
Proximal face
GPEB
Basin periphery
Basin crease
Basin triangle
Basin proximal slope
Trough rim
Egl trough
Upper walls
Distal
Peak
Medial
Cibarial

Figure 3.4 Fine resolution terminology for the cibarium and precibarium of the blue-green sharpshooter. In this figure, all model views are internal. A) Cibarium bowl (concave, with the cibarial diaphragm and true mouth split outward, like classic plantation shutters (concave). B) Left half of the hgl precibarium (concave). C) Left half of the egl distal enclosure (concave) and distal egl basin (partially concave and partially convex). D) Left half of the egl trough and part of the egl basin (the egl fold and basin protuberance are convex, and the rest is concave). The egl fold lateral groove was modified for the sake of illustration. The coordinate axes indicate anterior → posterior, distal → proximal (for the trough), ventral → dorsal, and left → right. The gray 3D parts of subfigures b - d are abstract representations of the epipharynx and hypopharynx. Hgl: hypopharyngeal; egl: epipharyngeal; GPEB: groove at the proximal end of the basin; HEF: hypopharyngeal extension that inserts into the stylet food canal.

Our model of the precibarium is more precise than that of the cibarium. For example, the view of the egl basin in Figure 3.1c reveals a segment under the precibarial valve/flap that is shaped like a triangle pointing downward. This triangular segment represents the inward extension of the basin central groove, which is inferred to be deeper toward the precibarial valve/flap. The segment of the model to the right of the downward pointing triangle, which also protrudes below the rest of the basin, is part of the groove at the proximal end of the basin. While the shapes of this groove and the basin central groove are not perfectly accurate, they serve to account for stagnation zones when fluid flows in and out of the precibarium. Similarly, the precibarial pit/ring (Figure 3.3a and Figure 3.3c) serves as a pocket with an imprecise shape that accounts for a predicted stagnation zone.

The precibarial trough segment (Figure 3.3a) exhibits the essential widening toward the cibarium, while ignoring the flared shape that is present in SEMs (Figure 3.3b and Figure 3.3c). This will allow for order of magnitude predictions of fluid drag forces, while

avoiding the time and computational costs of designing a 3D model that flares toward the cibarium. In these ways, the 3D model balances complexity with cost.

The precibarium is speculated to be the portion of the foregut where most bacterial detachment occurs during insect feeding. Thus, it is appropriate that the precibarial segment of our 3D model was constructed with more attention to fine-resolution details, allowing for more precise estimation of fluid dynamics in this segment in future studies. In the following section, the morphology of the 3D model, particularly in the precibarium, is cross-referenced with the corresponding anatomical segments observed in the SEMs.

3.2.3 Fine-Scale Spatial-Resolution Terms for the Precibarium and Cibarium

We present in Figure 3.4 and Figure 3.5 finer resolution terminology than described in the Introduction and new terms intended to aid in describing biofilm spatial patterns and fluid dynamics. When new terminology is introduced, it is denoted as ‘proposed herein’ (PH).

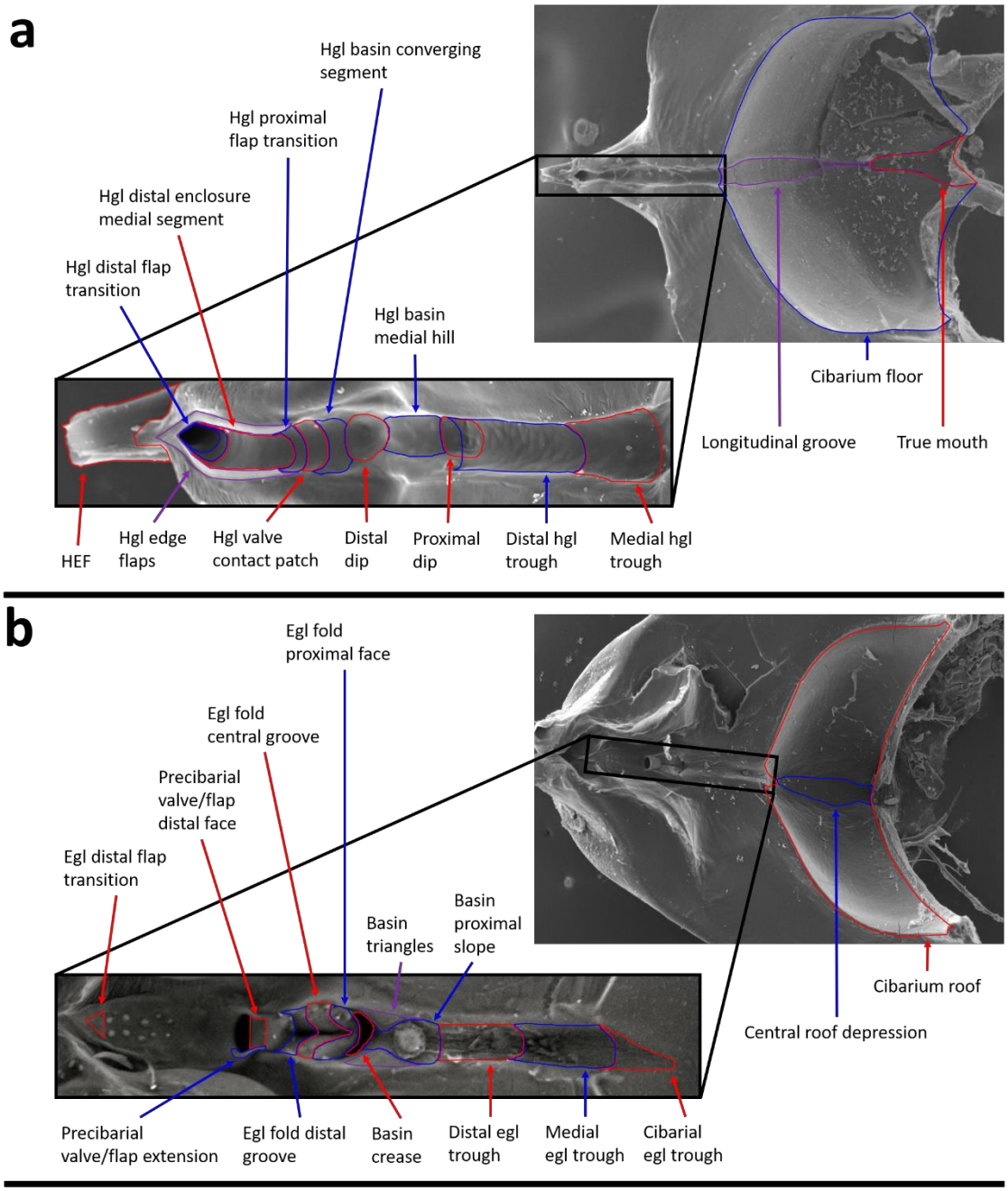
a
Hgl basin converging segment
Hgl proximal flap transition
Hgl distal enclosure medial segment
Hgl distal flap transition
Hgl basin medial hill
Cibarium floor
Longitudinal groove
True mouth
HEF
Hgl edge flaps
Hgl valve contact patch
Distal dip
Proximal dip
Distal hgl trough
Medial hgl trough
b
Egl fold proximal face
Egl fold central groove
Precibarial valve/flap distal face
Egl distal flap transition
Basin triangles
Basin proximal slope
Cibarium roof
Central roof depression
Precibarial valve/flap extension
Egl fold distal groove
Basin crease
Distal egl trough
Medial egl trough
Cibarial egl trough

Figure 3.5 Fine resolution terminology for the precibarium and cibarium of the blue-green sharpshooter, labeled using scanning electron micrographs. A) Hypopharynx. The electron microscope image on the top right was adapted from a previous publication (Reprinted with permission from Rapicavoli et al. 2015; copyright © American Society for Microbiology, [*Appl. Environ. Microbiol.* 81, no. 23 (2015): 8145-8154 10.1128/AEM.02383-15]). B) Epipharynx. hgl: hypopharyngeal; egl: epipharyngeal; HEF: hypopharyngeal extension that inserts into the stylet food canal.

In Figure 3.4a, the anterior/dorsal view of the cibarium bowl reveals an alternative way of describing cibarium segments that are illustrated in Figure 3.2. The cibarium bowl can be divided into the longitudinal groove, central roof depression (PH), and lateral cibarial walls (PH) instead of the cibarium roof and cibarium floor. Figure 3.4a also reveals a portion of the precibarium: the cibarial epipharyngeal trough (PH), medial epipharyngeal trough (PH), and medial hypopharyngeal trough (PH) are visible (see also Figure 3.5).

The hypopharyngeal (hgl) precibarial wall segments presented in Figure 3.3b can be subdivided (Figure 3.4b and Figure 3.5a). The hgl trough is composed of the medial and distal subdivisions (PH), which meet at the hgl trough peak (PH). The proximal dip (PH) straddles the hgl trough and hgl basin, which have boundaries that are based on the boundaries of the epipharyngeal trough and epipharyngeal basin. The hgl basin contains the medial hill, distal dip, and converging segments (PH). The hgl basin meets the hgl distal enclosure at the distal edge of the converging segment.

The hgl distal enclosure is composed of the hgl valve/flap contact patch (PH), hgl proximal flap transition (PH), hgl medial segment of the distal enclosure (PH), and hgl distal flap transition (PH). The hgl valve/flap contact patch is the portion of the wall that remains bare of *X. fastidiosa* after a shag carpet-like biofilm develops. The hgl proximal

flap transition is demarcated by the region where the hgl edge flaps (PH) transition to their full width. The hgl medial segment of the distal enclosure is demarcated by the region where the hgl edge flap widths and the distance between the left and right edge flaps remain relatively constant. The hgl distal flap transition is demarcated by the region where the distance between the left and right hypopharyngeal edge flaps decreases, making the shape of a triangle.

The epipharyngeal (egl) precibarial wall segments presented in Figure 3.3c can also be subdivided (Figure 3.4c, Figure 3.4d, and Figure 3.5b). The egl trough is composed of the cibarial, medial, distal, upper (dorsal/posterior) walls, and rim subdivisions (PH). The cibarial and medial subdivisions are separated by an imaginary plane where the rim of the trough meets the cibarium that is perpendicular to the precibarial trough centerline. The medial and distal subdivisions meet at the egl trough peak (PH).

The egl basin is divided into five segments (Figure 3.4c, Figure 3.4d, and Figure 3.5b): 1) the groove at the proximal end of the basin, 2) the egl fold (PH), 3) the rim of the basin, 4) the egl basin upper (dorsal/posterior) walls (PH), and 5) the distal egl basin (PH). The groove at the proximal end of the basin (GPEB) contains the triangles, proximal slope, crease, and periphery segments (PH). The basin proximal slope is the segment of the GPEB proximal to the basin triangles, which is shaped like a rounded groove of a pulley. The proximal end of the basin proximal slope is demarcated by a transition from the tubular shape of the distal egl trough to the shape of a pulley groove. The distal end of the basin proximal slope is demarcated by a reversal in the concavity of the GPEB wall. The remaining portions of the GPEB walls form the crease and periphery segments. In our 3D

model, the basin periphery is mostly in the space between the basin triangles and egl fold (PH). The boundaries of the GPEB were altered from their original limits herein to allow for more precise and simplified naming conventions.

The egl fold (Figure 3.4d, Figure 3.5b) contains the proximal face (PH), central groove, distal groove (PH), distal/lateral wall (PH), and lateral groove (PH). The central groove is demarcated proximally by the edge of the rounded proximal face. It is demarcated distally by the widening of the distal groove. The central groove contains lower (ventral) and upper (dorsal) segments (PH), demarcated by the opening of the central groove. The distal groove contains a region that remains hidden behind the precibarial valve/flap in dorsal/distal views of the egl basin. This region is the valve/flap shadow (PH). The distal/lateral wall of the egl fold is composed of wall segments that may form a concave shape at the distal and lateral ends of the epipharyngeal fold. The lateral groove separates the distal/lateral wall from the remainder of the egl fold.

The distal egl basin contains the basin protuberances (PH), the precibarial valve/flap, and the precibarial pit/ring. The precibarial valve/flap contains the lower (ventral) face, edge, upper (dorsal) face, distal face, and extension segments (PH). The precibarial valve/flap extension begins at the distal edge of the upper face and wraps around the sides of the precibarial pit/ring.

At the distal edge of the precibarial pit/ring, the distal egl basin meets the egl distal enclosure. The egl distal enclosure is composed of the egl valve/flap contact patch (PH), egl proximal flap transition (PH), egl medial segment of the distal enclosure (PH), and egl distal flap transition (PH). The boundaries of these segments are delimited by their apposed

segments on the hypopharynx. The egl medial segment of the distal enclosure includes the D-sensilla field.

3.3 Discussion

The understanding of hemipteran feeding anatomy and physiology has advanced greatly since the time of Snodgrass (1935), an original authority for insect anatomy, principally through development of new technologies like electron and confocal microscopy and EPG. In-depth anatomical descriptions and terminology has often not kept pace. Herein, our goal was to remedy this problem and provide a foundation for future fluid dynamics studies. For example, the term 'functional foregut' was recently enlarged to include the food canal, because fluid flow is continuous through the stylet food canal, precibarium, and cibarium [10,23] . However, in this paper and future ones, we recommend reverting back to the earlier definition because the foregut is internal to the head of an insect [19], while the mouth parts are not. Also, although there are anatomical synonyms for the functional foregut (e.g., the buccal cavity and preoral cavity), here we exclusively used functional foregut because it emphasizes functionality and is commonly referenced in the *X. fastidiosa*-sharpshooter literature [12,20,23-25].

The foregut functionality we highlight is that of fluid movements, which are highly dynamic in this area of the complete foregut. Fluids can be taken up into the functional foregut, moved around, then either ejected (termed egestion) or separate boluses of fluid can be swallowed past the true mouth. Egestion and ingestion are the fluid movements that are most important for *X. fastidiosa* inoculation and acquisition, respectively. While *X.*

fastidiosa-like bacteria have been observed in both the stylet food canal and true foregut, colonization patterns have been described mainly in the precibarium and cibarium of sharpshooters [6,7,11,15,16]. Studies and hypotheses to date support that the cibarial dilator and precibarial valve muscles provide the sole propulsive power to cause egestion and concomitant inoculation of bacteria that have colonized the precibarium and cibarium [19,20]. There is no evidence that bacteria can be inoculated from the true foregut, which is not included in our 3D model.

Recent SEM observations of the spittlebug, *Philaenus spumarius* [26], revealed precibarial anatomy and lumenal structures nearly identical to those of sharpshooters. There are two sets of gustatory organs separated by the precibarial valve, which can open via action of a tiny precibarial valve muscle. The arrangement facilitates two-stage tasting of fluids brought into the precibarium. This similarity in separation of gustatory organs is not surprising, because such an orientation has been found in all hemipterans examined [27, E.A.B. unpub. data,28,29]. Extensive light microscopy and transmission electron microscopy of the precibarial valve interior of spittlebugs by Ruschioni et al. (2019) revealed a previously undescribed bell-like invagination whose opening is the precibarial pit (termed ring in that paper). The precibarial valve muscle is attached to the bell-shaped invagination in spittlebugs, unlike the proposed attachment directly to the pit/ring and flap in sharpshooters, as hypothesized by Backus and McLean (1982). Thus, while the flap was considered the actual valve by Backus and McLean (1982), Ruschioni et al. (2019) call the entire assembly the valve, with the flap only a part thereof. It is not yet known whether the lumenal structures of sharpshooters have similar internal anatomy to those of spittlebugs,

despite their similar external, lumenal appearances. Because of this terminological uncertainty, herein we referred to the precibarial valve/flap until the interiors of sharpshooter structures are studied using transmission electron microscopy.

In the past, broad understanding of sharpshooter functional foregut anatomy was not always sufficiently detailed for studies of the involvement of precibarial structures in *X. fastidiosa* acquisition and inoculation. Biofilm spatial patterns in the precibarium and cibarium are nuanced and have a finer resolution than the originally applied anatomical understanding [7,11,15]. Our study will allow for higher resolution descriptions of biofilm spatial patterns and fluid dynamics.

In conclusion, we had two objectives for this work. First, we introduced the 3D model, which mimics geometric complexity of the auchenorrhynchan/sharpshooter hemipteran functional foregut with finer spatial resolution than any previous model. The model is based on published microscopy images of blue-green sharpshooters from different geographical regions and likely different sexes. Second, we used the 3D model to synthesize the existing anatomical understanding of the sharpshooter foregut and propose new terminology, equipping multidisciplinary researchers to become proficient in anatomical details. These details will provide finer resolution and delimited boundaries to aid in describing the precise locations of *X. fastidiosa* biofilm formation sites. Both our new 3D model and the enhanced anatomical understanding will be helpful for future fluid dynamic studies of the functional foregut, which have essentially trended in the direction of determining flow characteristics with increasing spatial resolution [6,12,14,26]. An enhanced ability to model fluid dynamics and describe biofilm spatial patterns in blue green

sharpshooters will allow us to evaluate how physical forces affect *X. fastidiosa* acquisition, retention, and inoculation. Increased understanding in these areas could lead to new targets for preventing diseases caused by *X. fastidiosa*.

3.4 Methods

3.4.1 3D model construction

A 3D model of the blue-green sharpshooter functional foregut (and true mouth) was created using COMSOL Multiphysics (COMSOL, Inc., Stockholm, Sweden) based on a meta-analysis of previously published microscopy images of sharpshooters. The analyzed microscopy images were of insects from different geographical regions and likely different sexes. The model incorporates over 30 dimensions collected from the literature (Appendix C, Table C.1.1). The 3D model dimensions are consistent with those of Ranieri et al., as described in Appendix C[12].

Segments of the model were isolated and meshed in COMSOL Multiphysics. Meshes were exported as STL files that were interpreted in MATLAB (MathWorks, Inc., Natick, MA) as triangulations. Triangulations were displayed in Figure 3.1 – Figure3.5 using content from MATLAB Central's File Exchange[30-32].

3.4.2 Scanning electron microscopy

The morphology in this article is illustrated with a mix of previously published and unpublished scanning electron micrographs from the Rapicavoli et al. (2015) study. Detailed methods can be found therein. In brief, blue-green sharpshooter heads were dehydrated and critical point dried using a series of ethanol dilutions. Functional foreguts

were dissected from insect heads, mounted, coated with a platinum-palladium mixture, and imaged using a Philips XL30 field emission gun (FEG) scanning electron microscope (FEI, Hillsboro, OR).

3.4.3 Directional terms

Directional terms are illustrated using the coordinate axes in Figure 3.2a. Anterior and posterior point toward the space in front of and behind the insect, respectively. Note that, unlike most insects, sharpshooters (like other leafhoppers) have opisthognathous heads; that is, they are affixed under the head and pointed backwards. Thus, the mouthparts are unintuitively oriented posterior-ward (Figure 3.2a). Ventral and dorsal point toward the space below and above the insect in Figure 3.2a, respectively. Proximal and distal indicate a position that is close to and distant from an orientation site, respectively, and are used to describe progression and regression (respectively) along the ingestion route through the stylet food canal, functional foregut, and true mouth [20]. Also, left and right are used to indicate direction from the insect's perspective in later subfigures.

Another important aspect of the fine resolution terminology is its cross-applicability to sharpshooter species besides the blue-green sharpshooter. Despite defining directional terms above, anatomical names that include the words "posterior," "anterior," "dorsal," and "ventral" are avoided herein because the relationship between the functional foregut orientation and these directional terms varies for different sharpshooter species. For example, the 3D model of the functional foregut in Figure 3.2a would need to be rotated around 30 degrees clockwise relative to the coordinate axes for these terms to be appropriately applied to the cibarium of the glassy-winged sharpshooter, *Homalodisca*

vitripennis (Germar, 1821). If blue-green sharpshooter anatomy were labeled using coordinate axes that vary between species, then studies of *X. fastidiosa* colonization patterns that compare multiple sharpshooter species could be unnecessarily complicated. Therefore, the terminology proposed herein uses the terms “upper” and “lower” where the terms “posterior,” “anterior,” “dorsal,” and “ventral” could not otherwise be avoided.

3.5 References

1 Backus, E. A., Cervantes, F. A., Guedes, R. N. C., Li, A. Y. & Wayadande, A. C. AC–DC electropenetrography for in-depth studies of feeding and oviposition behaviors. *Annals of the Entomological Society of America* **112**, 236-248 (2019).

2 Purcell, A. H. & Finlay, A. Evidence for noncirculative transmission of Pierce's disease bacterium by sharpshooter leafhoppers. *Phytopathology* **69**, 393-395 (1979).

3 Lindow, S. Money matters: fueling rapid recent insight into *Xylella fastidiosa*—an important and expanding global pathogen. *Phytopathology* **109**, 210-212 (2019).

4 Tumber, K., Alston, J. & Fuller, K. Pierce's disease costs California $104 million per year. *California Agriculture* **68**, 20-29 (2014).

5 McKamey, S. Taxonomic catalogue of the leafhoppers (Membracoidea). Part 1. Cicadellinae. *Memoirs of the American entomológical Institute* **78**, 1-394 (2007).

6 Purcell, A. H., Finlay, A. H. & McLean, D. L. Pierce's disease bacterium: mechanism of transmission by leafhopper vectors. *Science* **206**, 839-841 (1979).

7 Almeida, R. P. & Purcell, A. H. Patterns of *Xylella fastidiosa* colonization on the precibarium of sharpshooter vectors relative to transmission to plants. *Annals of the Entomological Society of America* **99**, 884-890 (2006).

8 Newman, K. L., Almeida, R. P., Purcell, A. H. & Lindow, S. E. Cell-cell signaling controls *Xylella fastidiosa* interactions with both insects and plants. *Proceedings of the National Academy of Sciences* **101**, 1737-1742 (2004).

9 Backus, E. A., Shugart, H. J., Rogers, E. E., Morgan, J. K. & Shatters, R. Direct evidence of egestion and salivation of *Xylella fastidiosa* suggests sharpshooters can be "flying syringes". *Phytopathology* **105**, 608-620 (2015).

10 Backus, E. A. & Shih, H.-T. Review of the EPG waveforms of sharpshooters and spittlebugs including their biological meanings in relation to transmission of *Xylella fastidiosa* (Xanthomonadales: Xanthomonadaceae). *Journal of Insect Science* **20**, 6; 1-14 (2020).

11 Backus, E. A. & Morgan, D. J. Spatiotemporal colonization of *Xylella fastidiosa* in its vector supports the role of egestion in the inoculation mechanism of foregut-borne plant pathogens. *Phytopathology* **101**, 912-922 (2011).

12 Ranieri, E. *et al.* Fluid dynamics in the functional foregut of xylem-sap feeding insects: a comparative study of two *Xylella fastidiosa* vectors. *Journal of Insect Physiology* **120**, 103995 (2020).

13 Andersen, P. C., Brodbeck, B. V. & Mizell III, R. F. Feeding by the leafhopper, *Homalodisca coagulata*, in relation to xylem fluid chemistry and tension. *Journal of Insect Physiology* **38**, 611-622 (1992).

14 Rapicavoli, J. N. *et al.* O antigen modulates insect vector acquisition of the bacterial plant pathogen *Xylella fastidiosa*. *Appl. Environ. Microbiol.* **81**, 8145-8154 (2015).

15 Alves, E. *et al.* Retention sites for *Xylella fastidiosa* in four sharpshooter vectors (Hemiptera: Cicadellidae) analyzed by scanning electron microscopy. *Current Microbiology* **56**, 531-538 (2008).

16 Brlansky, R., Timmer, L., French, W. & McCoy, R. Colonization of the sharpshooter vector, *Oncometopia nigricans* and *Homalodisca coagulata* by xylem-limited bacteria. *Phytopathology* **73**, 530-535 (1983).

17 Backus, E. A. & McLean, D. L. The sensory systems and feeding behavior of leafhoppers. I. The aster leafhopper, *Macrosteles fascifrons* stål (Homoptera, Cicadellidae). *J Morphol* **172**, 361-379 (1982).

18 Backus, E. A. & McLean, D. L. The sensory systems and feeding behavior of leafhoppers. II. A comparison of the sensillar morphologies of several species (Homoptera: Cicadellidae). *Journal of morphology* **176**, 3-14 (1983).

19 Snodgrass, R. E. *Principles of Insect Morphology*. First edn, (New York, London, McGraw-Hill Book Company, Inc., 1935).

20 Backus, E. A. in *Vector-Mediated Transmission of Plant Pathogens* (ed JK Brown) 175-193 (Am Phytopath Society, 2016).

21 Backus, E. A. Sensory systems and behaviours which mediate hemipteran plant-feeding: a taxonomic overview. *Journal of Insect Physiology* **34**, 151-165 (1988).

22 Purcell, A. H. & Almeida, R. P. Role of bacterial attachment in transmission of *Xylella fastidiosa* by the glassy-winged sharpshooter, and other factors affecting transmission efficiency. in *Pierce's Disease Research Symposium*. 168 - 170 (2003).

23 Krugner, R., Sisterson, M. S., Backus, E. A., Burbank, L. P. & Redak, R. A. Sharpshooters: a review of what moves *Xylella fastidiosa*. *Austral Entomology* **58**, 248-267 (2019).

24 Sengoda, V. G., Shi, X., Krugner, R., Backus, E. A. & Lin, H. Targeted mutations in *Xylella fastidiosa* affect acquisition and retention by the glassy-winged sharpshooter, *Homalodisca vitripennis* (Hemiptera: Cicadellidae). *Journal of Economic Entomology* **113**, 612-621 (2020).

25 Rapicavoli, J. N. *Structural and functional characterization of the Xylella fastidiosa O antigen: contribution to bacterial virulence, insect transmission, and modulation of innate immune recognition in grapevine.* Doctor of Philosophy thesis, UC Riverside, (August 2016).

26 Ruschioni, S. *et al.* Functional anatomy of the precibarial valve in *Philaenus spumarius* (L.). *PLoS ONE* **14**, e0213318, doi:10.1371/journal.pone.0213318 (2019).

27 Ullman, D. E. & McLean, D. L. Anterior alimentary canal of the pear Psylla, *Psylla pyricola* foerster (Homoptera, Psyllidae). *Journal of morphology* **189**, 89-98 (1986).

28 Wensler, R. J. & Filshie, B. K. Gustatory sense organs in the food canal of aphids. *Journal of Morphology* **129**, 473-491 (1969).

29 McLean, D. L. & Kinsey, M. G. The precibarial valve and its role in the feeding behavior of the pea aphid, *Acyrthosiphon pisum*. *Bulletin of the ESA* **30**, 26-31 (1984).

30 Diana. Color blind friendly colormap. *MATLAB Central File Exchange.* Retrieved August 2019 https://www.mathworks.com/matlabcentral/fileexchange/46802-color-blind-friendly-colormap (2014).

31 Ikuma, K. Hatchfill2. *MATLAB Central File Exchange.* Retrieved September 2019 https://www.mathworks.com/matlabcentral/fileexchange/53593-hatchfill2 (2018).

32 Johnson, E. A. Arrow. *MATLAB Central File Exchange.* Retrieved February 2019 https://www.mathworks.com/matlabcentral/fileexchange/278-arrow (2016).

Chapter 4

Simulating Fluid Dynamics in Representative Systems

Marcus, I. M., White, D., Backus, E.A., Roper, M.C. Walker, S. L. Fluid Dynamics Simulations Suggest Novel Targets for Fighting Plant Diseases Caused by *Xylella fastidiosa* Bacteria. In preparation for submission.

Abstract

Xylella fastidiosa is a multicontinental plant pathogenic bacterium that is vectored from plant to plant by sharpshooter leafhoppers and other xylem-feeding hemipteran insects. The bacterium forms biofilms in plant xylem and the insect vector functional foregut. There are varying hypotheses for mechanisms of *X. fastidiosa* transmission reported in the literature. In this paper, transmission via flow driven detachment mechanisms is supported using novel 3D fluid dynamic simulations of grapevine xylem and the blue-green sharpshooter functional foregut. Analysis of simulation results is informed by previously reported *X. fastidiosa* colonization patterns in the functional foregut and sharpshooter feeding behaviors. The analysis supports a model of how fluid dynamics influence *X. fastidiosa* transmission and virulence.

4.1 Introduction

Pierce's disease (PD) of grapevines costs California's grape growers an estimated $56 million per year in lost production and vine replacement[1]. The disease is caused by the bacterium *Xylella fastidiosa*, which is spread by xylem-feeding hemipteran insect vectors[2]. *Xylella fastidiosa* forms biofilms in the functional foreguts (precibaria and cibaria) of vectors, including the glassy-winged sharpshooter (GWSS) and the blue-green sharpshooter (BGSS)[3,4]. The GWSS has been the most destructive vector of PD in California in recent decades[5], though the California native BGSS is also an important

vector of the bacterium among others[1]. The BGSS was used as the model vector for this study because there is larger breadth of information on its physiology[3,6-10].

Biofilms are surface-attached microbial communities encased in a self-produced matrix[11]. During BGSS feeding, *X. fastidiosa* cells are putatively detached from biofilms in the functional foregut, are carried by moving xylem sap, and are inoculated into xylem vessels[4,12]. Inoculation is linked with egestion, during which xylem sap is pumped from the cibarium, through the precibarium, and out the stylet (Fig. 1)[12]. Conversely, the flow path is reversed during ingestion, which is linked with acquisition of *X. fastidiosa* in the functional foregut[13].

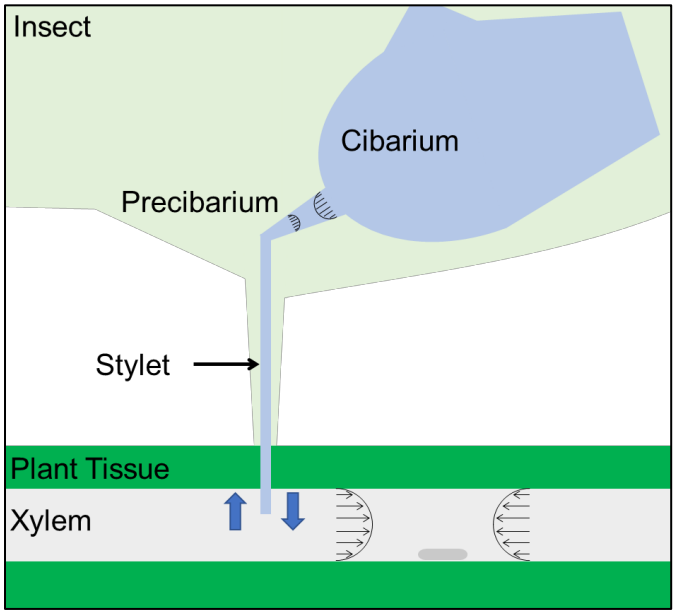

Figure 4.1: Fluid flow pathways between the plant xylem and functional foregut (precibarium and cibarium). Conceptual fluid velocity profiles are illustrated in the xylem and precibarium for ingestion and egestion. This figure is not drawn to scale.

It is hypothesized that high egestion flowrates physically detach *X. fastidiosa* from the BGSS functional foregut, resulting in inoculation[6]. This inoculation mechanism can be

evaluated by simulating fluid dynamics in the BGSS functional foregut during egestion and comparing the results with the drag forces required to detach *X. fastidiosa*. Current models of flow in the insect functional foregut do not simulate egestion and lack the geometric fidelity required for nuanced estimation of drag forces acting on bacteria[6,7,14]. Here, functional foregut fluid dynamics during egestion were simulated using a 3D model of the BGSS functional foregut[15] appropriate for nuanced drag force predictions. Functional foregut fluid dynamics during ingestion were also simulated to gain understanding about *X. fastidiosa* acquisition from infected xylem vessels.

BGSS feeding causes fluid drag forces in xylem vessels at the same time that it causes fluid drag forces in the functional foregut (Fig. 1). Thus, insect feeding may cause detachment of *X. fastidiosa* from plant xylem walls, an important step in bacterial acquisition. To our knowledge, fluid dynamics that occur in xylem during insect feeding have not been previously simulated, nor have the drag forces acting on wall-attached bacteria been calculated. These fluid dynamics would intuitively affect xylem-dwelling biofilms if the drag forces acting on them are comparable to or greater than those present before the vessels are disturbed by insect feeding (termed undisturbed xylem herein).

Bouda, et al.[16] made estimations of undisturbed xylem flow in one-year old grapevine using the Hagen-Poiseuille equation. This equation predicts total flowrates in cylindrical pipes based on the viscosity of the liquid, the pressure gradient along the pipe length, and the radius of the pipe. Based on their analysis, simulations of xylem flow with a uniform pressure gradient across different xylem vessels provided representative predictions in narrow xylem vessels and overpredicted flowrates in wide vessels by an

average of 23%. Thus, simulations of xylem flow in grapevine using the Hagen-Poiseuille equation and the average xylem pressure gradient should allow order of magnitude predictions of undisturbed xylem flowrates. However, these flowrates would not provide the resolution required to estimate drag forces acting on surface-attached bacteria, which require estimations of fluid shear rates.

Instead, shear rates can be predicted in simulations based on the Navier Stokes equations. These are equations that can be used to derive the Hagen-Poiseuille equation. Similar to the Hagen-Poiseuille equation, the Navier Stokes equations require input of the axial pressure gradient to predict flowrates. Previous simulations of xylem flow using the Navier Stokes equations have used the water potential gradient in place of the pressure gradient, though the water potential gradients were not based on direct experimental measurements[17]. The water potential gradient is a more complete measure of xylem flow driving force than the pressure gradient. The water potential gradient has been reported as 0.03 MPa/m for both well-watered and water-stressed grapevines[18]. We used this reported gradient together with the Navier Stokes equations to predict drag forces acting on surface-attached bacteria in undisturbed grapevine xylem.

In this study, we used novel fluid dynamics simulations to investigate the role of physical forces on *X. fastidiosa* transmission (acquisition and inoculation). Grapevine xylem simulations predicted drag forces acting on bacteria in the xylem during insect feeding and during undisturbed conditions. BGSS functional foregut simulations predicted fine scale drag forces during ingestion and egestion. In this paper, the resulting BGSS drag force profiles are compared with condensed versions of previously reported spatial

colonization patterns in the functional foregut. Simulation and comparison results support new mechanistic insights about pathogen virulence and disease transmission.

4.2 Results

4.2.1 Xylem Simulations

We simulated fluid dynamics in undisturbed grapevine xylem, defined herein as xylem that is not being fed on by insects (Fig. 2, *Undisturbed*)[18]. The *Undisturbed* results indicate that drag forces in undisturbed xylem increase with increasing vessel diameter. The predicted drag forces are not high enough to detach individually surface-attached bacteria, assuming *X. fastidiosa* adhesive forces when adhered to xylem walls are similar to those reported when *X. fastidiosa* is adhered to glass in microfluidic studies[19]. However, drag forces may be high enough to detach bacteria in later stages of biofilm development. *Xylella fastidiosa* biofilm stiffness decreases over time in vitro[20]. Aggregates can detach from biofilms and move downstream under flow conditions simulating those in undisturbed xylem vessels[20].

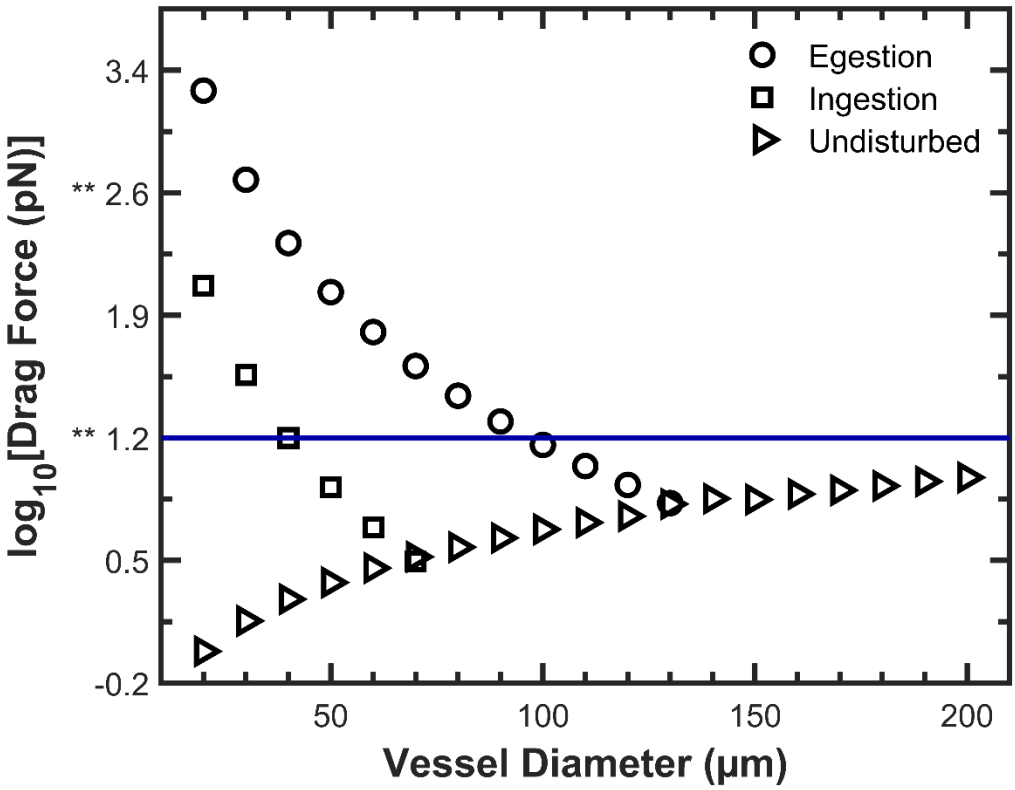

Figure 4.2: Simulated drag forces acting on individually surface-attached bacteria in grapevine xylem vessels. Egestion and Ingestion represent simulated fluid flow for insect-xylem interactions during egestion and ingestion, respectively. Undisturbed represents simulated undisturbed xylem vessels by modeling the water tension gradient as a pressure gradient. The ** symbols on the y-axis are references to key drag forces in the results of a previous microfluidic study[19]. The blue horizontal line is a visual aid at $10^{1.2}$ pN (15.85 pN). It represents the drag force where less than 1% of individually surface-attached Xylella fastidiosa cells detached in De La Fuente, et al. (2007)[19]. When the drag forces in that same study were sequentially increased, over 70% of X. fastidiosa detached by the time the drag forces reached $10^{2.6}$ pN (443.8 pN)[19].

We also simulated fluid dynamics for xylem vessels during insect feeding, when ingested and egested fluids flow to and from the insect stylet that penetrates a xylem vessel. Calculated drag forces are greater than or equal to those in undisturbed xylem for vessels smaller than 80 µm and 140 µm during ingestion and egestion, respectively (Fig. 4.2;

Ingestion, *Egestion*). For vessels smaller than 80 μm, predicted drag forces are 14 times higher during egestion than during ingestion. The difference between insect-driven drag forces (*Ingestion, Egestion*) and undisturbed xylem drag forces (*Undisturbed*) in vessels of a given diameter decreases with increasing vessel diameter.

4.2.2 Insect Simulations

We also created fluid dynamic simulations for the insect precibarium and cibarium. Full plots of simulation results can be found in Appendix D. Results herein focus on the precibarium due to its relevance for disease transmission[3]. Simulation results are plotted as heat maps within 3D molds[15] that resemble segments of the epipharynx and hypopharynx (Fig. 4.3). The heat map color represents the calculated drag force experienced by an individually surface-attached bacterium at a given location.

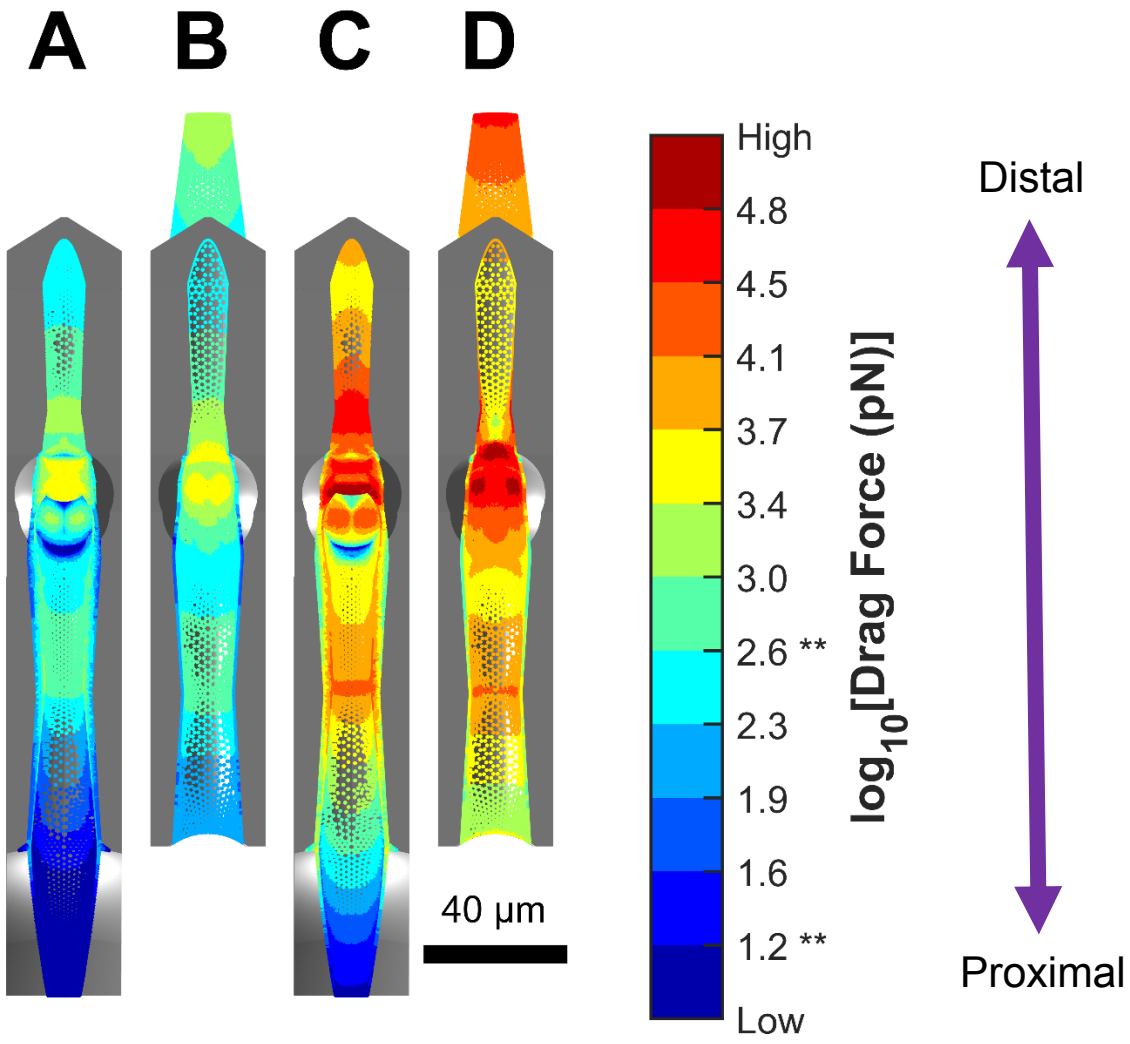

Figure 4.3: Heat maps of simulated drag forces acting on individually surface-attached bacteria in the blue-green sharpshooter precibarium during feeding. Drag forces are plotted within gray 3D models of segments of the epipharynx (A & C) and hypopharynx (B & D), which are similar to previously described 3D models[21]. During ingestion (A & B), drag forces are generally lower than during egestion (C & D). The ** symbols on the colormap are references to key drag forces in the results of a microfluidic study[19]. $10^{1.2}$ pN (15.85 pN) is the drag force where less than 1% of individually surface-attached Xylella fastidiosa cells detached in De La Fuente, et al. (2007)[19]. When the drag forces in that same study were sequentially increased, over 70% of X. fastidiosa detached by the time the drag forces reached $10^{2.6}$ pN (443.8 pN)[19].

There are four segments of the precibarium with predicted drag forces under $10^{1.2}$ pN during both ingestion and egestion (referred to as "low predicted drag forces" herein): the precibarial pit/ring, the valve shadow, the basin crease, and the proximal end of the cibarial epipharyngeal trough. $10^{1.2}$ pN (15.85 pN) is the drag force where less than 1% of individually surface-attached *X. fastidiosa* cells detached in a microfluidic study[19]. When the drag forces in that same study were sequentially increased, over 70% of *X. fastidiosa* detached by the time the drag forces reached $10^{2.6}$ pN (443.8 pN)[19]. In Fig. 3, several segments of the precibarium are predicted to experience drag forces more than 1.5 orders of magnitude higher than $10^{2.6}$ pN during egestion. These include the epipharyngeal trough peak, hypopharyngeal trough peak, and the epipharyngeal valve contact patch. Thus, there are segments in the precibarium where bacteria are predicted to detach during egestion and there are segments with no predicted detachment during egestion.

4.2.3 Colonization Patterns

Almeida and Purcell previously observed colonization patterns of *X. fastidiosa* in the precibaria of blue-green sharpshooters after a two-day incubation period (one-day acquisition access period and a one-day inoculation period)[3]. Their results were recorded in a collection of twelve diagrams. We condensed these diagrams into one for comparison with drag forces predicted by our simulations (Fig. 4.4, A & B). Similarly, colonization patterns described and observed for developed *X. fastidiosa* precibarial biofilms (at least 11 days of incubation) in the literature[3,8,9,22] were condensed onto 3D plots of the precibarium (Fig. 4.4, C & D). For a comprehensive description of how precibarial anatomy compares between the BGSS and the 3D model, see White, et al. (2021)[15].

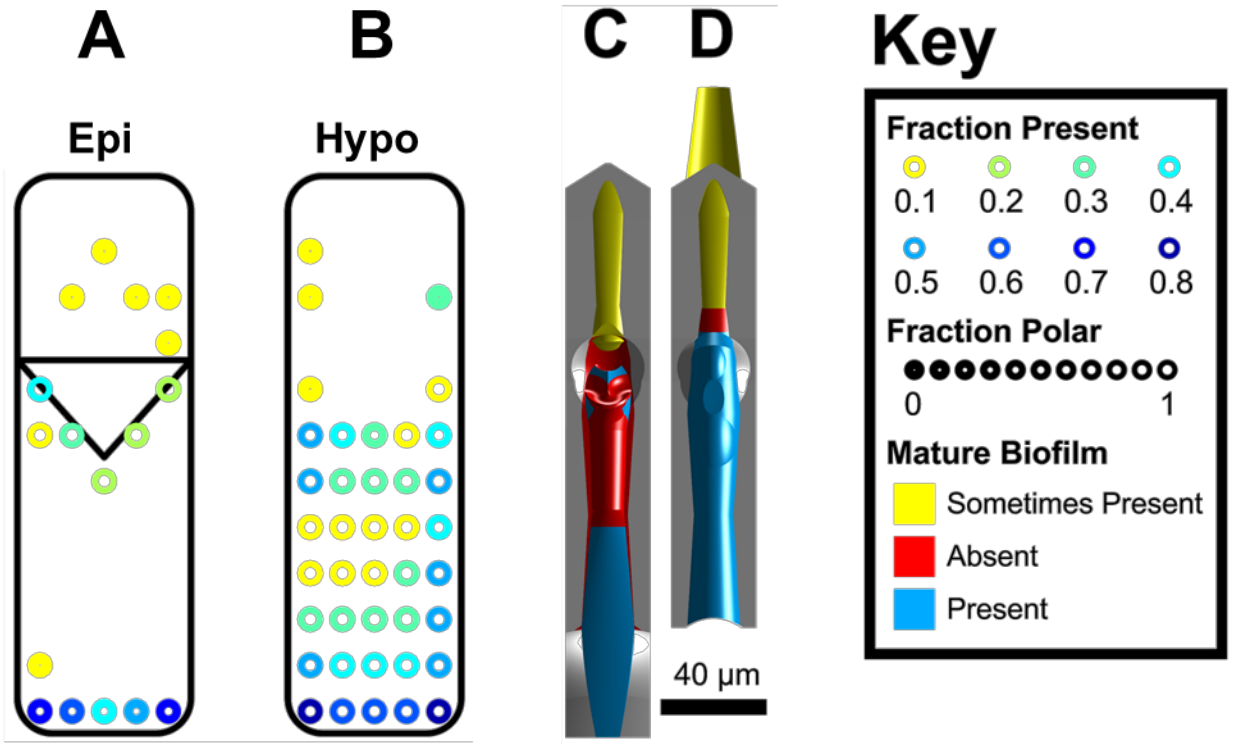

Figure 4.4: Colonization patterns of X. fastidiosa in the precibarium of blue-green sharpshooters after two-day incubation periods (A & B) and after at least 11 days of incubation (C & D). A&B) Subfigures A and B summarize the findings of Almeida and Purcell by combining their 12 published diagrams of epipharynx (A) and hypopharynx (B) colonization[3]. The images are not drawn to scale of the precibarium, and the triangle represents the precibarial valve. The color of the circles represents the fraction of published observations of a given location that indicated cells were attached. The amount of circle fill represents the fraction of attached cells that were polarly attached. C&D) Subfigures C and D summarize the location of developed biofilms in the precibarium (at least 11 days of incubation), as gathered from published descriptions and published microscope images[3,8,9,22]. The locations are mapped onto 3D models of the epipharynx (C) and hypopharynx (D). Blue represents colonized segments, red represents uncolonized segments, and yellow represents segments that are sometimes colonized.

Precibarial colonization patterns support a mechanism of flow-driven bacterial detachment during feeding. Segments of the precibarium with higher predicted drag forces (Fig. 4.3) tended to have lower bacterial colonization frequencies after a two-day

incubation period (Fig. 4.4, A & B). Segments with lower drag forces tended to have higher colonization frequencies. Colonization patterns in the proximal two thirds of Fig. 4.4B resemble the saddle-like drag forces in Fig. 4.4D, with less colonization in the middle of the saddle. The segments of the precibarium that appear to be distal to the precibarial valve, with drag forces greater than $10^{3.0}$ pN during egestion (Fig. 4.3), were not often colonized (Fig. 4.4). The proximal-most region of the hypopharynx, with some of the lowest drag forces on the hypopharynx, had the highest likelihood of observing attached bacteria. Similarly, the proximal-most region of the epipharynx, with some of the lowest drag forces, experienced a high rate of colonization.

Two of the other regions with low predicted drag forces were likely colonized after a two-day incubation period: the valve shadow and the precibarial pit/ring. Fig. 4.4A indicates bacterial colonization near the edge of the valve after a two-day incubation period, which is reminiscent of previously published images of developed biofilms that appear to extend under the valve[3,9]. In addition, bacteria were imaged at the entrance of the precibarial pit after a two-day incubation period[3]. Cells were also often found in the precibarial pit, though it is not clear whether this included specimens with two-day incubation periods. Therefore, three of the four regions of the precibarium with low predicted drag forces during egestion were likely colonized after a two-day incubation period.

The fourth region, the basin crease, remained notably uncolonized when developed biofilms (at least 11 days of incubation) were observed in the precibarium (Fig. 4.4C). The lack of colonization in this region contradicts a simple flow-driven detachment

interpretation and may be due to water hammer. Water hammer is a phenomenon observed in water pipes where a pressure wave travels through the water after a valve is abruptly closed[23].

Cervantes and Backus report peaks in electropenetrography (EPG) recordings of insect feeding that are thought to represent closing of the precibarial valve before swallowing[10]. Their results indicate that this closing may occur while xylem sap is still flowing into the cibarium during ingestion. In this case, quick closing of the valve likely causes water hammer. Simplistic calculations indicate that instantaneous closure of the precibarial valve during ingestion could increase the pressure distal to the valve by four atmospheres. The resulting pressure force may kick the epipharyngeal basin proximally, creating a water current in the basin crease and basin proximal slope, which could detach cells. This hypothesis is supported by the observed colonization of the basin triangle, with a lack of colonization between the basin triangle and the epipharyngeal fold[3]. This suggests that the two indicated boundaries approach each other during water hammer, smashing or dislodging cells at the edges of the basin triangle.

Other segments of the precibarium that remained uncolonized include the distal portion and upper edge of the epipharyngeal trough (Fig. 4.4C). These are segments with predicted drag forces that are mostly greater than $10^{3.0}$ pN during egestion (Fig. 4.3). Additionally, the distal epipharyngeal basin and the valve contact patch remained uncolonized (Fig. 4.4), but these may be due to closing of the precibarial valve[3]. Other segments distal to the precibarial valve were only sometimes colonized after at least 11

days of incubation (Fig. 4.4). These segments contain predicted drag forces greater than $10^{3.0}$ pN during egestion (Fig. 4.3).

Notably, there are two main segments in Fig. 4.4 with higher frequencies of laterally attached bacteria after two-day incubation periods. These appear to be distal to the precibarial valve and in a proximal segment of the epipharyngeal trough. These two regions have predicted drag forces that differ by a couple orders of magnitude from each other. Thus, the observed lateral attachment may not be due to the local flow environments.

4.3 Discussion

The results presented herein indicate that fluid dynamics likely play a major role in *X. fastidiosa* inoculation from the blue-green sharpshooter precibarium. Novel insect simulations predicted fine spatial details of fluid dynamics that mirror colonization patterns, with egestion drag forces that are much higher than those required to detach bacteria. In the proceeding discussion, xylem simulation results are used to gain mechanistic insights into *X. fastidiosa* virulence and acquisition. Mechanistic insights from the xylem and insect simulations are summarized in a model that is supported by published virulence and transmission studies on *X. fastidiosa* mutants[7,9,24,25].

Xylem simulations support the hypothesis that grapevine cultivars with wider xylem vessels are more susceptible to Pierce's disease than cultivars with narrower vessels[26]. Drag forces in undisturbed xylem are predicted to be higher in wider vessels (Fig. 4.2, *Undisturbed*). Thus, increased bacterial detachment from biofilms and decreased attachment of planktonic bacteria likely contribute to increased *X. fastidiosa* mobility in these vessels. Increased mobility of *X. fastidiosa* in grapevine xylem is linked with quicker development of Pierce's disease[24,25,27].

Xylem simulations also suggest that insects acquire more bacteria when feeding on narrower vessels. Drag forces in xylem vessels are predicted to be highest during insect egestion (Fig. 4.2). Particularly, vessels under 140 μm in diameter may be the main location of bacterial detachment during insect feeding, with an inverse relationship between detachment and vessel diameter. Thus, there is expected to be an inverse relationship between insect acquisition of the bacteria and vessel diameter.

This speculation is supported by observations that glassy-winged sharpshooters have higher bacterial acquisition efficiencies from water-stressed grapevines[28]. The opposite result might be predicted because lower insect populations and lower feeding rates are expected under water stress conditions[29]. However, water-stressed grapevines have a lower percentage of large xylem vessels than well-irrigated grapevines[18]. This could force sharpshooters to feed on smaller vessels, even though they may prefer large vessels[30], leading to higher rates of bacterial acquisition.

Bacteria acquisition is likely driven by drag forces during egestion, rather than ingestion. Predicted drag forces in xylem vessels are 14 times higher during egestion (Fig. 4.2). Notably, egestion is part of X wave feeding, a behavior that is interpreted as testing of xylem vessels before sustained ingestion. X wave feeding includes both egestion and ingestion in each tested vessel. It has been implicated in *X. fastidiosa* inoculation, though it has not yet been implicated in acquisition. Instead, most acquisition was previously speculated to occur during sustained ingestion. Egestion drag forces likely cause more xylem-dwelling bacteria to detach, enabling them to enter the functional foregut as planktonic bacteria and/or floating bacterial aggregates. Higher concentrations of floating bacteria cause more attachment in the precibarium, since bacteria deposition rates can be approximated as being proportional to floating bacteria concentration[31]. The timing of bacterial acquisition is discussed further in Appendix D.

In summary, our results support a model of how fluid dynamics affect *X. fastidiosa* virulence, acquisition, and inoculation (Fig. 4.5). Xylem flow, driven by a water potential gradient[32], causes detachment and spread of *X. fastidiosa* in undisturbed xylem (Fig. 4.2).

When BGSS feed on grapevine xylem, high egestion flowrates cause xylem-dwelling bacteria to detach (Fig. 4.2). Detached bacteria are carried into the insect functional foregut during ingestion, where they attach and form biofilms. During egestion, high flowrates detach cells from the functional foregut (Fig. 4.3 & 4.4) and carry them into plant xylem vessels.

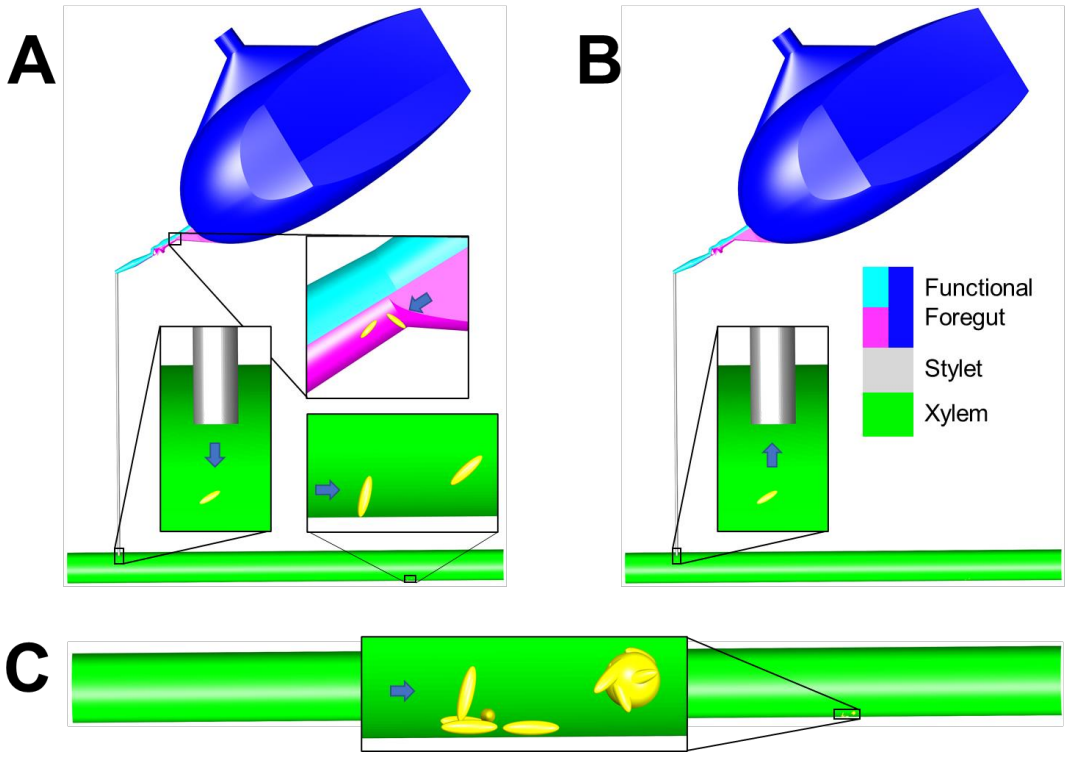

Figure 4.5:Inferred model of detachment-based transmission and virulence. The model describes the effects of xylem sap flow on surface-attached bacteria during egestion (A), ingestion (B), and in undisturbed xylem (C). A) Individually surface-attached bacteria and aggregates are detached from both xylem walls and precibarium walls during egestion. B) *X. fastidiosa* cells are acquired during ingestion. C) *X. fastidiosa* cells detach as aggregates in undisturbed xylem (in the absence of insect feeding).

Our model is supported by virulence and transmission studies on *X. fastidiosa* mutants[7,9,24,25]. Hyperattaching *rpfC* mutants are less mobile in grapevine xylem than wild

type *X. fastidiosa*, suggesting they are not easily detached from xylem biofilms to spread in the vasculature[24]. *rpfC* mutants are retained in BGSS heads less frequently than wild type (not significantly less) [24], suggesting *rpfC* mutants do not detach from xylem vessels as readily as wild type during X wave feeding, especially since they would intuitively adhere more strongly in the functional foregut than wild type. Meanwhile, hypoattaching *rpfF* mutants are more mobile in grapevines, present in a slightly high percentage of BGSS heads during feeding on infected grapevine, and poorly retained 7 days later[9,24]. Similarly, hypoattaching *gumD*, *gumH*, and *wzy* mutants may be poorly acquired/retained in BGSS[7,25]. These observations are consistent with flow-driven attachment and/or detachment hypotheses for both xylem vessels and the functional foregut.

Notably, hypoattaching *gumD* and *gumH* mutants are less mobile in grapevine, which may be interpreted as counterexamples to the model. However, grapevine infection rates and bacterial population sizes suggest that grapevines exhibit strong defense responses against these mutants[25]. The altered cell surface composition of these mutants may lead to quicker grapevine sensing of pathogen associated molecular patterns and corresponding quicker tyloses deployment[33], which is consistent with reduced pathogen mobility. Thus, virulence and transmission studies on *X. fastidiosa* mutants that have altered adhesion properties support our model.

Our model is also supported by the results of Purcell and Finlay (1979)[34], which are consistent with inoculation that is dominated by detachment rather than a flying syringe mechanism. PD transmission via BGSS increased with longer inoculation access periods (IAP). If inoculation of planktonic bacteria from the fluid held in the functional foregut

were a large contributor to transmission, the fitted trend of transmission versus IAP would have a large y-intercept. However, the y-intercept transmission rate (2%) is less than one tenth of the predicted transmission rate (>20%) for a 1-hour IAP. In addition, PD transmission via BGSS that were allowed different acquisition access periods (AAP) increased with increasing AAP. If transmission occurred solely due to a flying syringe mechanism, the transmission would not be affected by AAP.

We hypothesize flow-driven detachment is the main cause of BGSS *X. fastidiosa* inoculation in grapevines. Besides the flying syringe hypothesis, it has also been hypothesized that insect saliva plays a biochemical role in detaching bacteria from the functional foregut by degrading biofilm EPS[30,35]. However, our fluid dynamic simulations predict drag forces in the precibarium much higher than those required to detach *X. fastidiosa* from glass in the absence of insect saliva (Fig. 4.3)[19]. Thus, biochemical degradation is not expected to be necessary for *X. fastidiosa* transmission.

While our fluid dynamic simulations are useful for understanding *X. fastidiosa* virulence and transmission, they have limitations that could be improved in future studies. For example, xylem vessels were simulated as isolated cylindrical pipes. Xylem simulations did not account for the surface topography of vessels, the migration of fluid from adjacent vessels through pits, the T-junction nature of insect-xylem interactions, the pressure gradient heterogeneity in undisturbed xylem[16], or the interaction between insect-caused and plant-caused fluid dynamics in the xylem. The interaction between insect-driven flow and water potential gradient-driven flow was instead accounted for by modifying Figure 4.2. During ingestion (Fig. 2, *Ingestion*), calculated drag forces in xylem

vessels larger than 70 μm are similar to or lower than those for undisturbed xylem (Fig. 4.2, *Undisturbed*). During egestion (Fig. 4.2, *Egestion*), the same is true for xylem vessels larger than 130 μm. In these cases, simulation results for insect-driven flow are not included in Figure 4.2.

A second limitation of our analysis is that the insect simulations in Figure 4.3 relied on published EPG waveforms to make estimates for the durations of ingestion and swallowing during individual sustained ingestion (C2) episodes (see Methods). This resulted in estimates being less precise than they could have been if they used targeted EPG data, with the average durations of ingestion and swallowing during individual C2 episodes, as well as their standard deviations. A third limitation of our analysis is that the simulated flowrate during egestion was assumed to be equal to the average flowrate of swallowing, calculated by dividing the volume of the cibarium by the duration of swallowing. Thus, egestion flowrates were likely underestimated. This is because cibarial diaphragm elasticity is thought to work against the esophageal valve to accomplish swallowing, while cibarial diaphragm elasticity is thought to work in the same direction as xylem tension to accomplish egestion[3,36]. If the egestion flowrate used in fluid dynamic simulations were higher, the 140 μm cutoff in Figure 4.2 for ignoring egestion-driven flow would be higher and the regions in Figure 3C, 3D with drag forces less than $10^{1.2}$ pN would be smaller. Fittingly, Figures 4.2 and 4.3 are presented in ways that encourage order-of-magnitude analyses so that readers do not overinterpret the precision of our results.

The novel fluid dynamic simulations presented herein provide valuable insights into the virulence and transmission of *X. fastidiosa*. Results support a model for how fluid

dynamics affect *X. fastidiosa* virulence, acquisition, and transmission. The model sheds light on how microbial community development in situ is affected by environmental stresses and plant traits. An interdisciplinary approach is used to bring a quantitative understanding of interactions between phytobiome components[37].

Insect simulations similar to those presented herein could be used in future studies of physical transmission mechanisms for various insect-pathogen-plant scenarios. The 3D models in our insect simulations could be reapplied to simulate BGSS feeding on different host plants. In addition, 3D models and simulations could be created for other vectors of *X. fastidiosa*, such as the meadow spittlebug (*Philaenus spumarius*) and the glassy-winged sharpshooter (*Homalodisca vitripennis*). These vectors are implicated in serious crop diseases caused by *X. fastidiosa*[29]. Furthermore, insect simulations could be more broadly applicable for understanding physical transmission mechanisms of other cuticula-borne pathogens.

4.4 Methods

Fluid dynamic simulation results and colonization patterns were plotted using MATLAB® (Mathworks Inc, Natick, MA).

4.4.1 Xylem Simulations

Fluid dynamics in xylem vessels were simulated in COMSOL Multiphysics® (COMSOL, Inc., Stockholm, Sweden). 3D cylinders were used, with inlet and outlet specified based on the type of simulation. In the *Undisturbed* simulation, the boundary conditions were specified based on a water potential gradient of 0.03 MPa/m, which was

previously reported for both well-irrigated and water-stressed grapevines. The water potential gradient was modeled as a pressure potential gradient. In the *Ingestion* and *Egestion* simulations, flowrates were specified by dividing the calculated volume of the insect cibarium by the duration of filling and emptying of the cibarium during ingestion and swallowing. The volume was calculated from our 3D model of the cibarium and the duration was calculated based on reported EPG waveforms. Mesh refinement studies were completed for different vessel sizes and boundary conditions. More details on xylem simulations are in Appendix D.

4.4.2 Insect Simulations

Fluid dynamics in the precibarium were simulated in COMSOL Multiphysics® using our 3D model of the precibarium and cibarium[21]. The cibarial diaphragm was used as the outlet and inlet during ingestion and egestion, respectively. The flowrates calculated for *Ingestion* and *Egestion* xylem simulations were normalized based on the diaphragm surface area to calculate boundary velocities. These velocities were specified as perpendicular to the diaphragm to mimic the effects of diaphragm extension and relaxation. Simulation results and the 3D model meshes were exported and used in MATLAB® to calculate the drag forces acting on bacteria. Mesh refinement studies were completed. The temperature of water in insect simulations was specified based on heat transfer simulations. The Newtonian slip length of water over the insect cuticle was accounted for, based on the slip length of a similar surface. More details on insect simulations are in Appendix D.

4.5 References

1 Tumber, K., Alston, J. & Fuller, K. Pierce's disease costs California $104 million per year. *California Agriculture* **68**, 20-29 (2014).

2 Purcell, A. & Saunders, S. Glassy-Winged Sharpshooters Expected to Increase Plant Disease. *California Agriculture* **53**, 26-27 (1999).

3 Almeida, R. P. & Purcell, A. H. Patterns of Xylella fastidiosa colonization on the precibarium of sharpshooter vectors relative to transmission to plants. *Annals of the Entomological Society of America* **99**, 884-890 (2006).

4 Backus, E. A. & Morgan, D. J. Spatiotemporal Colonization of *Xylella fastidiosa* in its Vector Supports the role of Egestion in the Inoculation Mechanism of Foregut-Borne Plant Pathogens. *Phytopathology* **101**, 912-922 (2011).

5 Roper, M. & Lindow, S. E. Xylella fastidiosa: Insights into the lifestyle of a xylem-limited bacterium. *American Phytopathological Society, St. Paul, MN* (2015).

6 Purcell, A. H., Finlay, A. H. & McLean, D. L. Pierce's disease bacterium: Mechanism of transmission by leafhopper vectors. *Science* **206**, 839-841 (1979).

7 Rapicavoli, J. N. *et al.* O-antigen Modulates Insect Vector Acquisition of the Bacterial Plant Pathogen, Xylella fastidiosa. *Applied and environmental microbiology*, AEM. 02383-02315 (2015).

8 Purcell, A. H., Almeida, R. P., Backus, E., Jennifer, H. & Hill, B. Characterization and Studies on the Fundamental Mechanisms of Xylella Fastidiosa Transmission to Grapevines by The Glassy-Winged Sharpshooter 115 - 117 (Web, 2003).

9 Newman, K. L., Almeida, R. P., Purcell, A. H. & Lindow, S. E. Cell-Cell Signaling Controls *Xylella fastidiosa* Interactions with Both Insects and Plants. *Proceedings of the National Academy of Sciences* **101**, 1737-1742 (2004).

10 Cervantes, F. A. & Backus, E. A. EPG waveform library for Graphocephala atropunctata (Hemiptera: Cicadellidae): effect of adhesive, input resistor, and voltage levels on waveform appearance and stylet probing behaviors. *Journal of insect physiology* **109**, 21-40 (2018).

11 López, D., Vlamakis, H. & Kolter, R. Biofilms. *Cold Spring Harbor perspectives in biology* **2**, a000398 (2010).

12 Backus, E. A., Shugart, H. J., Rogers, E. E., Morgan, J. K. & Shatters, R. Direct evidence of egestion and salivation of Xylella fastidiosa suggests sharpshooters can be “flying syringes”. *Phytopathology* **105**, 608-620 (2015).

13 Dugravot, S., Backus, E. A., Reardon, B. J. & Miller, T. A. Correlations of cibarial muscle activities of Homalodisca spp. sharpshooters (Hemiptera: Cicadellidae) with EPG ingestion waveform and excretion. *Journal of insect physiology* **54**, 1467-1478 (2008).

14 Ranieri, E. *et al.* Fluid Dynamics in the Functional Foregut of Xylem-Sap Feeding Insects: A Comparative Study of Two *Xylella fastidiosa* Vectors. *Journal of Insect Physiology* **120**, 103995 (2020).

15 White, D., Backus, E. A., Marcus, I. M., Walker, S. L. & Roper, M. C. Functional foregut anatomy of the blue–green sharpshooter illustrated using a 3D model. *Scientific reports* **11**, 1-12 (2021).

16 Bouda, M., Windt, C. W., McElrone, A. J. & Brodersen, C. R. In vivo pressure gradient heterogeneity increases flow contribution of small diameter vessels in grapevine. *Nature communications* **10**, 1-10 (2019).

17 Alexis, M. E., Basile, K. B. & Clément, K. Dynamics of Water Flow in the Atmosphere-Aerial Roots Continuum. *Open Journal of Fluid Dynamics* **8**, 404-415 (2018).

18 Lovisolo, C. & Schubert, A. Effects of Water Stress on Vessel Size and Xylem Hydraulic Conductivity in *Vitis vinifera* L. *Journal of Experimental Botany* **49**, 693-700 (1998).

19 De La Fuente, L. *et al.* Assessing adhesion forces of type I and type IV pili of Xylella fastidiosa bacteria by use of a microfluidic flow chamber. *Appl. Environ. Microbiol.* **73**, 2690-2696 (2007).

20 Monteiro, M. P. *et al.* Stiffness signatures along early stages of Xylella fastidiosa biofilm formation. *Colloids and Surfaces B: Biointerfaces* **159**, 174-182 (2017).

21 White, D., Roper, M., & Backus, E. 3D Illustrated Anatomy of Sharpshooter Insect Functional Foregut. (2020 (In Press)).

22 Purcell, A. H., Almeida, R. P., Lindow, S. & Newman, K. Role of bacterial attachment in transmission of Xylella fastidiosa by the glassy-winged sharpshooter, and other factors affecting transmission efficiency. in *Symposium Proceedings.*

23 Ghidaoui, M. S., Zhao, M., McInnis, D. A. & Axworthy, D. H. A review of water hammer theory and practice. *Appl. Mech. Rev.* **58**, 49-76 (2005).

24 Chatterjee, S., Wistrom, C. & Lindow, S. E. A cell–cell signaling sensor is required for virulence and insect transmission of Xylella fastidiosa. *Proceedings of the National Academy of Sciences* **105**, 2670-2675 (2008).

25 Killiny, N., Martinez, R. H., Dumenyo, C. K., Cooksey, D. & Almeida, R. The exopolysaccharide of Xylella fastidiosa is essential for biofilm formation, plant virulence, and vector transmission. *Molecular plant-microbe interactions* **26**, 1044-1053 (2013).

26 Deyett, E. *et al.* Assessment of Pierce's disease susceptibility in *Vitis vinifera* cultivars with different pedigrees. *Plant Pathology* **68**, 1079-1087 (2019).

27 Lindow, S. *et al.* Production of *Xylella fastidiosa* Diffusible Signal Factor in Transgenic Grape Causes Pathogen Confusion and Reduction in Severity of Pierce's Disease. *Molecular Plant-Microbe Interactions* **27**, 244-254 (2014).

28 Del Cid, C., Krugner, R., Zeilinger, A. R., Daugherty, M. P. & Almeida, R. P. Plant Water Stress and Vector Feeding Preference Mediate Transmission Efficiency of a Plant Pathogen. *Environmental Entomology* **47**, 1471-1478 (2018).

29 Krugner, R., Sisterson, M. S., Backus, E. A., Burbank, L. P. & Redak, R. A. Sharpshooters: a review of what moves Xylella fastidiosa. *Austral Entomology* **58**, 248-267 (2019).

30 Backus, E. A., Holmes, W. J., Schreiber, F., Reardon, B. J. & Walker, G. P. Sharpshooter X wave: correlation of an electrical penetration graph waveform with xylem penetration supports a hypothesized mechanism for Xylella fastidiosa inoculation. *Annals of the Entomological Society of America* **102**, 847-867 (2009).

31 Carniello, V., Peterson, B. W., van der Mei, H. C. & Busscher, H. J. Physico-chemistry from initial bacterial adhesion to surface-programmed biofilm growth. *Advances in colloid and interface science* (2018).

32 Stroock, A. D., Pagay, V. V., Zwieniecki, M. A. & Michele Holbrook, N. The Physicochemical Hydrodynamics of Vascular Plants. *Annual Review of Fluid Mechanics* **46**, 615-642 (2014).

33 Rapicavoli, J. N. *et al.* Lipopolysaccharide O-antigen delays plant innate immune recognition of Xylella fastidiosa. *Nature Communications* **9**, 390, doi:10.1038/s41467-018-02861-5 (2018).

34 Purcell, A. H. & Finlay, A. Evidence for Noncirculative Transmission of Pierce's Disease Bacterium by Sharpshooter Leafhoppers. *Phytopathology* **69**, 393-395 (1979).

35 Backus, E. A. *et al.* Salivary enzymes are injected into xylem by the glassy-winged sharpshooter, a vector of Xylella fastidiosa. *Journal of insect physiology* **58**, 949-959 (2012).

36 Snodgrass, R. in *Principles of Insect Morphology* (ed AF Shull) 328-343 (McGraw-Hill Book Company, Inc., 1935).

37 Phytobiomes: A Roadmap for Research and Translation. (2016). <phytobiomes.org/roadmap>.

Chapter 5

Summary & Conclusions

The overarching goal of this doctoral work was to investigate how fluid drag forces and surface interaction forces affect the aqueous transport of pathogenic bacteria in agricultural systems. The transport of *E. coli* O157:H7 in agricultural soils in the presence of the nanoparticles TiO_2 and CuO was investigated using saturated sand column experiments (Chapter 2). Column experiment results were interpreted using DLVO predictions of surface interactions and parallel plate flow cell experiment results. The transport of *Xylella fastidiosa* in an insect-plant system was studied by simulating the fluid drag forces acting on surface-adhered bacteria (Chapter 4). Spatial drag force predictions were compared with locations where bacteria were observed to be surface-adhered in insects. This comparison was enhanced by a uniform terminology of insect anatomy (Chapter 3, Appendix B) and published measurements of the drag fluid forces required to detach surface-adhered *X. fastidiosa* cells (Chapter 4). The fate and transport of many bacteria species in various systems could be studied using the computer code developed in Appendix E. This code lays the groundwork for simulating how fluid drag forces and DLVO forces interact to affect bacterial surface deposition.

Chapter 2 results indicate that the presence of TiO_2 or CuO nanoparticles at the tested conditions each affect *E. coli* O157:H7 transport in at least one of the model systems. Mechanisms of altered transport in the presence of nanoparticles cannot be completely explained by fluid flow conditions and DLVO predictions. The increase of *E. coli* attachment in the presence of CuO in parallel plate experiments was not predicted by DLVO theory and may have been a biological response to stress. The increase of *E. coli* release in the presence of TiO_2 during the simulated rain events of column experiments

was supported by DLVO predictions. However, the overall lack of *E. coli* release in the presence of TiO_2 was not supported by classic DLVO theory. Instead, additional factors such as particle charge heterogeneity and hydrophobicity may have played important roles. Thus, more advanced models are needed for predicting *E. coli* transport in these experimental scenarios. Specifically, it could be valuable to model the potential for increased *E. coli* spread in agricultural soils in the presence of TiO_2 nanoparticles. This could have policy implications for regulating how nano-containing products can be applied, as well as regulating the required distances between at-risk water resources and sources of pathogenic *E. coli.*

In Chapter 3, a uniform terminology of anatomy related to sharpshooter insect functional foreguts is described. This uniform terminology enhances the analysis in Chapter 4 by making anatomical terminology more accessible to multidisciplinary scientists. It mitigates inconsistencies, consolidates synonyms, and increases the spatial resolution with which anatomy can be described. These properties of the uniform terminology reduce the barrier to entry for scientists seeking to research *X. fastidiosa* transmission.

Chapter 4 clarifies how fluid dynamics likely play a major role in the spread of *X. fastidiosa* between plants, and possibly within plants. Predictions are made for fluid drag forces acting on individually surface-attached cells in the blue-green sharpshooter functional foregut and grapevine xylem. Spatial predictions of drag forces in the insect are compared with bacteria surface colonization patterns in the precibarium, as well as the drag forces required to detach surface-adhered *X. fastidiosa* cells in laboratory experiments.

Results are used to support a model for how fluid dynamics affect detachment steps in *X. fastidiosa* spread between plants and within plants (Figure 4.5). The model predicts that fluid drag forces drive *X. fastidiosa* acquisition by insects, inoculation into plants, and spread in undisturbed xylem vessels. The model also predicts that drag forces drive more *X. fastidiosa* spread in wider xylem vessels than in narrower vessels.

The model in Chapter 4 supports potential targets for combating plant diseases caused by *X. fastidiosa*, two of which are novel (Figure 5.1). These unverified targets center around optimizing xylem vessel diameters and altering xylem sap properties. For example, the acquisition of *X. fastidiosa* by vectors may be reduced if the plants available for bacteria acquisition contain high proportions of wide xylem vessels, ideally greater than or equal to 140 μm in the case of blue-green sharpshooters feeding on grapevine (Figure 4.2). However, wider grapevine vessels may promote higher *X. fastidiosa* mobility in undisturbed xylem and corresponding quicker development of Pierce's disease, as well as increased risk of embolisms. Thus, optimizing vessel diameter distribution may be effective for combatting Pierce's disease. Future investigations of this potential disease prevention target will require studies that use insect-based inoculation rather than needle-based inoculation. In these investigations, xylem vessel diameter can be affected through grapevine breeding programs or screening for alternate hosts to plant around vineyards based on xylem vessel diameter distribution.

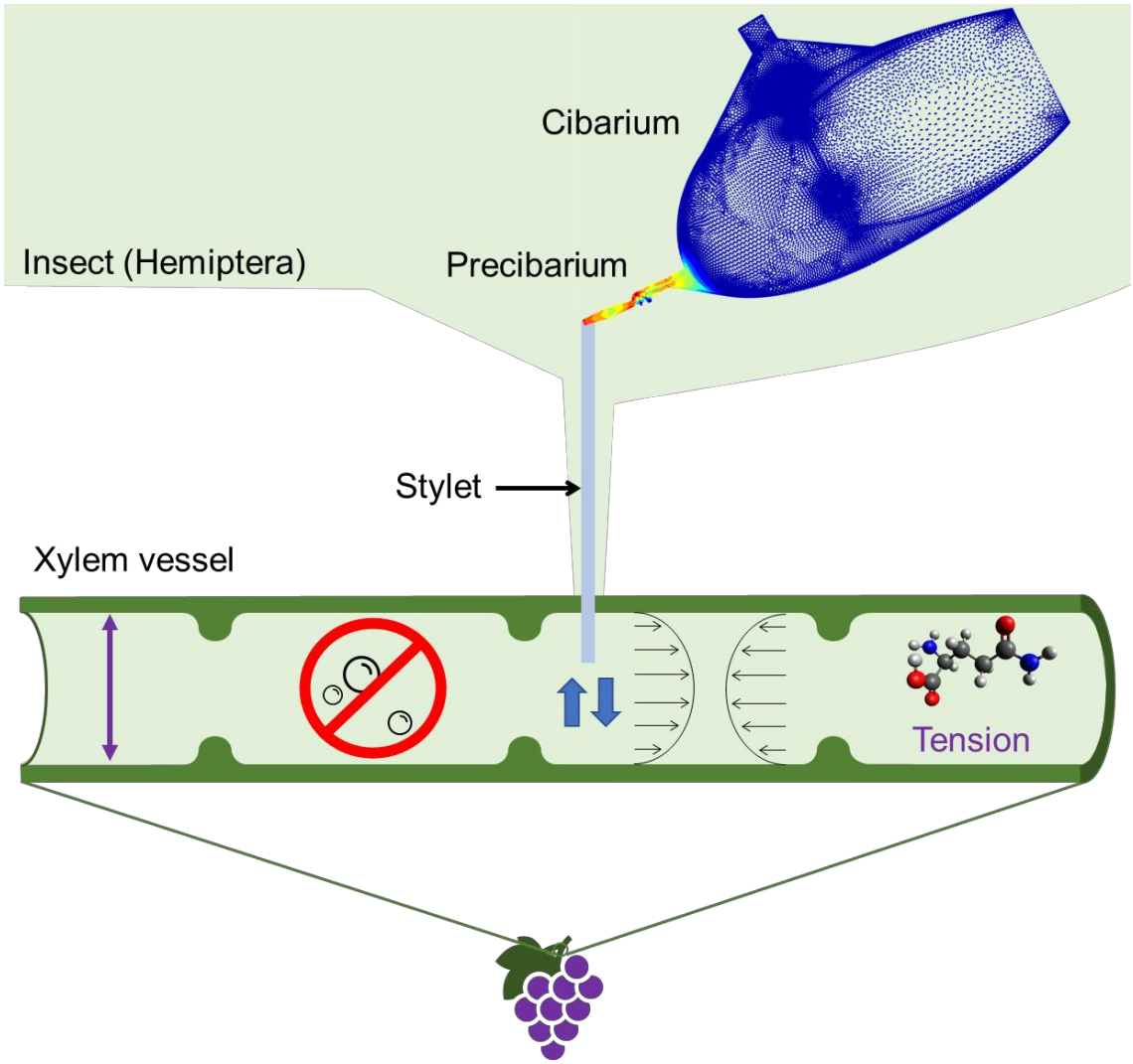

Figure 5.1: Summary of Chapter 4 simulations and potential disease prevention targets. A model blue-green sharpshooter feeds on grapevine xylem sap. Fluid dynamics during ingestion and egestion were simulated for both the functional foregut and xylem vessels of variable diameters. Results support flow driven mechanisms for vector acquisition and inoculation of *X. fastidiosa*. This mechanistic understanding emphasizes three potential targets for preventing diseases caused by *X. fastidiosa*. 1) Optimize xylem vessel diameter (purple arrows). 2) Avoid embolisms (air bubbles). 3) Reduce vector feeding behaviors associated with disease transmission, specifically the number of xylem vessels tested and the number of egestion-containing episodes. Vector feeding behavior may be influenced by xylem sap glutamine content (molecular drawing) and xylem tension[2,3].

Additionally, since it is inferred that physical forces play a major role in the spread of *X. fastidiosa*, there is increased incentive to avoid embolisms (air bubbles) in grapevines. Air bubble passage can exert around 10^5 pN of perpendicularly oriented detachment force on bacteria[4], which is larger than the predicted fluid drag forces in grapevine xylem vessels and most of the precibarium (Figure 4.2, Figure 4.3). Embolisms could cause *X. fastidiosa* to detach from xylem vessel walls, increase the bacteria's mobility in the plant, and lead to quicker systemic colonization of the plant. If air bubbles are ingested by the insect, they could lead to increased bacterial detachment from the functional foregut and increased inoculation.

Other potential disease prevention targets are related to insect feeding behavior. Relevant feeding parameters could be the number of xylem vessels a vector tests before accepting one and the number of egestion-containing episodes within vessels before acceptance. These feeding parameters can be quantified in future EPG studies and efforts to reduce them could lead to reduced transmission. Minimizing the number of vessels that a vector tests could lead to fewer inoculated xylem vessels and a lower probability of acquisition. Minimizing the number of egestion-containing events could lead to less *X. fastidiosa* cells acquired and inoculated. Sharpshooter feeding may be influenced by differences in xylem vessel diameter, xylem sap chemistry (particularly glutamine content), and xylem tension[2,3].

Overall, the model in Chapter 4 supports three potential targets for fighting plant diseases caused by *X. fastidiosa*, two of which are novel (Figure 5.1). 1) Optimize xylem vessel diameter. Chapter 4 results inspire the first acknowledgement that thinner xylem

vessels may lead to more *X. fastidiosa* acquisition by vectors, while supporting the previously reported hypothesis that grapevine cultivars with wider xylem vessels are more susceptible to Pierce's disease[1]. 2) Avoid embolisms. Chapter 4 results emphasize the importance of preventing embolisms in xylem vessels. Embolisms likely cause larger bacteria detachment forces than fluid dynamics in xylem vessels and most of the functional foregut. Larger detachment forces could lead to more acquisition and inoculation. 3) Reduce vector feeding behaviors associated with disease transmission, specifically the number of xylem vessels tested and the number of egestion-containing episodes. Chapter 4 results provide novel insight into the importance of egestion for *X. fastidiosa* acquisition and support egestion's putative role in inoculation. Acquisition was previously presumed to occur mainly during sustained ingestion, which occurs after egestion-containing X wave feeding. Since X wave feeding is part of xylem vessel testing, there is potential for both acquisition and inoculation in each tested xylem vessel. This increases the motivation for a disease prevention target which has not been discussed in published articles: reducing the number of tested vessels. Likewise, Chapter 4 results provide added significance for the intuitive target of reducing the number of egestion-containing episodes during feeding, due to its newfound relevance for bacteria acquisition. Vector feeding behavior may be influenced by xylem sap glutamine content and xylem tension[2,3].

As demonstrated in the preceding paragraphs, understanding mechanisms of pathogenic bacteria transport can lead to the proposal of new targets for disease prevention. In this study, potential *X. fastidiosa* disease prevention targets, including two novel targets, have been emphasized: optimizing xylem vessel diameter, avoiding embolisms, and

affecting insect feeding behaviors. Future research could examine how these targets affect *X. fastidiosa* spread, as well as how the targets can be controlled.

This potential for practical application of this dissertation research demonstrates how fundamental studies of bacteria transport mechanisms can be beneficial. Bacteria transport properties affect the spread of the human pathogen *E. coli* O157:H7 and the plant pathogen *X. fastidiosa.* In this dissertation, the effects of fluid drag forces and surface interactions on bacteria deposition and detachment were studied. A combination of experimental and computational tools was used to examine thermodynamic, kinetic, and transport properties of agricultural systems. The tools that were developed can be used to study bacteria transport in diverse systems for the protection of human health, environmental health, and economic outcomes.

5.1 References

1 Deyett, E. *et al.* Assessment of Pierce's disease susceptibility in *Vitis vinifera* cultivars with different pedigrees. *Plant Pathology* **68**, 1079-1087 (2019).

2 Andersen, P. C., Brodbeck, B. V., Mizell III, R. F. & Oden, S. Abundance and feeding of Homalodisca coagulata (Hemiptera: Auchenorrhyncha: Cicadellidae) on Vitis genotypes in north Florida. *Environmental entomology* **34**, 466-478 (2005).

3 Andersen, P. C., Brodbeck, B. V. & Mizell III, R. F. Feeding by the leafhopper, *Homalodisca coagulata*, in relation to xylem fluid chemistry and tension. *Journal of Insect Physiology* **38**, 611-622 (1992).

4 Boks, N. P., Norde, W., van der Mei, H. C. & Busscher, H. J. Forces involved in bacterial adhesion to hydrophilic and hydrophobic surfaces. *Microbiology* **154**, 3122-3133 (2008).

Appendices

Appendix A: Supplemental Information for Chapter 2

Appendix B: Uniform Terminology for Chapter 3

Appendix C: Supplemental Information for Chapter 3

Appendix D: Supplemental Information for Chapter 4

Appendix E: Overview of Approach to Particle Tracking Simulation Incorporating Surface Interactions

Appendix A: Supplemental Information for Chapter 2

A.1 Sand Preparation and Column Operation

Sand was prepared as described previously, except that baked sand was not stored under vacuum between baking and rehydration[1]. Briefly, quartz (IOTA) was sieved and the fraction between 250 and 300 μm sieves was retained and soaked in 12 M HCl for at least 24 hours. Acid-soaked sand was washed with DI H2O and baked in an oven at 800 °C for at least 8 hours. The baked sand was rehydrated for at least one hour by boiling in DI water and it was stored in DI water until used when wet packing the column. The column had a length of 5 cm, inner diameter of 1.5 cm, and porosity of 0.45 +/- 0.01.

In preparation for column experiments, at least 40 mL (10 PV) of DI H2O were flowed through the column, followed by at least 40 mL (10 PV) of 10 mM KCl. Once UV-VIS measurements began, 30 mL of the experimental solution (7.5 PV), 30 mL of the KCl electrolyte (7.5 PV), and 20 mL of DI H2O (5 PV) were flowed through the column. Once each experiment was completed, the column was removed from the flow system and the experimental solution was flowed through the tubing to measure C_0 for the breakthrough curve using the same UV-VIS detector.

The detector scanned at 366 and 600 nm so that the composition of the effluent could be probed. Previous research has used these two wavelengths to study the

photocatalytic activity of TiO_2 and measure the optical density of bacteria, respectively[2,3]. During measurements of experimental C_0 values, suspensions containing *E. coli* O157:H7 alone or in the presence of either particle displayed a ratio of absorbance at 366 nm vs. 600nm that was greater than one. Meanwhile, both ENMs in the absence of bacteria displayed an absorbance ratio less than 1.

A.2 Syringe Pumps

Solutions were pumped through the column using syringe pumps (kd Scientific KDS 230) to reduce the pulsation of flow caused by peristaltic pumps, which have been used in past experiments[1]. Experimental solutions were not stirred or sonicated while held in syringes. An additional experiment was run to support the validity of using syringe pumps without stirring or sonication, showing that the C_0 for the *E. coli* O157:H7 and *E. coli* O157:H7 + TiO_2 scenarios changed less than 3% over a length of time similar to an experiment.

A.3 Instrument Limitation: Not Allowing Multiple Refractive Indices

For the mixture of *E. coli* O157:H7 and TiO_2, DLS measurements indicate the effective size of the bacteria is much smaller than that for bacteria in the presence of CuO. This is contradicted by SEM images. The contradiction is hypothesized to be due to the higher refractive index of TiO_2, compared to *E. coli* O157:H7 or CuO. TiO_2 may dominate

dynamic light scattering measurements. It is hypothesized that the smaller effect of TiO_2 on DLS size measurements of *E. coli* 25922 is due to the TiO_2 being more covered by EPS in this scenario.

A.4 Bacteria:Nanoparticle Number Ratio Calculations

Table A.4.1 Calculations of number ratio of bacteria to nanoparticles.

Particle Concentrations of TiO_2	
[TiO_2](mg/mL)	0.01
Density of anatase TiO_2 (mg/cm3)	3900
TiO_2 Particle radius (cm/particle)	0.0000061
TiO_2 Volume (cm3/particle)	9.50776E-16
Primary particles TiO_2/mL solution:	2.70E+09
Particle Concentrations of CuO	
[CuO](mg/mL)	0.01
Density of CuO (mg/cm3)	6315
CuO Particle radius (cm/particle)	0.0000025
CuO Volume (cm3/particle)	6.54498E-17
Primary particles CuO/mL solution:	2.42E+10
Bacteria:Nanoparticle Ratios	
TiO_2 primary particles per 10^9 cells / mL:	2.7
CuO primary particles per 10^9 cells / mL:	24.2

A.5 DLVO Modeling

The interaction energy profiles for particle-particle, particle-spinach, and particle-quartz systems are presented in Figure A.5.1, Figure A.5.2, and Figure A.5.3, respectively. DLVO modeling predicted key aspects of experimental results. As indicated by SEM images and Figure A.5.1, both nanoparticles appear to interact with both bacteria species in suspension. Also, the breakthrough curves for *E. coli* O157:H7 alone and in the presence of CuO are consistent with the primary minimum deposition predicted by DLVO theory. In addition, more column elution was observed during the DI H_2O rinse of the *E. coli* + TiO_2 scenario than during the other scenarios with the pathogen. UV-VIS adsorption analysis revealed that *E. coli* was the main species appearing in the effluent. Therefore, the pathogen was more stable in the presence of TiO_2, as predicted in Figure A.5.3.

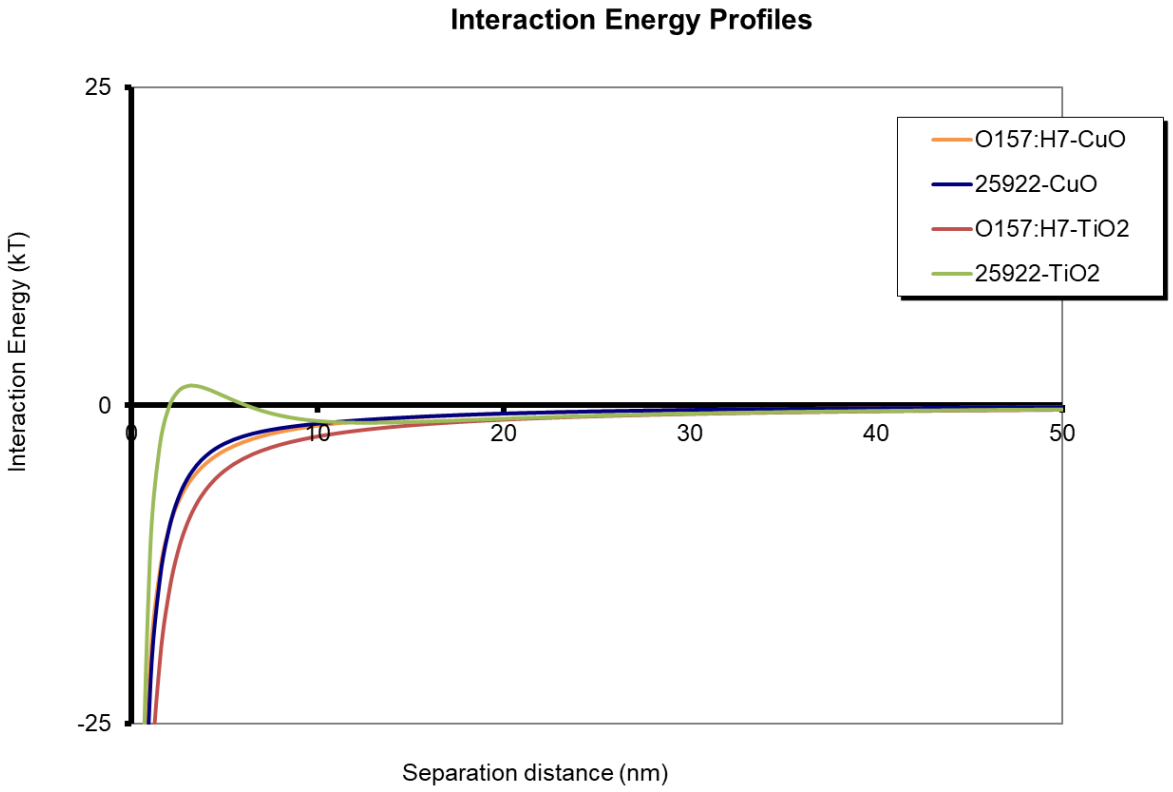

Figure A.5.1 Particle-Particle DLVO for bacteria and ENMs.

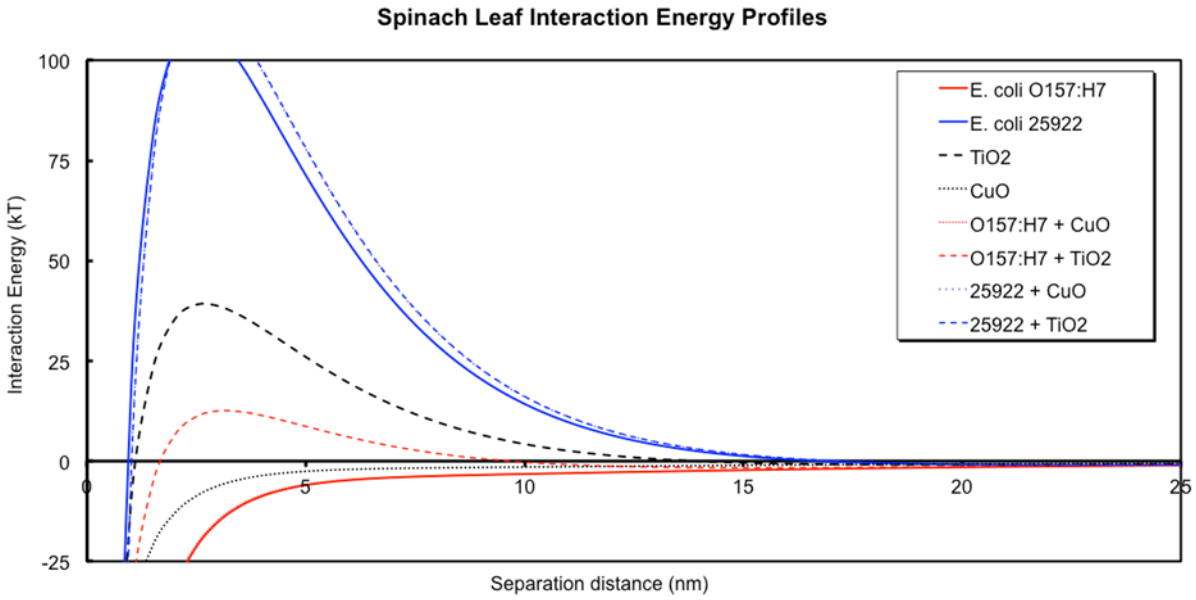

Figure A.5.2 Particle-Plate DLVO for spinach leaf surface.

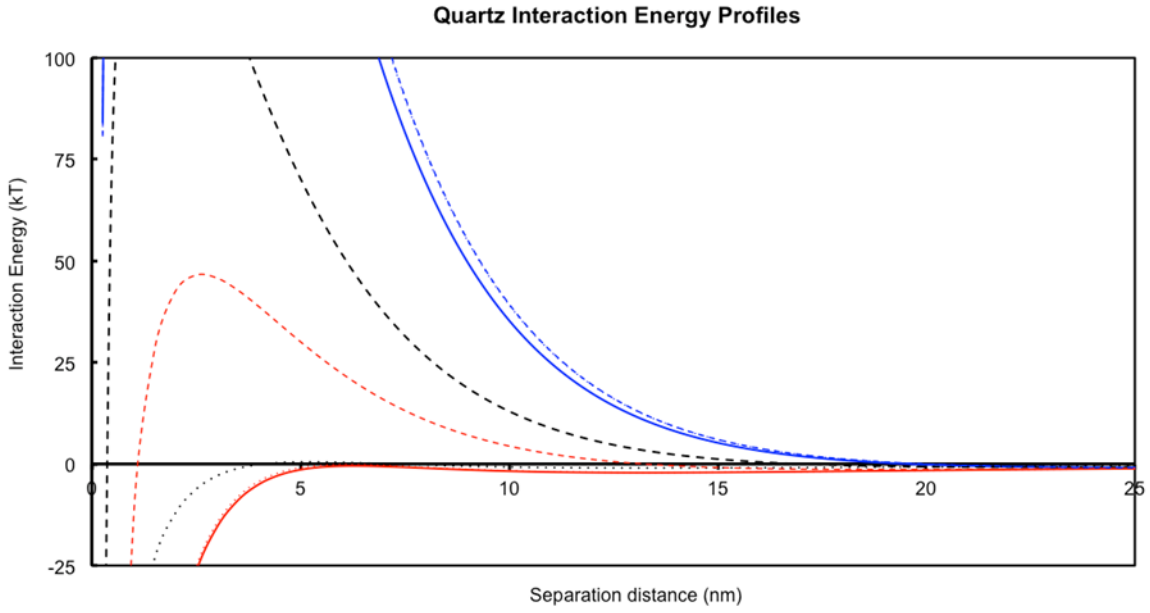

Figure A.5.3 Particle-Plate DLVO for quartz sand surface.

An initial interpretation of DLVO results may lead the reader to conclude that most of the *E. coli* O157:H7 in the presence of TiO_2 should elute during the H_2O rinse. This would be a rational conclusion since a previous study with *E. coli* retained in a saturated sand column under unfavorable deposition conditions showed that the majority of bacteria were eluted from the column upon decreasing the ionic strength of the pore fluid, behavior consistent with secondary minimum deposition[1]. However, in the current study, only a fraction of the *E. coli* in the presence of TiO_2 elutes during the DI H_2O rinse.

It is likely that only a small portion of the *E. coli* O157:H7 cells have meaningful interaction with TiO_2. Based on the hydrodynamic diameter of TiO_2 in the absence of *E. coli*, TiO_2 concentration is estimated to be 10^7 aggregates/mL, while the *E. coli* O157:H7 is present at 10^9 cells/mL. Therefore, it is logical that the majority of the cells exhibit behavior that is consistent with DLVO predictions for *E. coli* in the absence of TiO_2.

A.6 DLVO Shortcomings

Based on DLVO predictions, *E. coli* O157:H7 should irreversibly deposit onto the spinach and quartz surfaces, due to its nearly neutral cell surface charge. Meanwhile, more highly charged *E. coli* 25922 should experience greater repulsive forces, so it should attach less and detach more. Instead, attachment rate coefficients onto spinach are around the same magnitude for both the pathogen and non-pathogen scenarios in the flow cell. Also, significant detachment of *E. coli* O157:H7 cells is observed in the flow cell (up to 18% of attached cells), while essentially no detachment of *E. coli* 25922 is observed. In addition,

only partial release of *E. coli* 25922 is observed in the column (62% retention after DI rinse).

Similarly, the presence of TiO2 in suspension with *E. coli* O157:H7 is predicted to hinder irreversible bacteria attachment. However, TiO_2 has little effect on the pathogen's attachment and detachment in the flow cell. Moreover, *E. coli* O157:H7 exhibits a likely increase in retention in the column in the presence of TiO_2.These observations indicate DLVO interactions are not the primary factors influencing bacterial adhesion. This is in agreement with previous work[4].

A further shortcoming of DLVO modeling is that it predicts the elution of the majority of TiO_2 in the column in the absence of *E. coli*. However, little TiO_2 release was observed. Similar behavior of food grade TiO_2 was previously observed[5]. This behavior may be due to hydrophobic interactions of the TiO_2 nanoparticles.

A.7 *E. coli* Deposition Mechanisms

Some hypotheses for DLVO failing to predict *E. coli* deposition/detachment trends are based on physical shortcomings of the theory. Previous work found that colloid deposition kinetics were insensitive to particle size, despite DLVO theory predicting a decrease in particle deposition with increasing particle size[6]. It is possible that DLVO over-estimates the interaction energy for bacteria (relatively large particles) with surfaces. Furthermore, the equation that was used for van der Waals attraction between *E. coli* and surfaces in DLVO predictions, which assumes sphere-plate geometry, may under-estimate

their attraction. Rod-shaped *E. coli* are expected to have greater van der Waals attraction to a surface than their spherical counterpart[7].

Other hypotheses for *E. coli* deposition deviating from DLVO theory are biological in nature. Cell surface heterogeneity and bacteria population heterogeneity may provide for primary minimum deposition in spite of DLVO calculations[1]. In addition, the larger amount of EPS observed with *E. coli* 25922 (Figure 2.1) may facilitate additional surface interactions with quartz, irrespective of charge barriers.

Extra EPS may also contribute to the larger *E. coli* 25922 aggregates observed in DLS measurements, and thus physical straining. The straining hypothesis for *E. coli* 25922 in the column is supported by the bumpy retention profile shown in Figure A.7.1. The curve bumpiness is in contrast to the scenarios with *E. coli* O157:H7, where there is a steep decrease in absorbance with increasing depth, due to favorable deposition conditions. In the hypothetical absence of straining, there is already a hypothesized difference between *E. coli* O157:H7 and *E. coli* 25922 retention profiles: the *E. coli* 25922 retention profile may be less consistent with classical colloid filtration theory due to repulsive DLVO interactions[8].

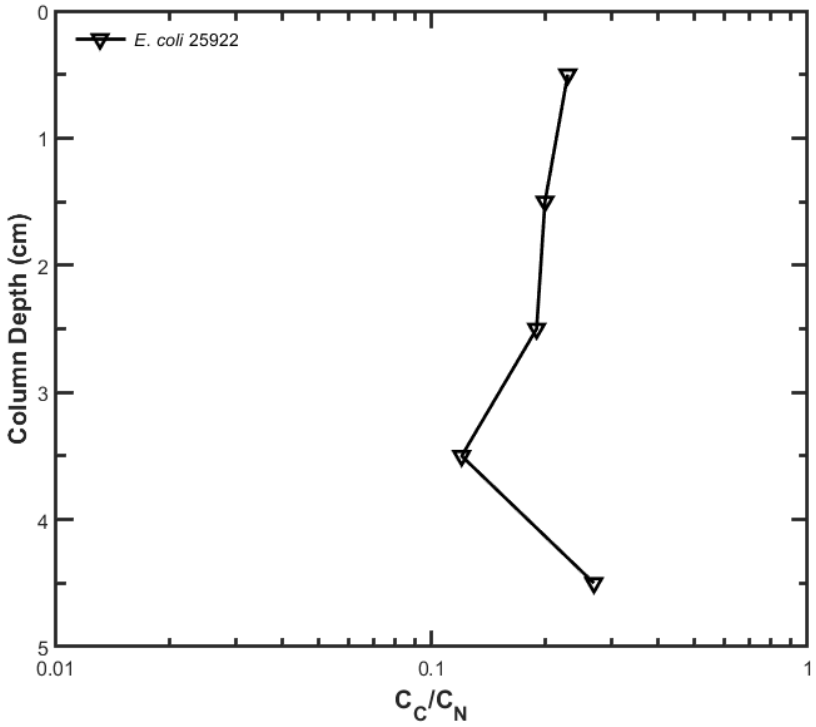

Figure A.7.1 Column retention profile for column transport experiment with *E. coli* 25922. C_C and C_N are defined as concentration of recovered particles and the sum of concentrations of recovered particles for a given suspension, respectively. A depth of 0 cm corresponds to the entrance of the column.

However, the bumpy nature of the *E. coli* 25922 retention profile is different than the hypothesized deviation from classical colloid filtration theory. In previous work, a correlation can be seen between bumpy column deposition profiles and straining of *E. coli*[9]. In this work, bumpy column deposition profiles often coincided with breakthrough curves that had an upward-sloping breakthrough plateau, as seen in the *E. coli* 25922 scenario of Figure A.7.2. Furthermore, it is logical that the slightly larger *E. coli* 25922 would be strained in 275 μm sand grains when previous work showed that *E. coli* O157:H7 was

strained in 240 μm sand grains[9]. Other potential reasons for non-exponential deposition profiles are discussed elsewhere[9].

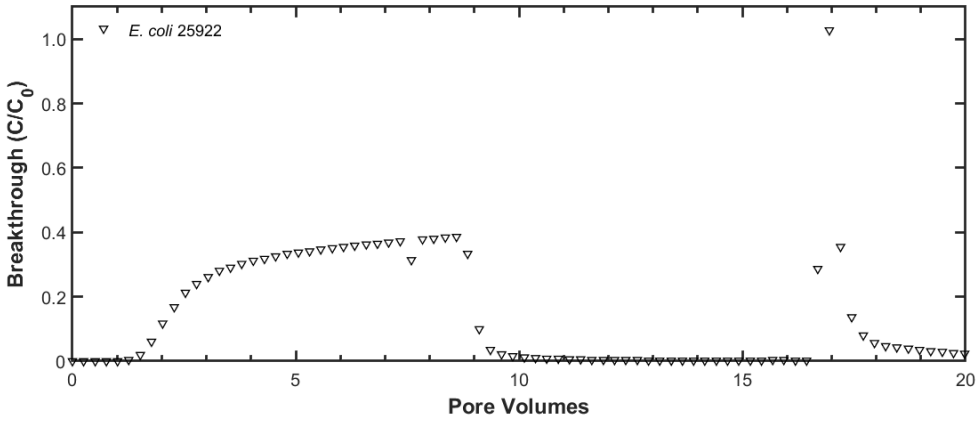

Figure A.7.2 Breakthrough curve for saturated sand column transport experiment with *E. coli* 25922. Columns were injected with 10^9 cells/mL in 10 mM KCl electrolyte at pH 7. There are no error bars because only one replicate was completed. Experimental conditions: Darcy velocity = 1 cm/min, Pe = 65[10], bed length = 5 cm, bed diameter = 1.5 cm, porosity = 0.44, average grain diameter = 275μm.

A.8 DLVO Modeling Assumptions and Qualifications

Calculations of effective hydrodynamic diameter and zeta potential were used to generate DLVO predictions. Zeta potentials of -5 and -25 mV were used as estimates of net charges for spinach surfaces and quartz grains, respectively, based on previous work[1,11].

The Van der Waals equation used in DLVO modeling of sphere-plate interaction is valid for separation distances of up to about 20% of the sphere radius[12]. For the limiting case of CuO nanoparticles, the DLVO calculations are estimated to be valid up to 47 nm (based on hydrodynamic diameter), by which point the DLVO curve is asymptotic.

The electrical double layer (EDL) equation used in the DLVO modeling of sphere-plate interaction is exact for surface potentials less than 25mV[13]. At higher surface potentials, this equation appears to be a good approximation for separation distances that are greater than 3 nm in 10 mM KCl, based on Table 1 of the referenced article[13]. Since the interaction energy barriers of highly charged particles in Figure A.5.1 and Figure A.5.2 extend past 3 nm, the EDL equation is considered valid. Another requirement for the validity of the EDL equation is that the double layer thickness be small relative to the particle size, which is easily satisfied for the limiting condition of CuO nanoparticles in 10 mM KCl.

A.9 References

1 Redman, J. A., Walker, S. L. & Elimelech, M. Bacterial Adhesion and Transport in Porous Media: Role of the Secondary Energy Minimum. *Environmental Science & Technology* **38**, 1777-1785, doi:10.1021/es034887l (2004).

2 Baran, W., Makowski, A. & Wardas, W. The effect of UV radiation absorption of cationic and anionic dye solutions on their photocatalytic degradation in the presence TiO2. *Dyes and Pigments* **76**, 226-230 (2008).

3 Begot, C., Desnier, I., Daudin, J. D., Labadie, J. C. & Lebert, A. Recommendations for calculating growth parameters by optical density measurements. *Journal of Microbiological Methods* **25**, 225-232 (1996).

4 Mayton, H. M., Marcus, I. M. & Walker, S. L. Escherichia coli O157: H7 and Salmonella Typhimurium adhesion to spinach leaf surfaces: Sensitivity to water chemistry and nutrient availability. *Food microbiology* **78**, 134-142 (2019).

5 Waller, T., Marcus, I. M. & Walker, S. L. Influence of septic system wastewater treatment on titanium dioxide nanoparticle subsurface transport mechanisms. *Analytical and bioanalytical chemistry*, 1-8 (2018).

6 Elimelech, M. & O'Melia, C. R. Effect of particle size on collision efficiency in the deposition of Brownian particles with electrostatic energy barriers. *langmuir* **6**, 1153-1163 (1990).

7 Vold, M. J. Van der Waals' attraction between anisometric particles. *Journal of Colloid Science* **9**, 451-459 (1954).

8 Tufenkji, N. & Elimelech, M. Deviation from the classical colloid filtration theory in the presence of repulsive DLVO interactions. *Langmuir* **20**, 10818-10828 (2004).

9 Bradford, S. A., Simunek, J. & Walker, S. L. Transport and straining of E. coli O157: H7 in saturated porous media. *Water Resources Research* **42** (2006).

10 Lanphere, J. D., Rogers, B., Luth, C., Bolster, C. H. & Walker, S. L. Stability and transport of graphene oxide nanoparticles in groundwater and surface water. *Environmental engineering science* **31**, 350-359 (2014).

11 Elimelech, M., Nagai, M., Ko, C.-H. & Ryan, J. N. Relative insignificance of mineral grain zeta potential to colloid transport in geochemically heterogeneous porous media. *Environmental science & technology* **34**, 2143-2148 (2000).

12 Gregory, J. Approximate expressions for retarded van der Waals interaction. *Journal of Colloid and Interface Science* **83**, 138-145 (1981).

13 Hogg, R., Healy, T. W. & Fuerstenau, D. Mutual coagulation of colloidal dispersions. *Transactions of the Faraday Society* **62**, 1638-1651 (1966).

Appendix B: Uniform Terminology for Chapter 3

The proposed uniform terminology is illustrated and described in Chapter 3 and Table B.1 serves as a glossary.

Table A.9.1: Glossary of the proposed uniform terminology for sharpshooter functional foregut and related anatomy. The uniform terminology uses a one-term, one-meaning approach. The superscript "PH" indicates that a specific term is proposed herein (Chapter 3).

Terminology	Description
Alimentary canal	The digestive tract of the insect, which starts at the true mouth and ends at the anus. It is composed of the true foregut, midgut, and hindgut.
Anterior	See Figure 3.2A and figure caption. This directional term points toward the space in front of the insect. In the alimentary canal, this term also indicates regression along the alimentary canal.
Apodemal groove	See Figure 3.4A. The central groove of the cibarial diaphragm. On the anterior/dorsal (in blue-green sharpshooters) side of the cibarial diaphragm, the cibarial dilator muscle attaches to the apodeme.
Basin	See Figure 3.3A. A segment of the precibarium. It includes an epipharyngeal segment and a hypopharyngeal segment (see Figure 2B, 2C).

Terminology	Description
Basin crease[PH]	See Figures 3.4D, 3.5B. The ventral (in blue-green sharpshooters) segment of the groove at the proximal end of the basin.
Basin lateral groove[PH]	See Figure 3.4D. The groove that separates the egl fold distal/lateral wall from the remainder of the egl fold.
Basin periphery[PH]	See Figure 3.4D. A segment of the groove at the proximal end of the basin.
Basin protuberances	See Figure 3.4C, 3.4D. The segments of the bulbous protrusion of the epipharynx that are a part of the epipharyngeal basin.
Basin proximal slope[PH]	See Figures 3.4D, 3.5B. The proximal-most segment of the groove at the proximal end of the basin.
Basin triangles[PH]	See Figures 3.4D, 3.5B. The segments of the groove at the proximal end of the basin where triangular patches of shag carpet-like *X. fastidiosa* biofilm form.
Bell-like invagination	A potential segment of the epipharyngeal basin, based on microscope observations of a spittlebug [1].
Central roof depression[PH]	See Figures 3.4A, 3.5B. A depression in the cibarium roof.
Cibarial diaphragm	See Figure 3.2A – C. The membranous segment of the cibarium.

[PH] This term is proposed herein.

Terminology	Description
Cibarial epipharyngeal trough[PH]	See Figures 3.4A, 3.4D, 3.5B. The proximal-most segment of the epipharyngeal trough.
Cibarium	See Figure 3.2A – C. The proximal-most segment of the preoral cavity; the sucking pump.
Cibarium bowl	The apposition of the floor and roof of the cibarium.
Cibarium chamber	The lumen (cavity) of the cibarium.
Cibarium floor	See Figures 3.2B, 3.5A. The hypopharyngeal segment of the cibarium.
Cibarium roof	See Figures 3.2C, 3.5B. The epipharyngeal segment of the precibarium.
Cuticular flap	A potential segment of the epipharyngeal basin, based on microscope observations of a spittlebug [1]. In Chapter 3, this term is merged with precibarial valve to get precibarial valve/flap.
D-sensilla	Precibarial chemosensilla that lie in the D-sensilla field.
D-sensilla field	See Figure 3.3A – C. A segment of the distal enclosure where the D-sensilla lie.
Distal	See Figure 3.2A and figure caption. This directional term indicates regression along the preoral cavity.

[PH] This term is proposed herein.

Terminology	Description
Distal dip[PH]	See Figures 3.4B, 3.5A. A segment of the hypopharyngeal basin.
Distal enclosure[PH]	See Figure 3.3A – C. The second of four segments of the precibarium. It includes an epipharyngeal segment and a hypopharyngeal segment.
Distal epipharyngeal basin[PH]	See Figure 3.4C.
Distal flap transition[PH]	See Figures 3.4B, 3.4C, 3.5A, 3.5B. The segment of the distal enclosure where the distance between the left and right hypopharyngeal edge flaps decreases, making the shape of a triangle. The distal flap transition includes the epipharyngeal distal enclosure segment apposed to the hypopharyngeal edge flap distance transition segment.
Distal trough[PH]	See Figures 3.4B, 3.4D, 3.5A, 3.5B. The distal segment of the trough. It includes an epipharyngeal segment and a hypopharyngeal segment.
Dorsal	See Figure 3.2A and figure caption. A directional term that points toward the space above the insect in Figure 3.2A.
Egl[PH]	An abbreviation for "epipharyngeal."

[PH] This term is proposed herein.

Terminology	Description
Epipharyngeal basin	See Figure 3.3C. The segment of the basin that is on the epipharynx.
Epipharyngeal basin upper walls[PH]	See Figure 3.4D.
Epipharyngeal fold[PH]	See Figure 3.4D. A segment of the epipharyngeal basin.
Epipharyngeal fold central groove	See Figures 3.4D, 3.5B. Composed of the lower central groove and upper central groove.
Epipharyngeal fold distal/lateral wall[PH]	See Figure 3.4D.
Epipharyngeal fold distal groove[PH]	See Figures 3.4D, 3.5B.
Epipharyngeal fold proximal face[PH]	See Figures 3.4D, 3.5B.
Epipharyngeal precibarial walls	See Figure 3.2C. The epipharyngeal surfaces of the precibarium.
Epipharyngeal trough	See Figure 3.3C. The segment of the trough that is on the epipharynx.

[PH] This term is proposed herein.

Terminology	Description
Epipharyngeal trough upper walls[PH]	See Figure 3.4D.
Epipharyngeal trough peak[PH]	See Figure 3.4D. This includes small portions of the medial epipharyngeal trough and distal epipharyngeal trough.
Epipharynx	See Figure 3.2C.
Esophageal valve	The valve that separates the true foregut from the midgut.
Esophagus	The second segment of the true foregut in sharpshooter insects.
Functional foregut	The combination of the precibarium and cibarium.
Groove at the proximal end of the basin	See Figure 3.4D. A segment of the epipharyngeal basin. The portion of the epipharyngeal precibarial walls that this term includes was slightly altered herein.
Gustatory organ	A group of precibarial chemosensilla (D-sensilla, H-sensilla, or P-sensilla).
H-sensilla	Precibarial chemosensilla that lie on the hypopharynx.
Hgl[PH]	An abbreviation for "hypopharyngeal."
Hindgut	The third (last) segment of the alimentary canal.
Hypopharyngeal basin converging segment[PH]	See Figures 3.4B, 3.5A.

[PH] This term is proposed herein.

Terminology	Description
Hypopharyngeal edge flaps[PH]	See Figure 3.5A. The flaps on the edges of the hypopharyngeal precibarial walls of the distal enclosure. See also "proximal flap transition," "distal flap transition," and "medial segment of the distal enclosure."
Hypopharyngeal extension that inserts into the food canal (HEF)	See Figures 3.3A, 3.3B, 3.5A. The distal segment of the precibarium. For abbreviation and clarity, we write, "hypopharyngeal extension to stylet food canal."
Hypopharyngeal precibarial walls	See Figure 3.2B. The hypopharyngeal surfaces of the precibarium.
Hypopharyngeal trough	See Figure 3.3B. The segment of the trough that is on the hypopharynx.
Hypopharynx	See Figure 3.2B.
Lateral cibarial walls[PH]	See Figure 3.4A.
Longitudinal groove	See Figures 3.4A, 3.5A. A segment of the cibarium.
Lower face of precibarial valve/flap	See Figure 3.4D.

[PH] This term is proposed herein.

Terminology	Description
Medial hill[PH]	See Figures 3.4B, 3.5A. A segment of the hypopharyngeal basin.
Medial segment of the distal enclosure[PH]	See Figures 3.4B, 3.4C, 3.5A. The segment of the distal enclosure where the hypopharyngeal edge flap width and the distance between the left and right edge flaps remain relatively constant. The medial segment of the distal enclosure includes the epipharyngeal segment apposed to the hypopharyngeal edge flap constant-width, constant-distance segment.
Medial trough[PH]	See Figures 3.4A, 3.4B, 3.4D, 3.5A, 3.5B. The medial segment of the trough. It includes an epipharyngeal segment and a hypopharyngeal segment.
Midgut	The second (middle) segment of the alimentary canal.
P-sensilla	Precibarial chemosensilla that lie in the epipharyngeal basin.
Pharynges	Plural pharynx.
Pharynx	The first segment of the true foregut in sharpshooter insects.
Pockets of apodemal groove	See Figure 3.4A.
Posterior	See Figure 3.2A and figure caption. A directional term that points toward the space behind the insect.

[PH] This term is proposed herein.

Terminology	Description
Precibarial chemosensilla	Parts of gustatory organs in the sharpshooter precibarium.
Precibarial pit/ring	See Figure 3.3A, 3.3C, 3.4C. A segment of the epipharyngeal basin.
Precibarial valve/flap	See Figure 3.3C.
Precibarial valve/flap distal face[PH]	See Figures 3.4C, 3.5B.
Precibarial valve/flap edge[PH]	See Figure 3.4D.
Precibarial valve/flap extension[PH]	See Figures 3.4C, 3.5B.
Precibarium	See Figure 3.2, 3.3. The second of three segments of the preoral cavity.
Proximal	See Figure 3.2A and figure caption. This directional term indicates progression along the preoral cavity.

[PH] This term is proposed herein.

Terminology	Description
Proximal dip[PH]	See Figures 3.4B, 3.5A. A segment that straddles the hypopharyngeal trough and basin.
Proximal flap transition[PH]	See Figures 3.4B, 3.4C, 3.5A. The segment of the distal enclosure where the hypopharyngeal edge flaps transition to their full width. The proximal flap transition includes the epipharyngeal distal enclosure segment apposed to the hypopharyngeal edge flap width transition segment.
Rim of basin	See Figure 3.4D. The basin rim is relatively unpronounced in blue-green sharpshooters compared to glassy-winged sharpshooters.
Rim of trough[PH]	See Figure 3.4D. This is the space immediately ventral/anterior (in blue-green sharpshooters) to the corner of the epipharyngeal trough upper walls.
Ring	A potential segment of the epipharyngeal basin, based on microscope observations of a spittlebug. In Chapter 3, this term is combined with precibarial pit to get precibarial pit/ring.
Stylet food canal	See Figure 3.2A. The portion of the preoral cavity enclosed by the maxillary stylets.
Stylets	Piercing-sucking mouthparts.

[PH] This term is proposed herein.

Terminology	Description
Trough	See Figure 3.3A – C. The proximal segment of the precibarium. It includes an epipharyngeal segment and a hypopharyngeal segment.
True foregut	See Figure 3.2A. The first segment of the alimentary canal. It contains the pharynx and esophagus in sharpshooters; some insects also have a crop and a proventriculus in their true foreguts. The true foregut is generally referred to by the name "foregut," but in this publication, we add the accompanying adjective "true." This emphasizes the difference between the "true foregut" and the "foregut" described in many previous publications. In sharpshooters, the true foregut begins at the true mouth and ends at the esophageal valve.
True mouth	See Figures 3.2A, 3.2B, 3.5A. This segment separates the functional foregut from the true foregut.
Upper face of precibarial valve/flap[PH]	See Figure 3.4C.
Valve/flap contact patch[PH]	See Figures 3.4B, 3.4C, 3.5A. The segment of the distal enclosure where the hypopharynx remains bare of *X. fastidiosa* after a shag

[PH] This term is proposed herein.

Terminology	Description
	carpet-like biofilm develops. The valve/flap contact patch includes the bare hypopharyngeal segment and the apposed epipharyngeal segment.
Valve/flap shadow[PH]	See Figure 3.4D. A region of the epipharyngeal fold that remains hidden in dorsal/distal views of the blue-green sharpshooter egl basin. It also exists in other sharpshooter species and is delimited based on equivalent views of the egl basin in those species.
Ventral	See Figure 3.2A and figure caption. A directional term that points toward the space below the insect in Figure 3.2A.

[PH] This term is proposed herein.

B.1 References

1 Ruschioni, S. *et al.* Functional Anatomy of the Precibarial Valve in *Philaenus spumarius* (L.). *PLoS ONE* **14**, e0213318 (2019).

Appendix C: Supplemental Information for Chapter 3

C.1 3D Model Dimensions

Table C.1.1 Dimensions of the 3D model of the blue-green sharpshooter functional foregut, as illustrated in Figure 3.1. Dimensions were estimated based on published microscopy images of blue-green sharpshooters, except where Alves et al. (2008) was cited[1]. hgl: hypopharyngeal; egl: epipharyngeal; HEF: hypopharyngeal extension that inserts into the stylet food canal.

#	Anatomical Feature	Length (μm)	References used to estimate length
A1	Longitudinal groove depth	4	[2]
A2	Longitudinal groove width	26	Longitudinal grove width in the 3D model is around 26 μm^3.
A3	Cibarium length radius	290	[3]
A4	True mouth length radius	0.6*cibarium length radius	[1]
A5	True mouth cylinder diameter	50	[1]
A6	Cibarium floor radius	215	[2]

A7	Cibarium lateral radius	124	Estimated as 137 μm, but the dimension is 124 μm in the 3D model[2,3]
A8	Cibarium roof radius	130	[2]
A9	Cibarial diaphragm side wall length	1.5*cibarium length radius	[1]
A10	Apodemal groove width	11	[2]
B1	HEF distal lateral diameter	12	[4,5]
B2	Distal enclosure distal flap transition + HEF narrowing segment length	48	[3,4]
B3	Distal enclosure distal flap transition triangle base	11.5	[4,6]
B4	Distal enclosure widening segment (proximal flap transition + medial segment) length	35	[4,6]
B5	Distal enclosure valve contact patch distal lateral diameter	14.5	[4-6]
B6	Distal enclosure valve contact patch distal depth	10	[5,6]

B7	Hgl distal enclosure valve contact patch length	9	[4-6]
B8	Egl distal basin valve extension inner medial diameter	9	[5]
B9	Protruding valve segment length	4	[3,5,6]
B10	Protruding valve segment width	10	[3,5,6]
C1	Hgl basin distal dip length	13	[6]
C2	Hgl basin medial hill length	13	[6]
C3	Egl basin width	17.5	[3,6]
C4	Egl fold diameter (parallel to C3)	0.5*egl basin width	[3,6]
C5	Egl basin cone distal diameter	17	[6]
C6	Egl basin cone length	9	[6]
C7	Egl groove at the proximal end of the basin: basin entrance length	8	[6]
C8	Hgl trough distal diameter	20	[4,6]
C9	Hgl proximal dip length	20	[6]
C10	Hgl distal trough length	38	[4,6]

C11	Egl distal trough distal diameter	14	[6]
C12	Egl trough length ratio medial:distal	34:23	[6]
C13	Egl medial-distal trough diameter	12	[3,6]
C14	Hgl medial-distal trough diameter	15	[4,6]
C15	Hgl medial trough length	42.5	[4,6]
C16	Hgl trough proximal diameter	20	[2-4,6]
C17	Egl cibarial-medial trough diameter	20	[2,3,6]
C18	Cibarial trough proximal depth	67	[2]
C19	Cibarial trough deep proximal lateral diameter	9	[2]

C.2 Comparison of 3D Model with Micro-CT Measurements

After the 3D model was made using microscopy images, micro-CT measurements of blue-green sharpshooters were published[7]. The micro-CT measurements show a different cibarium shape than our 3D model (Figure C.2.1).

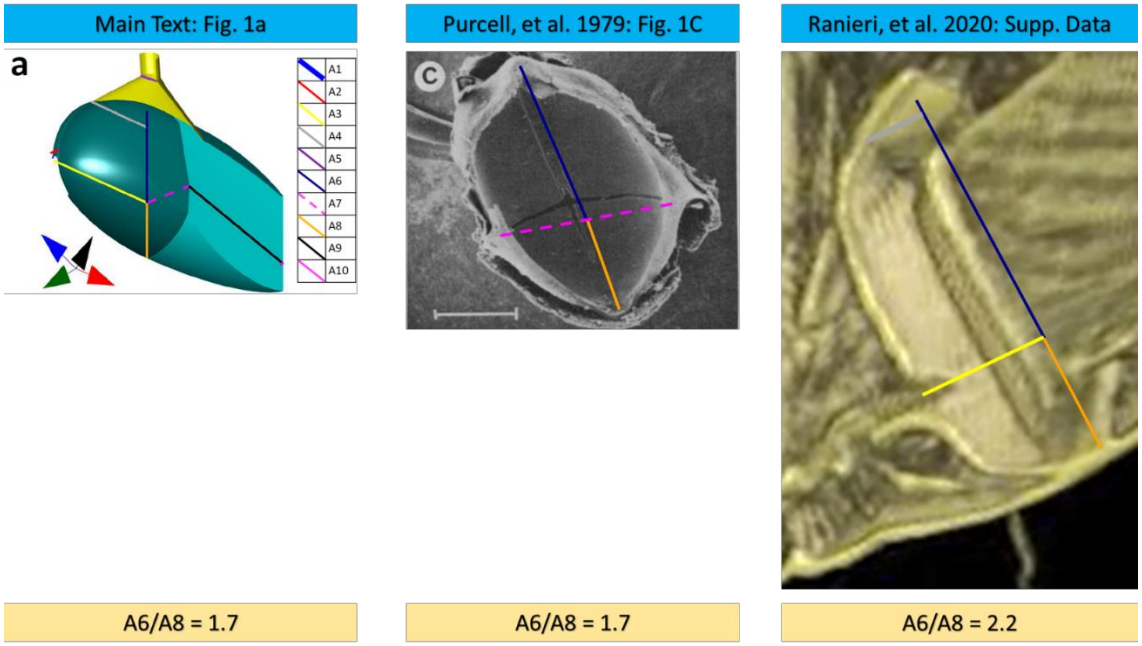

Figure C.2.1 Comparison of cibarium shape in a microscope image and a micro-CT measurement. The dimensions A6 and A8 in Figure 3.1 of the main text are based on measurements from a microscope image published by Purcell, et al. (1979)[2] (From Purcell, A. H., Finlay, A. H. & McLean, D. L. Pierce's disease bacterium: mechanism of transmission by leafhopper vectors. *Science* 206, 839-841 (1979). Reprinted with permission from AAAS.). The ratio of A6 to A8 is different in the image from Purcell, et al. (1979) than in the micro-CT measurement from Ranieri, et al (2020)[7] (Reprinted from Journal of Insect Physiology, Vol 120, Emanuele Ranieri, Gianluca Zitti, Paola Rioloa, Nunzio Isidoro, Sara Ruschioni, Maurizio Brocchini, Rodrigo P.P. Almeida, Fluid dynamics in the functional foregut of xylem-sap feeding insects: A comparative study of two *Xylella fastidiosa* vectors, 103995, Copyright 2020, with permission from Elsevier.). This may be due to biological variability.

The micro-CT study reports a 130° bend in the precibarium[7]. Our 3D model has a 117° bend at that location (Figure C.2.2), which is within 10% of 130°. The length the of precibarium was reported to be 154 µm based on micro-CT[7]. Our 3D model is 168 µm long between the points where the trough meets the cibarium and where the distal enclosure meets the HEF (Figure C.2.2). While 168 µm is an underestimate due to the curviness of the precibarium, it is within 10% of 154 µm. Therefore, our 3D model is in reasonable agreement with micro-CT measurements.

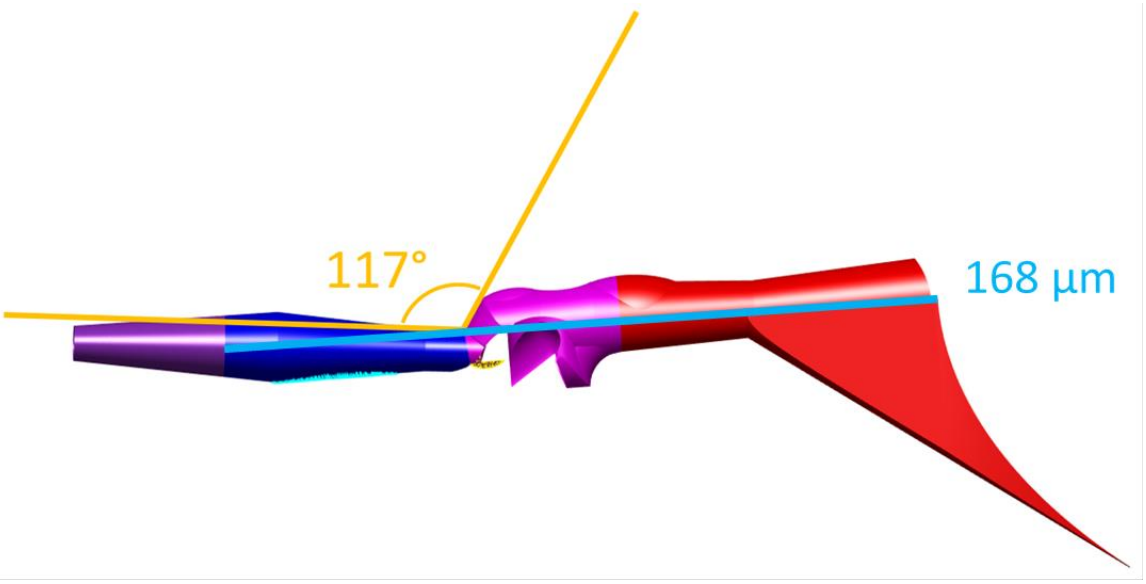

Figure C.2.2 Measurements of the 3D model of the precibarium for comparison with Ranieri et al. (2020)[7].

C.3 References

1 Alves, E. *et al.* Retention sites for *Xylella fastidiosa* in four sharpshooter vectors (Hemiptera: Cicadellidae) analyzed by scanning electron microscopy. *Current Microbiology* **56**, 531-538 (2008).

2 Purcell, A. H., Finlay, A. H. & McLean, D. L. Pierce's disease bacterium: mechanism of transmission by leafhopper vectors. *Science* **206**, 839-841 (1979).

3 Rapicavoli, J. N. *et al.* O antigen modulates insect vector acquisition of the bacterial plant pathogen *Xylella fastidiosa*. *Appl. Environ. Microbiol.* **81**, 8145-8154 (2015).

4 Purcell, A. H. & Almeida, R. P. Characterization and studies on the fundamental mechanisms of *Xylella fastidiosa* transmission to grapevines by the glassy-winged sharpshooter. in *Pierce's Disease Research Symposium.* 115 -117.

5 Almeida, R. P. & Purcell, A. H. Patterns of *Xylella fastidiosa* colonization on the precibarium of sharpshooter vectors relative to transmission to plants. *Annals of the Entomological Society of America* **99**, 884-890 (2006).

6 Newman, K. L., Almeida, R. P., Purcell, A. H. & Lindow, S. E. Cell-cell signaling controls *Xylella fastidiosa* interactions with both insects and plants. *Proceedings of the National Academy of Sciences* **101**, 1737-1742 (2004).

7 Ranieri, E. *et al.* Fluid dynamics in the functional foregut of xylem-sap feeding insects: a comparative study of two *Xylella fastidiosa* vectors. *Journal of Insect Physiology* **120**, 103995 (2020).

Appendix D: Supplemental Information for Chapter 4

D.1 Results

D.1.1 Full Insect Simulations

Figure 4.3 displays insect simulation results that pertain to the precibarium. Figure D.1.1 displays the full insect simulation results, with both the precibarium and cibarium. Predicted drag forces are low almost everywhere except the precibarium.

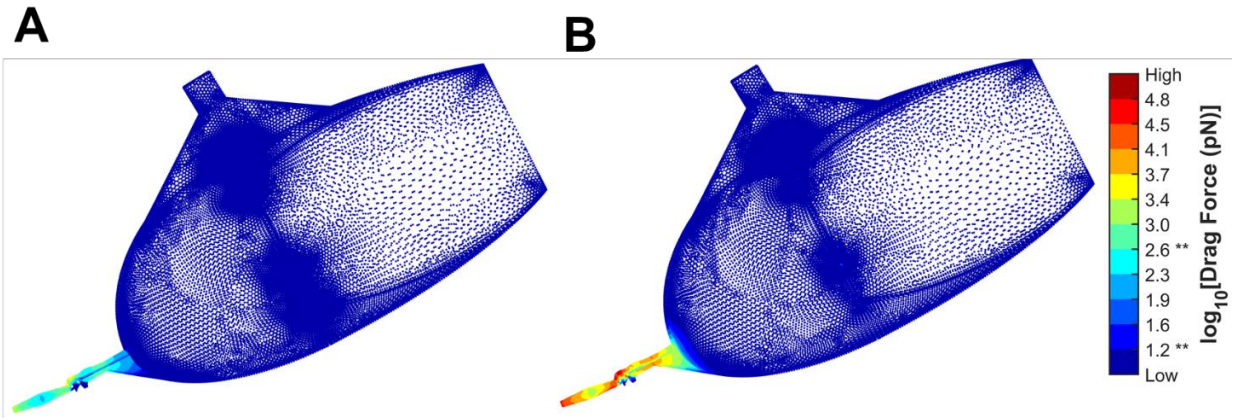

Figure D.1.1 Full insect simulation results, including the precibarium, cibarium, and true mouth. The results for the precibarium are examined closely in Figure 4.3. These heat maps are of simulated drag forces acting on individually surface attached bacteria in the blue-green sharpshooter during feeding. During ingestion (A), drag forces are generally lower than during egestion (B). The ** symbols on the colormap are references to key drag forces in the results of Fuente et al.[1]. $10^{1.2}$ pN (15.85 pN) represents the minimum drag force that caused meaningful detachment of individually surface-attached *Xylella fastidiosa*. When the drag forces in the referenced work were sequentially increased, representative results showed that over 70% of *X. fastidiosa* detached by the time the drag forces reached $10^{2.6}$ pN (443.8 pN)[1].

D.1.2 Second View of Figure 4.3 Results

Figure 4.3 of the main text displays insect simulation results that pertain to the precibarium. Figure D.1.2 displays precibarium results from another viewpoint that is useful for analyzing results.

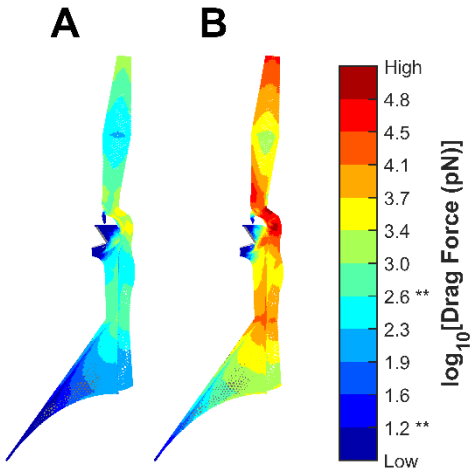

Figure D.1.2 Precibarial insect simulation results, displayed in a different arrangement than in Figure 4.3 of the main text. The hypopharyngeal and epipharyngeal results are apposed, with only the left half of the precibarium visible. During ingestion (A), simulated drag forces are generally lower than during egestion (B).

D.1.3 Generally Useful Simulation Results

Table D.1.1 Potentially useful quantities calculated from insect simulations.

Cibarium volume[1] (nL)	28.6
Precibarium volume (nL)	0.0558
Surface area of precibarium (μm^2)	14241
Surface area of precibarium + cibarium + true mouth (μm^2)	625070
Ingestion flow rate (m^3/s)	$3.37*10^{-11}$
Egestion flow rate (m^3/s)	$4.80*10^{-10}$

[1] See Figure D.3.2 for calculation method.

Table D.1.2 Flowrates calculated for the *Undisturbed* xylem simulations.

Vessel Diameter (μm)	Flowrate (nL/s)
20	0.1
30	0.6
40	1.9
50	4.6
60	9.7
70	17.9
80	30.7
90	49.4
100	76.0
110	111.4
120	157.0
130	236.6
140	321.4
150	384.8
160	502.9
170	639.1
180	804.0
190	998.7
200	1228.8

D.2 Discussion

D.2.1 Timing of Bacteria Acquisition

Bacteria is likely acquired in the precibarium primarily during X wave (XW) feeding for multiple reasons. First, this behavior likely creates harsher flow environments for xylem biofilms than sustained ingestion (C2) feeding (Fig. 2): XW feeding causes the high drag forces associated with egestion and the back-and-forth fluid motion associated with the insect alternating between ingestion and egestion. In contrast, C2 does not include egestion and causes more of a start-stop motion. This means the maximum xylem drag forces are predicted to be 14 times higher during XW feeding than during C2 feeding in the vessels where ingestion is relevant for bacteria detachment. Harsher flow conditions cause more xylem-dwelling bacteria to detach and enter the functional foregut as planktonic bacteria and floating bacteria aggregates. Higher floating bacteria concentrations cause more attachment in the precibarium, since bacteria deposition rates can be approximated as being proportional to floating bacteria concentration[2].

In addition, XW feeding comes before C2 feeding and is inferred to have multiple waveform events per swallow[3]. Since XW comes before C2 in a selected xylem vessel, the bacteria prone to detachment may already be detached by the time C2 occurs. Also, for each C2 waveform event, there is a corresponding swallow of xylem sap. Conversely, multiple XC1 waveform events typically occur before the next swallow, which is inferred to occur during the first XC2 event (XC1 and XC2 are parts of XW). This means planktonic bacteria concentrations during successive XC1 events can build up and lead to higher deposition rates in the functional foregut.

Still, there is a chance that bacteria acquisition in the precibarium occurs mainly during C2 feeding instead of XW feeding. As discussed in the results, water hammer likely occurs during C2 feeding. Presumably, water hammer shockwaves could travel from the precibarial valve, through the stylet food canal, and into the xylem to detach bacteria. Additionally, the duration of C2 feeding behavior can be on the order of hours, while the duration of XW feeding is on the order of minutes[3]. Longer durations may allow for more bacteria acquisition in the precibarium during C2 feeding due to the rate-based nature of bacterial deposition[2]. Therefore, the timing of when the bulk of bacteria acquisition occurs is a tradeoff between fluid dynamics, insect anatomy, xylem anatomy, and insect feeding behaviors.

D.2.2 Locations of Initial Bacteria Acquisition

Based on current results (Figure 4.3 and Figure 4.4), initial bacteria acquisition in the precibarium is mainly expected to occur near the precibarial pit/ring, the valve/flap shadow, and the cibarial epipharyngeal trough. Acquisition is expected in these low flow regions during ingestion and egestion because shear forces required to prevent bacteria deposition are generally lower than those required to detach the same bacteria[4]. While there appear to be 0.5 to 5 second pauses between the ingestions of XC2 events that could greatly increase the surface area in the precibarium available for attachment[3], these are not expected to greatly alter the sites of initial acquisition. In the case that bacteria attach under the inferred quiescent conditions of XC2 pauses, the majority are likely swept away by the ensuing ingestion flowrates because bacteria typically exhibit bond-strengthening with a surface on a time-scale of minutes after initial adhesion[2]. If anything, acquisition during

XC2 pauses is mainly expected to expand the region of acquisition in the precibarial trough, which has a relatively low gradient of predicted drag forces (Fig. 3). Therefore, most initial acquisition is inferred to occur in low-flow regions of the precibarium.

D.3 Methods

D.3.1 Xylem Simulations

D.3.1a *Illustrated Methods*

Fluid dynamics in grapevine xylem vessels were simulated in COMSOL Multiphysics® (COMSOL, Inc., Stockholm, Sweden), as illustrated in Figure D.3.1.

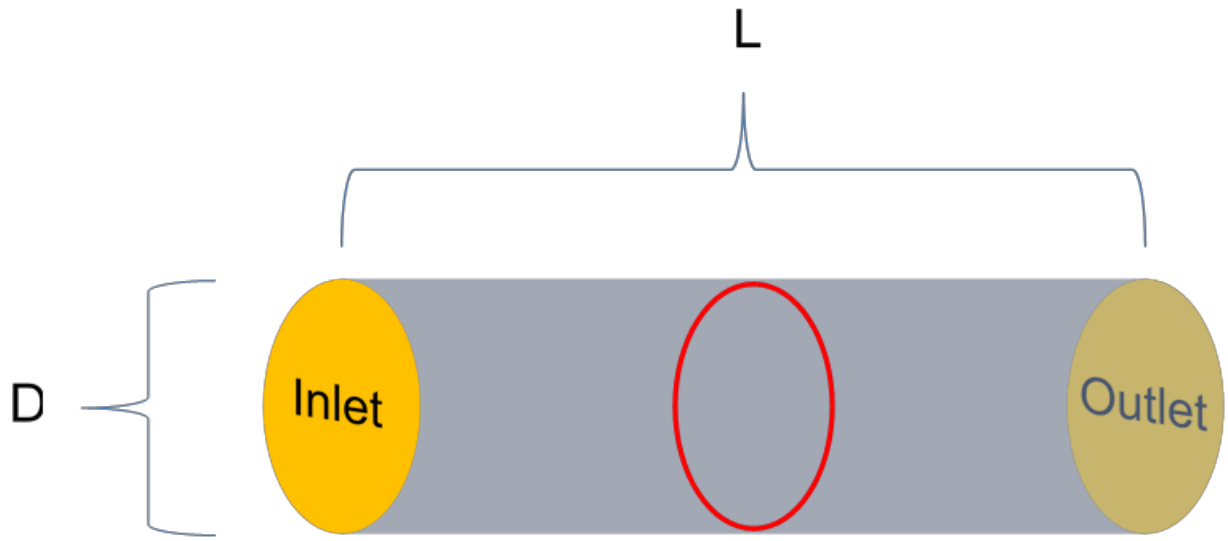

Figure D.3.1 Arrangement for both undisturbed and disturbed xylem simulations. 3D cylinders were used, with inlet and outlet specified based on the type of simulation. The length (L) of cylinders was 100 µm. The diameter (D) of cylinders was increased stepwise from 20 µm to 200 µm by increments of 10 µm using a parametric sweep for each simulation. At the midpoints of the cylinders, edge probes (red) were used to calculate velocities and shear rates near the walls of the cylinder, which were used to calculate the drag forces acting on individually surface attached bacteria. The edge probes were in the shape of circles with radii equal to that of the cylinder, minus 0.2887 µm.

D.3.1b *Simulation Inputs*

In the *Undisturbed* simulation, the boundary conditions were specified based on a water potential gradient of 0.03 MPa/m, which was previously reported for both well-

irrigated and water-stressed grapevines.[5] The water potential gradient was modeled as a pressure potential gradient, so the pressure drop across the pipe was (0.03 MPa/m)(100e-6 m) = (3e-6 MPa). The inlet and outlet were specified to have fully developed flow with average pressures corresponding to the calculated pressure drop.

In the *Ingestion* and *Egestion* simulations, flowrates were specified by dividing the calculated volume of the insect cibarium by the duration of filling and emptying of the cibarium during C2. Next, these flowrates were divided by two to account for an assumed equal partitioning of flow in xylem vessels upstream and downstream of penetrating stylets. The xylem vessel (cylinder) inlets were specified to have fully developed flow with flow rates of (1.685 e-11 m^3/s) and (2.4e-10 m^3/s) for *Ingestion* and *Egestion* simulations, respectively.

D.3.1c *Calculation of Simulation Inputs*

In the *Ingestion* and *Egestion* simulations, flowrates were specified by dividing the calculated volume of the insect cibarium by the durations of filling and emptying of the cibarium during C2, and then dividing by two. The volume was calculated from our 3D model of the cibarium and the durations were estimated based on published electropenetography (EPG) recordings[3].

Our 3D model of the cibarium accounted for 5 dimensions aimed to mimic the cibarium of blue-green sharpshooters[6]. Our calculated volume ignored the volume added to the cibarium by the precibarium, longitudinal groove, and true mouth, as shown in Figure D.3.2. Using COMSOL Multiphysics®, a volume of 2.86e-11 m^3, or 28.6 nanoliters was

calculated. This calculated volume is comparable to the 8.7e-11 m^3 reported elsewhere based on a different volume estimation method[7].

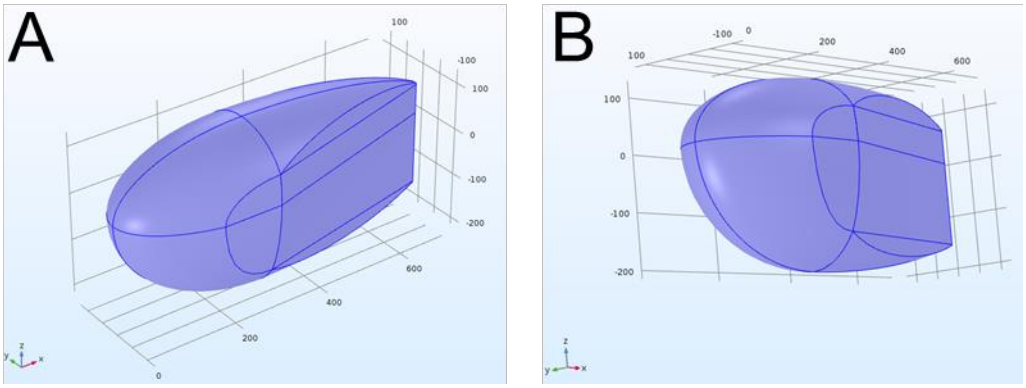

Figure D.3.2 3D model of the blue-green sharpshooter cibarium used for estimating the cibarium volume. The precibarium, longitudinal groove, and true mouth geometries were not included in this calculation. The model is shown from two different angles in COMSOL Multiphysics®. It has a calculated volume of 28.6 nanoliters.

The durations of ingestion and egestion required to fill and empty the cibarium were estimated from published from EPG recordings of blue-green sharpshooters feeding on grapevine[3]. The flowrates of ingestion and egestion during XC1 and XC2 were assumed to be the same as the flowrates of ingestion and swallowing during C2. The regularity of the C2 waveform allows for estimation of the time required to fill and empty the cibarium.

The repetition rate for C2 was reported as 1.1 Hz by Backus et al. under the conditions of 10^9 ohms, AC, and silver glue[3]. Based on their figure illustrating C2 EPG recordings under conditions of 10^7 and 10^8 ohms, AC, and silver paint, we estimated the ratio of the duration of C2 ingestion and swallowing as 14.24:1.

Therefore, the estimated durations of C2 cibarium filling and emptying are 0.849 s and 0.0597 s, respectively. These durations, together with the cibarium volume, yield estimated ingestion and egestion flow rates of 3.37e-11 m^3/s and 4.80e-10 m^3/s, respectively. These flowrates were divided by two for xylem vessel *Ingestion* and *Egestion* simulations because it was assumed that flow is equally partitioned upstream and downstream of a penetrating stylet.

D.3.1d *Probe Locations*

As illustrated in Figure D.3.1, velocities and shear rates in the fluid dynamic simulations of xylem vessels were probed 0.2887 μm from the cylinder walls. Concentric ring edge probes were used in simulations to avoid inconsistencies associated with point probes, which yield slightly variable measurements depending on their angular position. This variability may be due to the limitations of finite element calculations in the fluid dynamic simulations, which use a mesh-based method. The concentric ring edge probes were positioned at the midpoint of the 100 μm long cylinders to avoid entrance and exit effects.

D.3.1e *Mesh Refinement*

Xylem simulations used "Fine" physics-controlled meshes in COMSOL Multiphysics®. The accuracy of the "Fine" mesh setting was evaluated by comparing results between this mesh setting an the next-best mesh setting "Normal". Results were compared at a variety of cylinder diameters, a variety of calculated drag forces, and both types of boundary condition sets by running the *Undisturbed* and *Egestion* simulations with "Normal" physics-controlled meshes. Results with "Normal" meshes were within 8% of

results with “Fine” meshes. On average, there was a 1% difference between “Fine” and “Normal” results.

D.3.1f *Additional Assumptions*

1. The viscosity of xylem sap is the same as that of water[8]. Xylem sap is an incompressible[9] Newtonian[10] fluid that can be modeled by the Navier-Stokes equations at the size scale of interest[11].
2. Xylem flow is laminar and steady state, and there is no slip at xylem vessel walls.
    a. Laminar flow was verified based on the *Egestion* simulation of the 20 μm xylem vessel. The Reynolds number was calculated to be 15.

D.3.2 Insect Simulations

D.3.2a *Illustrated Methods*

Fluid dynamics in the blue-green sharpshooter precibarium and cibarium during feeding were simulated in COMSOL Multiphysics® (COMSOL, Inc., Stockholm, Sweden), as illustrated in Figure D.3.3.

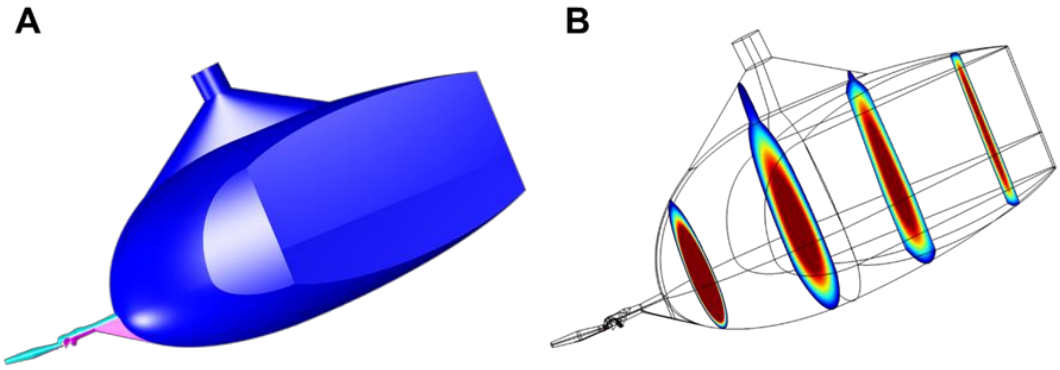

Figure D.3.3 Contextualization of insect fluid dynamic simulations. A) The 3D model of the blue-green sharpshooter precibarium and cibarium, which was described in another study using different coloring to label the model[6]. The precibarial epipharynx (magenta) and precibarial hypopharynx (cyan) are emphasized here as the portions of the 3D model used in Figure 3 of the main text. The blue portion of the 3D model includes the cibarium and true mouth, in which fluid dynamics were also simulated, but the results for this region are only included in the supporting materials (herein). B) Fluid dynamics were simulated in the whole 3D model, including the precibarium, cibarium, and true mouth. Red regions in the slice plot indicate areas with high fluid velocities and blue regions indicate regions with low velocities. Full fluid dynamic simulation results are described in more detail above.

The simulation results presented in the main text are focused on the precibarium of the insect, as illustrated in Figure D.3.4.

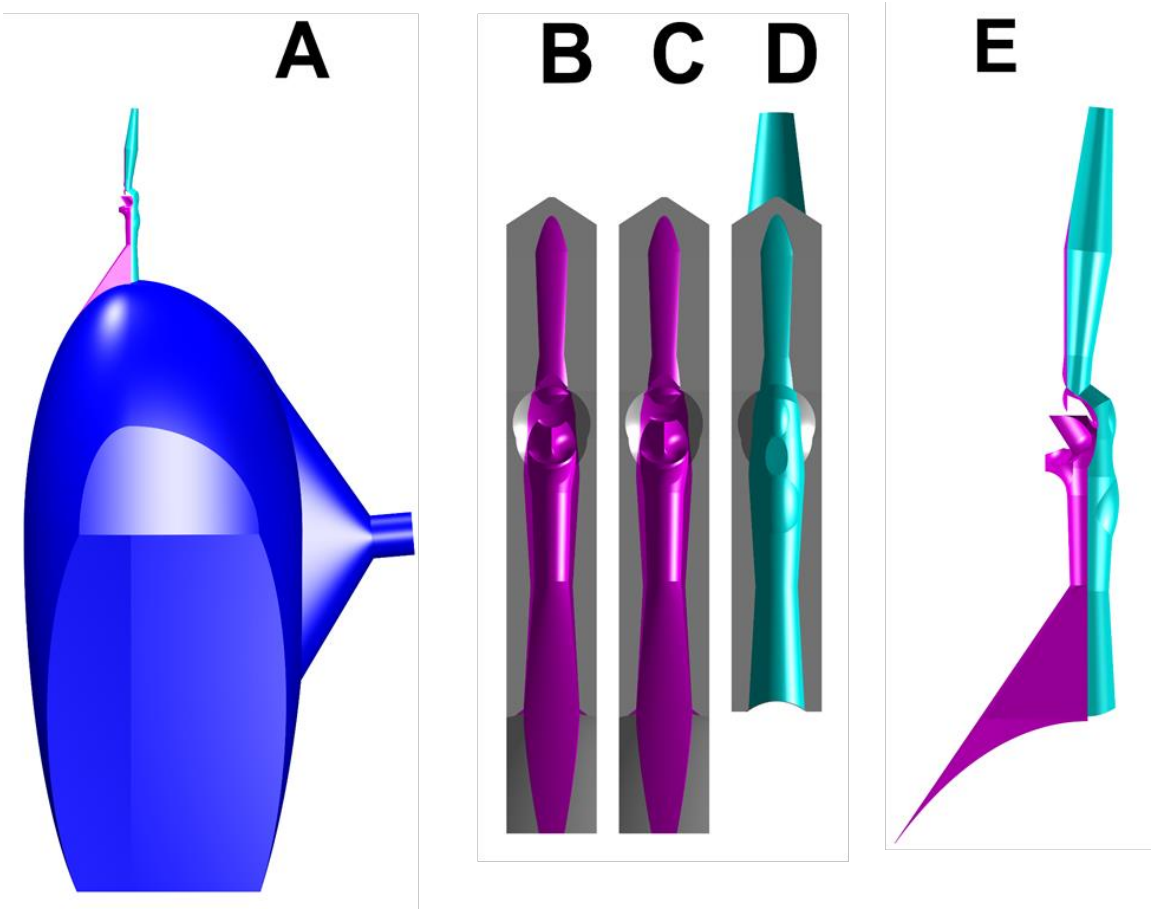

Figure D.3.4 Illustrated derivation of the 3D molds used for displaying heat maps of drag forces. A) The 3D model of the blue-green sharpshooter precibarium and cibarium shown in Figure D.3.3, rotated for comparison with subsequent subfigures. B) The precibarial epipharynx (magenta) from subfigure A plotted within a gray representation of a portion of the epipharynx. The precibarial valve is in the same position as in the previously reported 3D model[6]. C) A very similar 3D mold to that presented in subfigure B, except that a portion of the precibarial valve is sticking out into the lumen of the precibarium. This represents the inferred position of the precibarial valve during egestion, due to fluid drag. The precibarial valve of aster leafhoppers has been described as hollow and mainly composed of cuticle[12], so we infer that the blue-green sharpshooter precibarial valve is flexible and deformed during outflow. The deformed precibarial valve was included in the 3D model used for the egestion simulation. The 3D models used for ingestion and egestion simulations were only different in this respect. D) The precibarial hypopharynx (cyan) from subfigure A plotted within a gray representation of a portion of the hypopharynx. E) Half of the precibarial epipharynx and hypopharynx from subfigure A. This portion of the 3D model provides an alternative way of presenting heat maps of drag forces.

The cibarial diaphragm was used as the outlet and inlet for the ingestion and egestion simulations, respectively, as illustrated in Figure D.3.5.

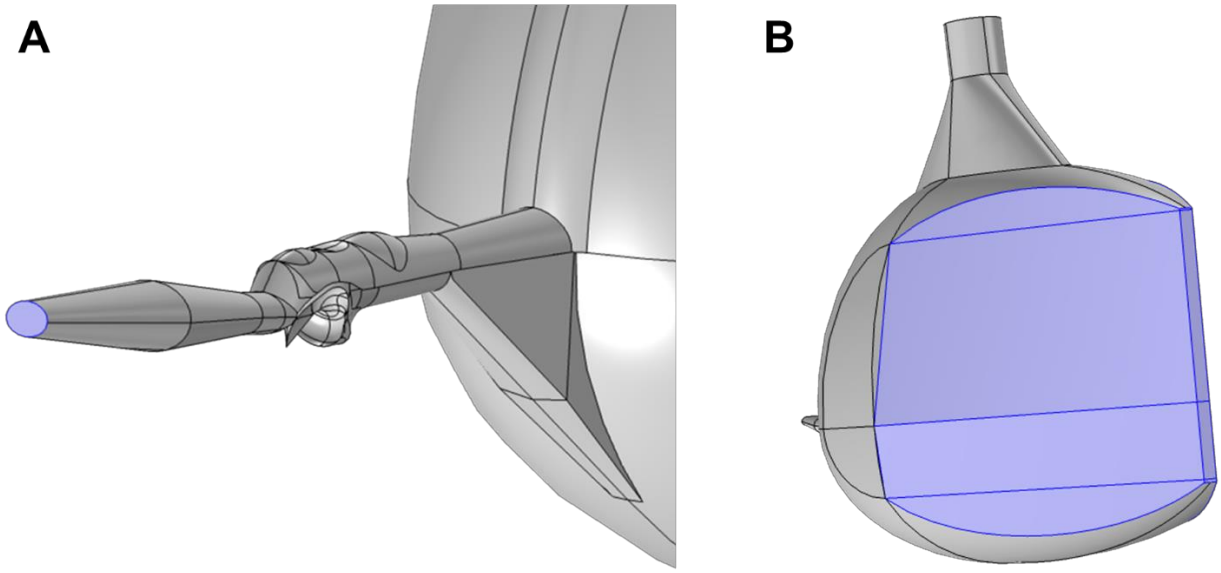

Figure D.3.5 The inlet (A) and outlet (B) used for the ingestion simulation, indicated in blue. The blue regions identify the entrance to the HEF (A) and a symmetrical section of the cibarial diaphragm (B). The inlet and outlet were reversed (swapped) for the egestion simulation. HEF: hypopharyngeal extension that inserts into the stylet food canal.

D.3.2b *Simulation Inputs*

In the ingestion and egestion simulations, fluid velocities were specified for the section of the cibarial diaphragm indicated in Figure D.3.5B. This indicated section served as the outlet for the ingestion simulation and the inlet for the egestion simulation, simulating the effects of the cibarial diaphragm being extended and released by the cibarial dilator muscles. Specified velocities were 0.14 mm/s and 2.0 mm/s for the ingestion and egestion simulations, respectively.

D.3.2c *Calculations and Validation of Simulation Inputs*

Specified velocities at the cibarial diaphragm are derived from the ingestion and egestion flowrates calculated above (section D.3.1c). These flowrates were divided by the surface area of the indicated section of the cibarial diaphragm (Figure D.3.5B) to calculate boundary velocities:

$$\hat{Q}_{boundary\_ingestion} = \frac{3.37 * 10^{-11}\, m^3/_s}{2.4 * 10^{-7} m^2} = 1.4 * 10^{-4} \frac{m}{s}$$

$$\hat{Q}_{boundary\_egestion} = \frac{4.80 * 10^{-10}\, m^3/_s}{2.4 * 10^{-7} m^2} = 2.0 * 10^{-3} \frac{m}{s}$$

Boundary velocities were specified as perpendicular to the cibarial diaphragm to mimic the effects of diaphragm extension and relaxation.

D.3.2d *Temperature: Heat Transfer Simulation*

The temperature of xylem sap in insect fluid dynamic simulations was carefully chosen to be 20 °C because the viscosity of sap is affected by its temperature, which is affected by the insect temperature. The chosen sap temperature is a Fermi estimate based on heat transfer simulations and an analysis that accounts for sharpshooter feeding behavior. The Fermi estimate is explained below, followed by a sensitivity analysis of insect fluid dynamic simulations with respect to sap temperature.

Heat transfer simulations predict that the xylem sap in the precibarium and cibarium is at the same temperature as the insect. Before sap enters the precibarium, it travels through the stylet food canal and is likely warmed by the proboscis of the insect, which we infer has a similar temperature to the insect body. In blue-green sharpshooters, the stylet food canal has a mean area of 28 μm^2 and the proboscis is around 650 μm long [7,13]. Since the

ingestion flowrate is estimated to be $3.37*10^{-11}$ m^3/s, the average velocity in the stylet food canal while the xylem sap is warming is 1.2 m/s. The maximum velocity is twice the average velocity, or 2.4 m/s, assuming Hagen Poiseuille flow. This means the fastest moving xylem sap spends 0.27 milliseconds moving through the proboscis.

Our time-dependent heat transfer simulations predict that xylem sap reaches the temperature of the containing walls' boundary layer by the time it enters the precibarium. Time-dependent heat transfer simulations were conducted for a cylinder of stationary water with a constant temperature boundary condition, as shown in Figure D.3.6.

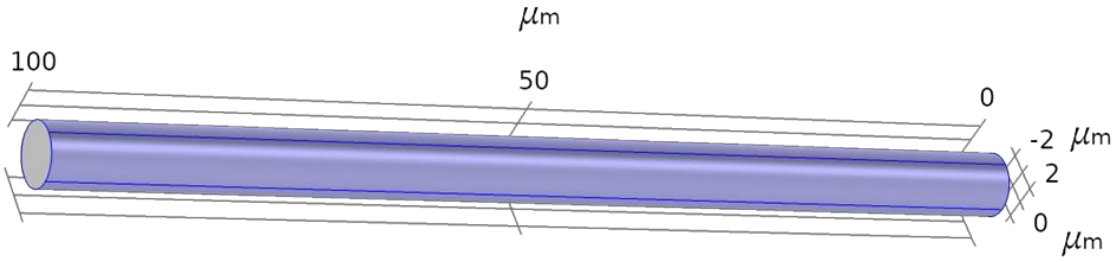

Figure D.3.6 Illustration of the heat transfer simulation in COMSOL Multiphysics®. Heat transfer was simulated between a solid cylinder of water and its constant temperature boundary, indicated in blue. The ends of the cylinder (gray) were specified as thermal insulation. The cylinder had a radius of 3 µm and a length of 100 µm. While the *Heat Transfer in Solids* interface was used, the properties of liquid water were used in the simulation.

The constant temperature boundary condition was specified as 14 °C higher than the initial temperature of the water based on the maximum expected temperature difference between the insect and xylem sap. This maximum expected temperature difference was estimated based on the size of the insect, its temperature difference from ambient air, and the temperature difference between air and xylem sap.

The mass of blue-green sharpshooters was estimated based on the mass of glassy-winged sharpshooters. Since glassy-winged sharpshooters that fed on grapevines had dry weights of 10 – 15 mg[14], and because blue-green sharpshooters are around half the size of glassy-winged sharpshooters, the mass of blue-green sharpshooters is estimated as 10^{-5} kg.

The maximum expected difference between ambient temperature and blue-green sharpshooter body temperature was estimated using measurements made on another insect that is also in the infraorder Cicadina, *Diceroprocta apache*[15]. The body mass of *Diceroprocta apache* was measured as $7*10^{-5}$ kg, so the maximum body-air temperature difference for this insect (12 °C) is expected to be greater than that for blue-green sharpshooters, since larger insects generally have a larger maximum body-air temperature differences. Therefore, 12 °C is a conservative estimate for the maximum temperature difference between a blue-green sharpshooter and ambient air.

The temperature difference between ambient air and xylem sap was estimated for laboratory conditions where plants may be cooler than air due to transpiration and a lack of solar radiation. A previous study cited how elevated atmospheric concentrations of carbon dioxide causes partial stomatal closure, leading to reduced transpiration from plant leaves[16]. Associated increases in canopy temperature by 0.3 – 1.7 °C have been observed[16]. This supports our choice of a 2 °C temperature difference between xylem sap and air. Our estimate of a plant temperature lower than air is conservative since plant tissue temperatures have been reported as higher than air temperatures[17,18].

By adding 12 °C and 2 °C together, we estimate the maximum temperature difference between insect and xylem sap to be 14 °C. This was the temperature difference

used in the heat transfer simulations, which showed xylem sap can reach the temperature of its boundary in less than 0.27 milliseconds. Results are listed for two different sets of boundary conditions in Table D.3.1.

Table D.3.1 Time required for minimum water temperatures in heat transfer simulations to approach within 0.1 °C of boundary temperatures.

$T_{boundary\_initial}$ (°C)	$T_{water\_initial}$ (°C)	Time (milliseconds)
37	23	0.089
21	7	0.091

Less than 0.27 milliseconds are required for the temperature of the xylem sap in the stylet food canal to reach that of the boundary layer coating stylet food canal walls. Xylem sap draws heat out of the surrounding insect tissue. Based on the following analysis, we infer that surrounding insect tissue, and maybe the whole insect body, falls to the temperature of xylem sap inside the plant (undisturbed xylem sap).

When feeding on grapevine, glassy-winged sharpshooters consume around 20 – 30 times their dry body weight per hour[14,19]. We presume the same is true for blue-green sharpshooters. Based on this large fluid intake and the large heat capacity of water, we infer that heat flows from insects to the xylem sap they consume until the portions of the insect in close proximity with the sap reach the same temperature as xylem sap inside the plant. This inference is supported by the increase in glassy-winged sharpshooter optimal survival temperature by 20 °C when fed on a host plant instead of no host plant[20].

In summary, we infer that xylem sap in the precibarium and cibarium of the blue-green sharpshooters during feeding is usually the temperature of xylem sap in the plant. Since the insect fluid dynamic simulations were created using experimental EPG data, a plant temperature was chosen to approximate conditions during the EPG study. The study was likely conducted at room temperature, with the plants likely being slightly cooler than room temperature due to evapotranspiration and a lack of solar radiation. Unless otherwise specified, fluid dynamics simulations in this work used a water temperature of 20 °C (for both insect simulations and xylem simulations).

In reality, the temperature of xylem sap flowing through the precibarium and cibarium likely varies due to differences in ambient temperature, how long an insect has been feeding, and more. In Figure D.3.7, we compare insect fluid dynamic simulations at different temperatures to test the sensitivity of our simulation results. Temperature has little effect on simulation results.

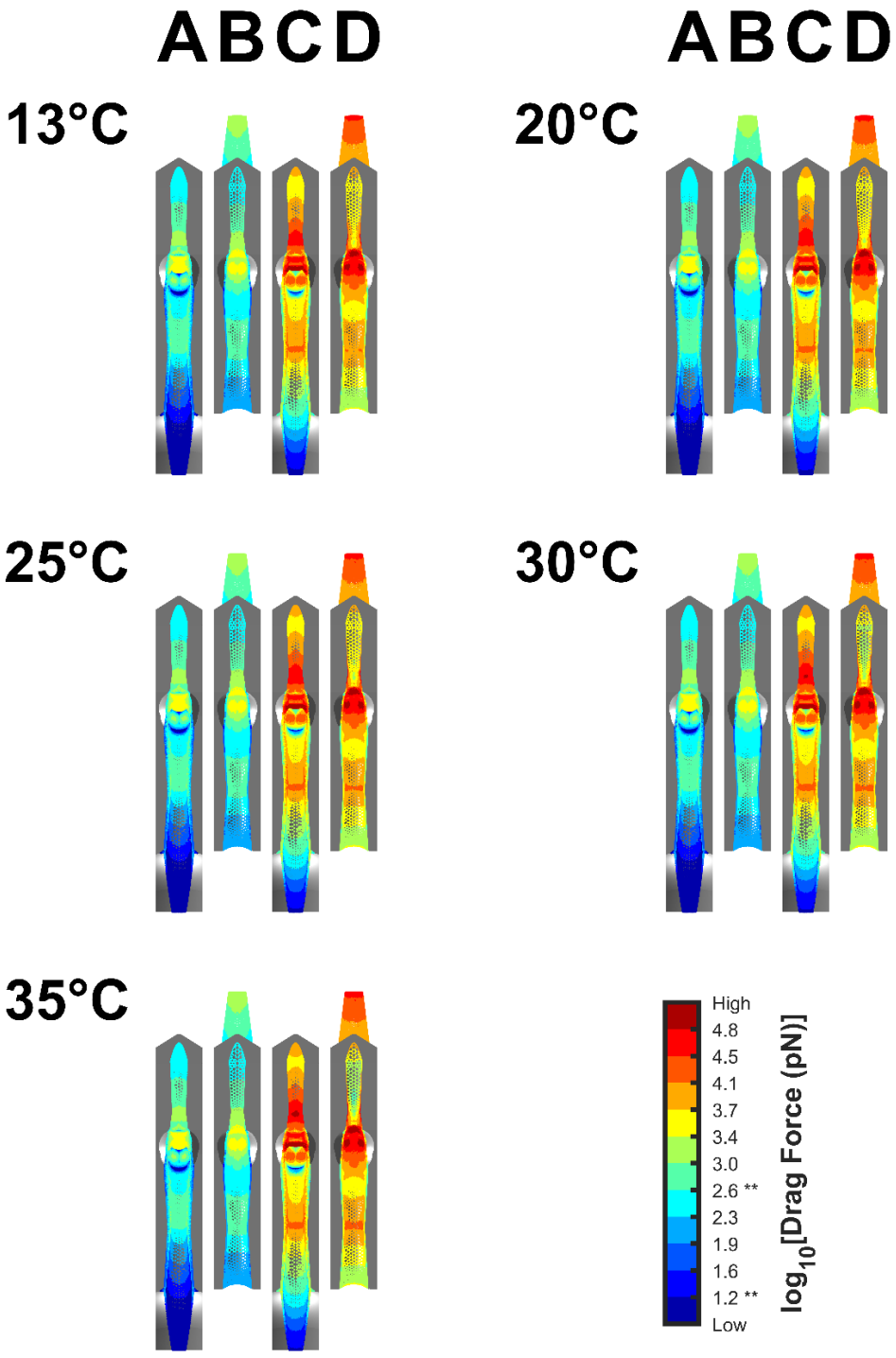
A B C D
A B C D
13°C
20°C
25°C
30°C
35°C
High
4.8
4.5
4.1
3.7
3.4
3.0
2.6 **
2.3
1.9
1.6
1.2 **
Low
log10[Drag Force (pN)]

Figure D.3.7 Temperature sensitivity analysis for insect (blue-green sharpshooter) fluid dynamic simulations.The simulation was run using xylem sap (water) at different temperatures. The 20 °C simulation results are presented in detail in Figure 3 of the main text. 13 °C – 35 °C is the range where glassy-winged sharpshooters produced excreta (fed on a host plant) in a previous study[21]. According to a previously published simulation, the temperature range of around 20 °C – 30 °C is optimal for glassy-winged sharpshooter survival on a host plant[20]. The 20 °C and 30 °C simulation results are very similar.

D.3.2e *Slip Length*

The no-slip boundary condition has traditionally been specified for most macroscopic flows[22]. In our insect simulations, this idealistic boundary condition could not be used. This is because the waxy cuticle of blue-green sharpshooters is highly hydrophobic and because of the need for precise simulation of fluid flow at the size scale of individual surface-attached bacteria. A Navier slip length of 28 nm was specified as a wall boundary condition in COMSOL Multiphysics®.

The functional foregut cuticle is expected to be smooth[23] and hydrophobic[24], with a contact angle around 105° [24-26]. The boundary slip length of water near a smooth surface with a contact angle of 98° was measured as 28 nm using colloidal probe of atomic force microscope[27,28].

D.3.2f *Probe Locations*

Velocities and shear rates in insect fluid dynamic simulations were probed 0.2887 μm from the walls. This was accomplished by using both COMSOL Multiphysics® and MATLAB. COMSOL was used to create meshes that mimicked those used for fluid dynamics simulations. These representative meshes were exported from COMSOL as .stl files and interpreted in MATLAB as triangulations. The incenters of each triangle were identified and points that were 0.2887 μm away, on triangle face normal vectors, were identified. These points were used as evaluation points in COMSOL Multiphysics® to export velocities, shear rates, and calculated drag forces.

D.3.2g *Mesh Refinement*

Insect simulations used "Finer" physics-controlled meshes in COMSOL Multiphysics®. The "Finer" mesh setting was evaluated by comparing (Figure D.3.8) results between this mesh setting and the next-best mesh setting "Fine" (except that an alteration was made to the "Fine" setting: the "Resolution of Narrow Regions" was changed from 0.7 to 0.72).

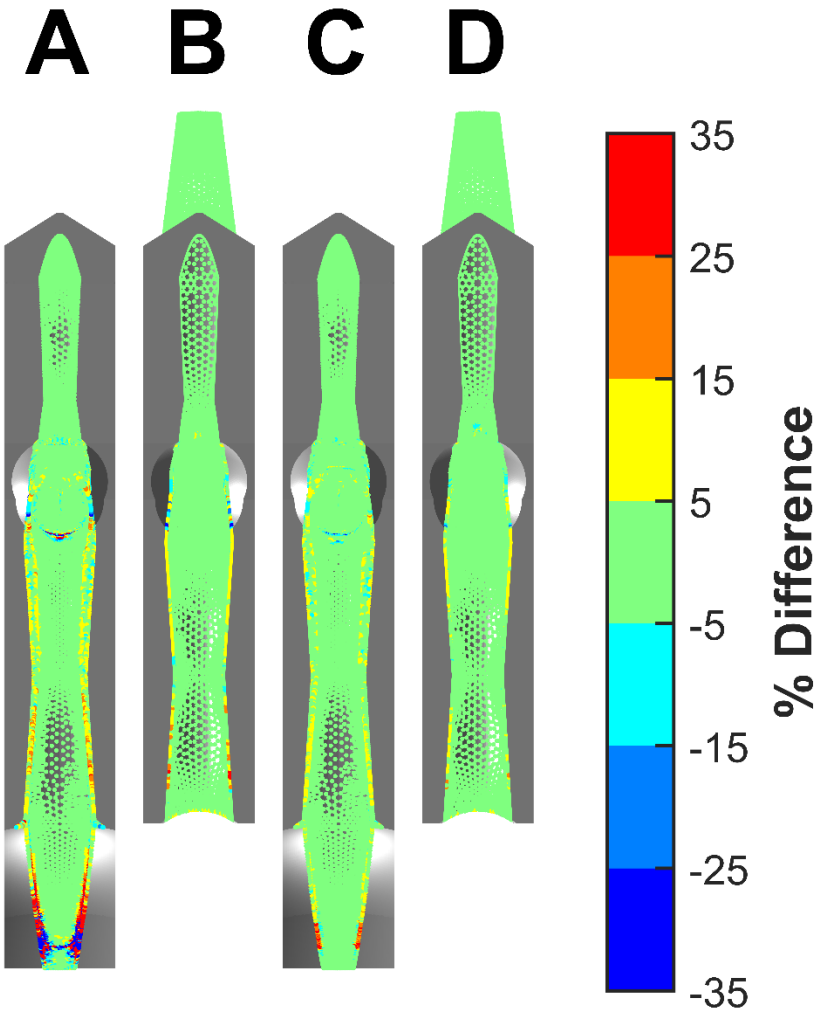

Figure D.3.8 Mesh refinement study for the insect simulations. The results in Figure 4.3 of the main text are compared with results from lower resolution simulations. The simulations in Figure 4.3 used "Finer" physics-controlled meshes in COMSOL

Multiphysics®. The lower resolution simulations used "Fine" physics-controlled meshes, with the "Resolution of Narrow Regions" changed from 0.7 to 0.72. Percent difference is displayed between the $\log_{10}$(Drag Force [pN]) of the "Finer" and "Fine" simulations. Most of the results for the lower resolution simulations are within 5% of Figure 4.3 results. Percent differences outside this range are often at stagnation zones (a small change in small drag force could be a big % difference) and sharp turns in the geometry (this may be due to the method of comparing meshes: the "Fine" simulations used the same probe locations as the "Finer" simulations).

D.3.2h *Additional Assumptions*

1. The viscosity of xylem sap is the same as that of water[8]. Xylem sap is an incompressible[9] Newtonian[10] fluid that can be modeled by the Navier-Stokes equations at the size scale of interest[11].
2. Flow is quasi-steady state.
    a. This assumption is not ideal due to the short duration of ingestion and egestion during sharpshooter feeding. However, there is a lack of information in the literature that could inform a time-dependent model. Also, the quasi-steady state model serves as a first approximation of fine scale drag forces in the precibarium and cibarium.
3. Flow is laminar. This is justified in the next section.

Laminar Flow Assumption

The laminar flow assumption is supported using the equation for calculating the Reynolds number of flow through a cylindrical pipe.

$$Re = \frac{\rho V D}{\mu} \quad (1)$$

Re = Reynolds number

V = average velocity in the pipe

D = diameter of the pipe

μ = dynamic viscosity

The average velocity can be calculated using the volumetric flowrate (Q) and the diameter of the pipe.

$$V = \frac{Q}{\pi(\frac{D}{2})^2} \tag{2}$$

Thus, the Reynolds number can be calculated using the volumetric flowrate instead of average velocity.

$$Re = \frac{4\rho Q}{\pi D \mu} \tag{3}$$

The Reynolds number increases with decreasing diameter. The thinnest location in the 3D model of the insect precibarium and cibarium that fluid flows through quickly is identified in Figure D.3.9.

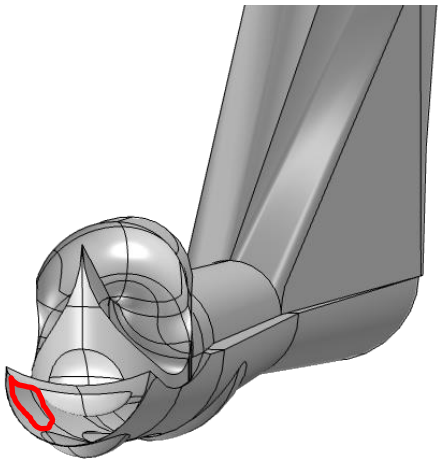

Figure D.3.9 Location in the 3D model of the precibarium and cibarium with the highest calculated Reynolds number, indicated by a red freeform shape. A section of the precibarium is shown, with the red freeform shape identifying a region between the precibarial valve and the hypopharyngeal precibarium wall.

The region indicated in Figure D.3.9 is more than 2 μm wide, so the Reynolds number is calculated using a 2 μm diameter.

$$Re = \frac{4(1000\frac{kg}{m^3})(4.8 * 10^{-10}\frac{m^3}{s})}{\pi(2 * 10^{-6}m)(8.9 * 10^{-4}\frac{kg}{m * s})} = 343$$

This Reynolds number is an overestimate since not all the xylem sap passes through the space indicated in Figure D.3.9. Also, a Reynolds number of 343 is far less than the commonly used 2100 - 2300 limit for the laminar flow assumption in cylindrical pipes. Still, the way the precibarial valve protrudes into the lumen of the 3D model suggests that a Kármán vortex street could be formed during egestion. This could cause fluctuating drag forces distal to the precibarial valve. Therefore, care should be taken when interpreting the results of fluid dynamic simulations distal to the precibarial valve. However, the laminar flow assumption is useful for estimating the order of magnitude of drag forces in the insect fluid dynamic simulations.

D.3.3 Calculated Drag Forces

D.3.3a *Summary*

The results for our xylem and insect fluid dynamic simulations are reported as drag forces acting on individually surface-attached bacteria. It would be impractical to calculate these drag forces directly, so a method was developed for estimating the drag force acting on bacteria that are hypothetically present in simulations. Drag forces are calculated using location-specific fluid velocities and shear rates. These calculations are informed by the work of De La Fuente et al.[1].

De La Fuente et al.[1] used microfluidic chamber experiments to determine the flowrates required to detach individually surface-attached *X. fastidiosa* from a glass surface. They used fluid dynamic simulations to calculate drag forces acting on bacteria as a function of these flowrates. We recreated their microfluidic chamber simulations to determine the fluid velocities and shear rates that correlated with their reported drag forces. Thus, we were able to correlate flow properties with drag forces and *X. fastidiosa* detachment. We used these correlations to calculate hypothetical drag forces in our xylem and insect simulations, as well as make inferences about *X. fastidiosa* detachment.

D.3.3b *Illustrated and Detailed Methods*

COMSOL Multiphysics® can be used to calculate fluid drag forces acting on individually surface-attached bacteria using the expression "spf.T_stressx" (Figure D.3.10)[29].

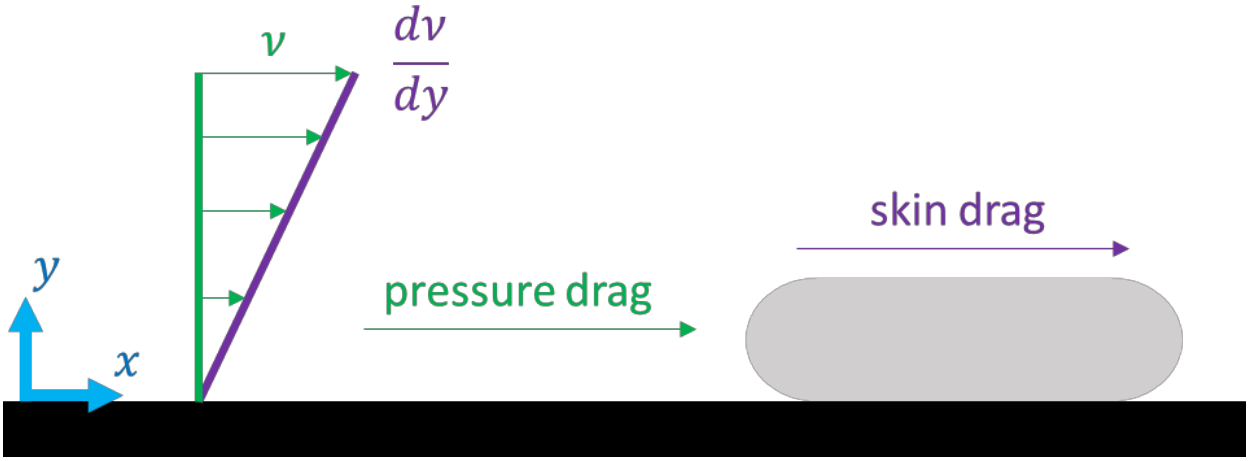

Figure D.3.10 Basic diagram of fluid flowing past a surface-attached bacterium (gray). The fluid has velocities (*v*) that are variable with respect to distance from the wall surface (*y*). The fluid also has a shear rate (*dv/dy*) that is effectively independent of distance from the wall within a separation distance of 1 µm (Table D.3.2). The

bacterium experiences both pressure drag (green) and skin drag (purple; skin drag is also known as surface drag). The total drag force can be calculated using the expression "spf.T_stressx" in COMSOL Multiphysics®[29]. The bacterium in this figure is oriented parallel to the flow for the sake of simplicity, but in our microfluidic simulations, the bacterium is oriented perpendicular to flow, as shown in Figure D.3.13.

However, this method of calculating drag forces would be impractical for both the xylem simulations and the insect simulations. It would require an impractical amount of simulations where 3D pill-shaped bacteria would be included at various locations in xylem vessels, the precibarium, and the cibarium. Instead of using this time-consuming method, properties of fluid flow were used to calculate the drag forces that would act on surface-attached bacteria if they were present (Figure D.3.11).

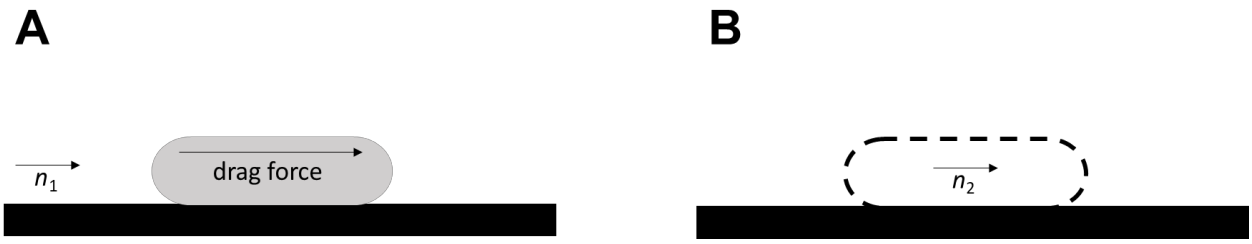

Figure D.3.11 Comparison of the methods for calculating drag forces in our microfluidic chamber simulations vs. in our xylem and insect simulations. In our microfluidic chamber simulations (A), drag forces acting on the individual surface-attached bacterium were calculated using the expression "spf.T_stressx". These drag forces were correlated with up stream flow properties (n_1: fluid velocities and shear rates). In our xylem and insect simulations, drag forces acting on hypothetical surface-attached bacteria (dashed oval) are predicted using the flow properties at the locations of the hypothetical bacteria (n_2: fluid velocities and shear rates). The bacteria in this figure are oriented parallel to the flow for the sake of simplicity, but in our microfluidic simulations, the bacterium is oriented perpendicular to flow, as shown in Figure D.3.13.

Drag forces acting on the surface-attached bacteria are composed of both pressure drag (form drag) and skin drag (friction drag), as shown in Figure D.3.10. Pressure drag is

a function of local velocity squared and skin drag is a function of local shear rate (Equations 4, 5). Equation 4 uses the dynamic pressure term of Bernoulli's Equation and Equation 5 is derived from Newton's law of viscosity.

$$F_{pressure\_drag} = \frac{1}{2}\rho A v^2 \quad (4)$$

$$F_{skin\_drag} = \mu A \frac{dv}{dy} \quad (5)$$

F = drag force acting on a surface-attached bacterium

ρ = density of xylem sap

A = area of the bacteria over which pressure drag or skin drag acts

v = velocity of xylem sap

μ = dynamic viscosity of xylem sap

dv/dy = shear rate of xylem sap

Previous studies of bacteria detachment have focused on skin drag when calculating fluid dynamic effects on bacteria[4,30]. This is convenient because calculations are simpler, but our results indicate pressure drag is comparable in magnitude to skin drag at the edge of the precibarial valve during egestion (Figure D.3.12).

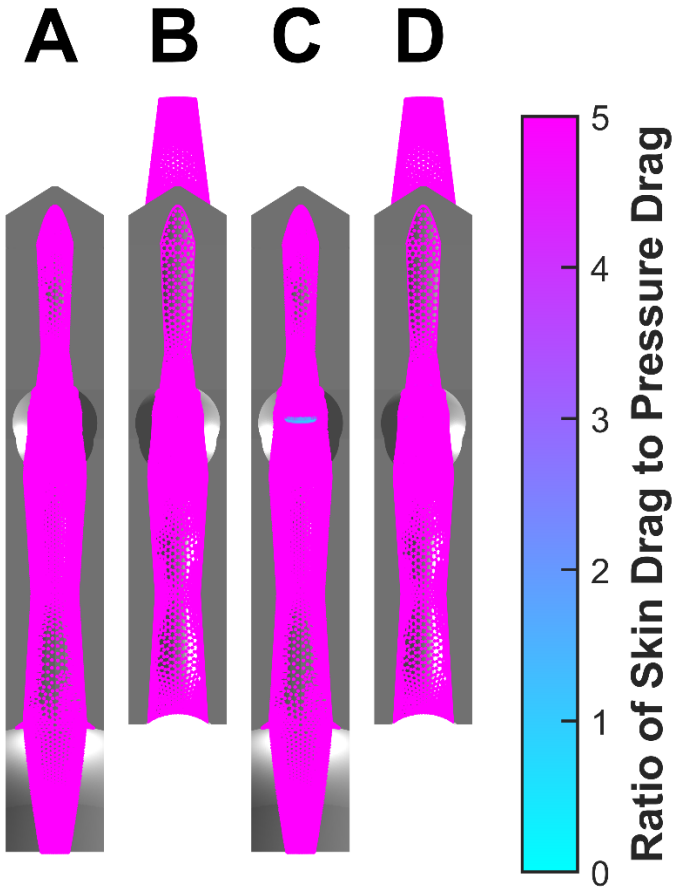

Figure D.3.12 Evaluation of the need for including pressure drag in total drag force calculations. The ratio between skin drag and pressure drag is plotted within gray 3D models of sections of the epipharynx (A & C) and hypopharynx (B & D), which are similar to previously described 3D models[6]. The ratio is generally greater than 5 for both ingestion (A & B) and egestion (C and D), so pressure drag does not have a large effect on total drag force calculations. The ratio is less than 5 at the edge of the precibarial valve during egestion (C), so pressure drag accounts for a relevant portion of the total calculated drag in this region. Pressure drag and skin drag calculations are based on the first and second terms in the fitted equation of Figure D.3.14, respectively.

Fittingly, our drag force calculations for the xylem and insect simulations account for both skin drag and pressure drag, with calculations calibrated based on the work of De

La Fuente et al.[1]. We recreated their microfluidic chamber simulations and our results are within 3% of theirs (Figure D.3.13).

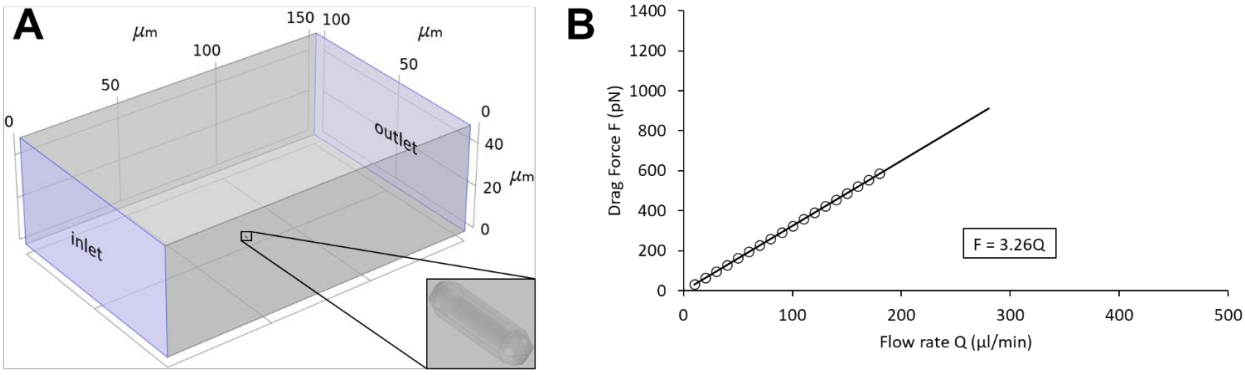

Figure D.3.13 Recreation of the results of De La Fuente et al.[1]. A) The microfluidic chamber fluid dynamic simulation was recreated. It calculates the drag force acting on a surface-attached bacterium at different flow rates. The dimensions of the box (150X100X50 µm), inlet/outlet (blue), and bacterium (0.5X1.9 µm) mimic those of De La Fuente et al.[1]. B) Correlation between drag force (F) and flow rate (Q). Our results are within 3% of the results of De La Fuente et al. based on their equation "F = 3.17Q"[1]. Our results were closest to theirs when the bacteria was oriented perpendicular to the flow (A), so this is the orientation used in our microfluidic chamber simulation.

Our microfluidic chamber simulations were probed for the velocities and shear rates up-stream of the surface-attached bacterium (Figure D.3.13). Correlating upstream flow properties with drag forces allowed us to make predictions of drag forces in xylem and insect simulations without including bacteria in the 3D geometries (Figure D.3.13B).

We were able to estimate answers to this question:

What drag force would a surface-attached bacterium experience if it were at a specific location in the simulation?

Each of the colored dots in Figure D.3.7 and Figure 4.3 represent an answer to this question. Figure D.3.14 and Equation 6 show the correlation between flow properties and drag force.

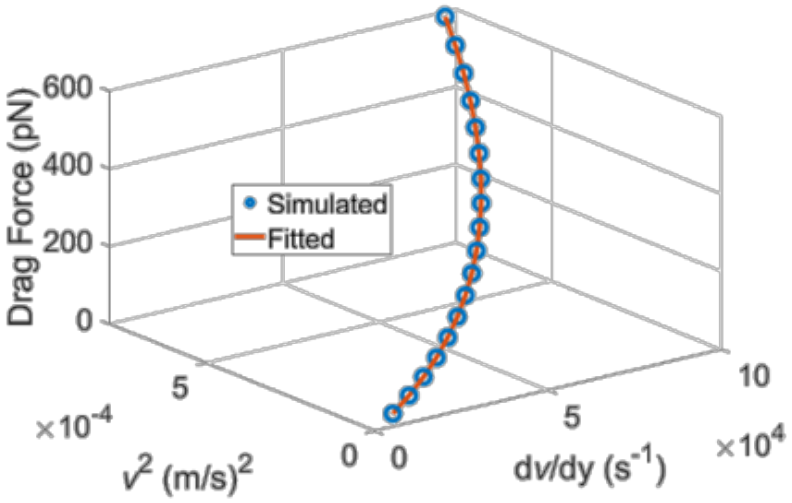

Figure D.3.14 Correlation between flow properties (v^2 and dv/dy) and drag force (F) in our microfluidic chamber simulations. The orange fitted line goes through the blue data point circles, demonstrating a goodness of fit. The equation for the orange fitted line (using SI units) is $F = 506.6621985v^2 + 0.00604035dv/dy$. This equation is given with rounded coefficients in Equation 6 and the variables are defined below.

$$F = 507v^2 + 0.00604\frac{dv}{dy} \quad (6)$$

F = total drag force (N)

v = velocity of xylem sap at 0.2887 µm from wall surface (m/s)

dv/dy = shear rate of xylem sap at 0.2887 µm from wall surface (s^{-1})

Equation 6 relies on probing the velocities and shear rates 0.2887 µm away from the wall surface where the bacterium is hypothetically attached. This distance from the wall was chosen because it allows for a good fit between the data and model in Figure D.3.14

(better than at 0.25 μm or 0.30 μm). It is preferred to probe velocities at this distance from the wall because pressure drag is dependent on squared velocity. Since the bacterium in the simulation is 0.5 μm wide, the average squared velocity is at 0.2887 μm for the xylem simulations and 0.2852 μm for the insect simulations. These numbers are within 2% of each other and are derived below.

Pressure drag force per area ($\hat{F}$) is dependent on squared velocity:

$$\hat{F} = \frac{F_{pressure\_drag}}{A} = \frac{1}{2}\rho v^2 \quad (7)$$

$F_{pressure\_drag}$= pressure drag force from Equation 4

A = area of the bacteria over which pressure drag acts

ρ = density of xylem sap

v = velocity of xylem sap

$\hat{F}$ = pressure drag force per area; this term simplifies the calculation because it avoids addressing the position dependency of A (the area per nanometer increases from the wall [y = 0 μm] to the midline of the bacteria [y = 0.25 μm] and then decreases to the outer edge of the bacteria [y = 0.5 μm]); the validity of this simplification is supported by the fact that 78% of the area per nanometer over which pressure drag acts is not variable with respect to distance from the wall.

Velocity is dependent on distance from the wall and the slip length[31]:

$$v = C_1(y + l) \quad (8)$$

y = distance from the wall

l = slip length specified for a particular simulation

C_1 = shear rate of xylem sap, represented by the letter '*C*' to emphasize its constant nature with respect to distance from the wall in this context (see Table D.3.2).

Plugging Equation 8 into Equation 7:

$$\hat{F} = \frac{1}{2}\rho C_1^2 (y + l)^2 \tag{9}$$

Gathering all constants into a new constant (C_2):

$$\hat{F} = C_2 (y + l)^2 \tag{10}$$

Calculating the average pressure drag force per area ($\breve{F}$):

$$\breve{F} = \frac{\int_0^{y_2} \hat{F}\, dy}{y_2} = \frac{C_2}{y_2} \int_0^{y_2} (y + l)^2 dy \tag{11}$$

y_2 = distance from the wall to the outer edge of the bacteria (0.5 μm)

Integrating:

$$\breve{F} = \frac{C_2}{y_2} \left[\frac{(y + l)^3}{3} \right]_0^{y_2} \tag{12}$$

Evaluating:

$$\breve{F} = \frac{C_2}{3y_2} [(y_2 + l)^3 - l^3] \tag{13}$$

Substituting an expression for $\breve{F}$ based on Equation 10:

$$C_2 (\breve{y} + l)^2 = \frac{C_2}{3y_2} [(y_2 + l)^3 - l^3] \tag{14}$$

$\breve{y}$ = distance from the wall with the average pressure drag force per area

Solving for $\breve{y}$:

$$\breve{y} = \sqrt{\frac{(y_2 + l)^3 - l^3}{3y_2}} - l \tag{15}$$

Solving Equation 15 for the xylem simulations:

$$\breve{y}_{xylem} = \sqrt{\frac{(0.5 + 0)^3 - 0^3}{3(0.5)}} - 0 = 0.2887\ \mu m$$

Solving Equation 15 for the insect simulations:

$$\breve{y}_{insect} = \sqrt{\frac{(0.5 + 0.028)^3 - 0.028^3}{3(0.5)}} - 0.028 = 0.2852\ \mu m$$

An insightful reader might question why the squared velocity profile is central to deciding where fluid properties should be probed, instead of deciding based on shear rate. This question would be reasonable, since skin drag (dependent on shear rate) is generally much larger than pressure drag (dependent on squared velocity) in Figure D.3.12. However, our microfluidic chamber simulations indicate shear rate is effectively independent of distance from the wall within a separation distance of 1 μm (Table D.3.2), so calculated skin drag is effectively independent of probe distance from the wall within this range.

Table D.3.2 Shear rates (s^{-1}) in microfluidic chamber simulations. Shear rates were probed upstream of the surface-attached bacterium at different distances from the wall. This table shows that sheer rate is effectively independent of distance from the wall within a separation distance of 1 µm.

Flow rate	Distance from Wall (µm)							
(µl/min)	0.01	0.1	0.2	0.25	0.3	0.5	0.75	1
10	5387	5387	5387	5387	5387	5276	5277	5277
20	10775	10775	10775	10775	10775	10552	10554	10555
30	16163	16163	16163	16163	16163	15830	15832	15834
40	21552	21552	21552	21552	21552	21107	21110	21113
50	26941	26941	26941	26941	26941	26386	26389	26393
60	32331	32331	32331	32331	32331	31665	31669	31673
70	37721	37721	37721	37721	37722	36944	36949	36954
80	43111	43112	43112	43112	43112	42224	42230	42236
90	48502	48502	48503	48503	48503	47504	47511	47518
100	53893	53894	53894	53894	53894	52785	52792	52800
110	59285	59285	59285	59286	59286	58066	58074	58082
120	64676	64677	64677	64677	64678	63348	63357	63366
130	70069	70069	70069	70070	70070	68630	68639	68649
140	75461	75461	75462	75462	75462	73912	73923	73933
150	80854	80854	80855	80855	80855	79195	79206	79218
160	86247	86247	86248	86248	86248	84478	84491	84503
170	91640	91641	91641	91642	91642	89762	89775	89788
180	97034	97034	97035	97035	97036	95046	95060	95074

Equation 7 is not intended to be a rigorous method for quantifying drag forces acting on surface-attached bacteria. It does not account for the different orientations that bacteria may have with respect to flow direction. However, it provides a means of correlating fluid velocities and shear rates with the detachment of *X. fastidiosa* reported by De La Fuente et al[1].

D.3.4 Water Hammer

The water hammer calculation is based on the fundamental equation of water hammer[32]:

$$\Delta P = \rho a \Delta v \tag{16}$$

ΔP = magnitude of pressure wave, based on an instantaneous valve closure

ρ = density of xylem sap

a = speed of sound in xylem sap

Δv = average velocity of xylem sap (volumetric flow rate divided by cross sectional area)

The density and speed of sound are taken as those of water. The volumetric flow rate is taken as that for ingestion. The cross-sectional area is calculated from a cross-section of the 3D model of the precibarium (Figure D.3.15). Therefore, the maximum pressure spike expected during insect ingestion due to water hammer is overestimated (instantaneous valve closure) as follows:

$$\Delta P = \left(997 \frac{kg}{m^3}\right)\left(1481 \frac{m}{s}\right)\left(\frac{3.37 \times 10^{-11} \frac{m^3}{s}}{1.14 \times 10^{-10} m^2}\right) = 4.36 \times 10^5 Pa = 4.3\ atm$$

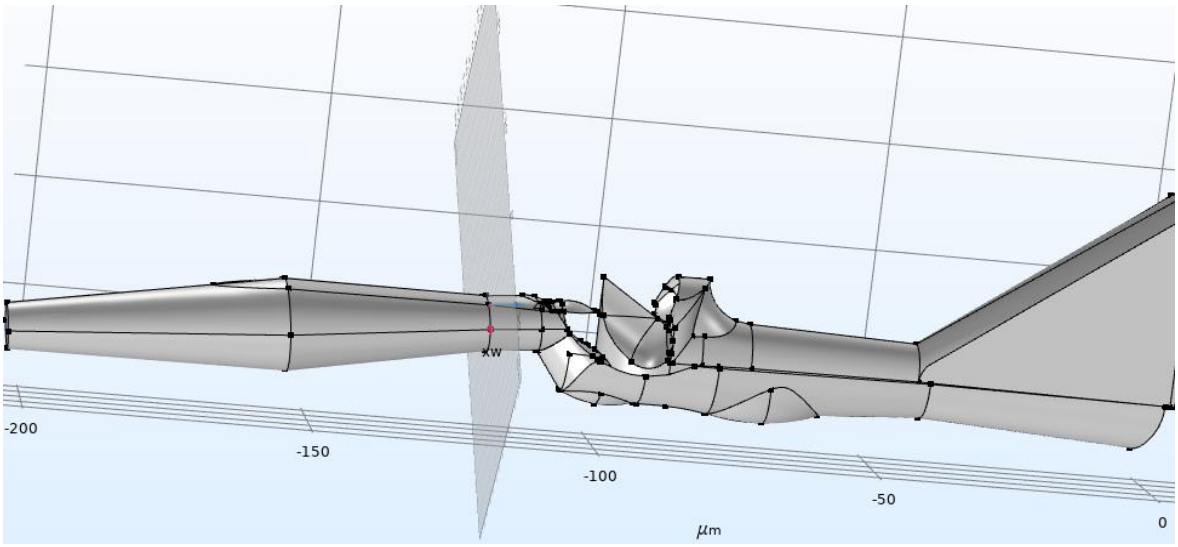

Figure D.3.15 Cross-section of the precibarium used for water hammer calculation. A work plane is shown intersecting the 3D model of the precibarium in COMSOL Multiphysics®. The cross-section represents the area of the precibarial valve that contacts the fluid distal to the valve when the valve is closed.

D.4 References

1 De La Fuente, L. *et al.* Assessing adhesion forces of type I and type IV pili of Xylella fastidiosa bacteria by use of a microfluidic flow chamber. *Appl. Environ. Microbiol.* **73**, 2690-2696 (2007).

2 Carniello, V., Peterson, B. W., van der Mei, H. C. & Busscher, H. J. Physico-chemistry from initial bacterial adhesion to surface-programmed biofilm growth. *Advances in colloid and interface science* (2018).

3 Cervantes, F. A. & Backus, E. A. EPG waveform library for Graphocephala atropunctata (Hemiptera: Cicadellidae): effect of adhesive, input resistor, and voltage levels on waveform appearance and stylet probing behaviors. *Journal of insect physiology* **109**, 21-40 (2018).

4 Boks, N. P., Norde, W., van der Mei, H. C. & Busscher, H. J. Forces involved in bacterial adhesion to hydrophilic and hydrophobic surfaces. *Microbiology* **154**, 3122-3133 (2008).

5 Lovisolo, C. & Schubert, A. Effects of Water Stress on Vessel Size and Xylem Hydraulic Conductivity in *Vitis vinifera* L. *Journal of Experimental Botany* **49**, 693-700 (1998).

6 White, D., Roper, M., & Backus, E. 3D Illustrated Anatomy of Sharpshooter Insect Functional Foregut. (2020 (In Press)).

7 Ranieri, E. *et al.* Fluid Dynamics in the Functional Foregut of Xylem-Sap Feeding Insects: A Comparative Study of Two *Xylella fastidiosa* Vectors. *Journal of Insect Physiology* **120**, 103995 (2020).

8 Holbrook, N. M. & Zwieniecki, M. A. *Vascular Transport in Plants*. (Elsevier, 2011).

9 Fine, R. A. & Millero, F. J. Compressibility of water as a function of temperature and pressure. *The Journal of Chemical Physics* **59**, 5529-5536, doi:10.1063/1.1679903 (1973).

10 Elimelech, M., Gregory, J. & Jia, X. *Particle deposition and aggregation: measurement, modelling and simulation*. (Butterworth-Heinemann, 2013).

11 Liu, C. & Li, Z. On the validity of the Navier-Stokes equations for nanoscale liquid flows: The role of channel size. *AIP Advances* **1**, 032108, doi:10.1063/1.3621858 (2011).

12 Backus, E. A. & McLean, D. L. The sensory systems and feeding behavior of leafhoppers. I. The aster leafhopper, Macrosteles fascifrons Stål (Homoptera, Cicadellidae). *Journal of Morphology* **172**, 361-379 (1982).

13 Bess, E. blue-green sharpshooter (Graphocephala atropunctata) (Signoret, 1854). https://www.forestryimages.org/browse/detail.cfm?imgnum=5495281 (2012).

14 Brodbeck, B. V., Andersen, P. C., Oden, S. & Mizell, R. F. Preference-performance linkage of the xylem feeding leafhopper, Homalodisca vitripennis (Hemiptera Cicadellidae). *Environmental entomology* **36**, 1512-1522 (2014).

15 Stevenson, R. Body size and limits to the daily range of body temperature in terrestrial ectotherms. *The American Naturalist* **125**, 102-117 (1985).

16 Kimball, B. & Bernacchi, C. in *Managed ecosystems and CO2* 311-324 (Springer, 2006).

17 Reicosky, D., Deaton, D. & Parsons, J. Canopy air temperatures and evapotranspiration from irrigated and stressed soybeans. *Agricultural meteorology* **21**, 21-35 (1980).

18 Do, F. & Rocheteau, A. Influence of natural temperature gradients on measurements of xylem sap flow with thermal dissipation probes. 1. Field observations and possible remedies. *Tree physiology* **22**, 641-648 (2002).

19 Andersen, P. C., Brodbeck, B. V. & Mizell III, R. F. Feeding by the leafhopper, Homalodisca coagulata, in relation to xylem fluid chemistry and tension. *Journal of Insect Physiology* **38**, 611-622 (1992).

20 Son, Y., Groves, R. L., Daane, K. M., Morgan, D. J. & Johnson, M. W. Influences of temperature on Homalodisca vitripennis (Hemiptera: Cicadellidae) survival under various feeding conditions. *Environmental entomology* **38**, 1485-1495 (2009).

21 Son, Y. *et al.* Estimation of feeding threshold for Homalodisca vitripennis (Hemiptera: Cicadellidae) and its application to prediction of overwintering mortality. *Environmental entomology* **39**, 1264-1275 (2010).

22 Choi, C.-H., Westin, K. J. A. & Breuer, K. S. Apparent slip flows in hydrophilic and hydrophobic microchannels. *Physics of fluids* **15**, 2897-2902 (2003).

23 Almeida, R. P. & Purcell, A. H. Patterns of Xylella fastidiosa colonization on the precibarium of sharpshooter vectors relative to transmission to plants. *Annals of the Entomological Society of America* **99**, 884-890 (2006).

24 Rapicavoli, J. N. *et al.* O-antigen Modulates Insect Vector Acquisition of the Bacterial Plant Pathogen, Xylella fastidiosa. *Applied and environmental microbiology*, AEM. 02383-02315 (2015).

25 Dellieu, L., Sarrazin, M., Simonis, P., Deparis, O. & Vigneron, J. P. A two-in-one superhydrophobic and anti-reflective nanodevice in the grey cicada Cicada orni (Hemiptera). *Journal of Applied Physics* **116**, 024701 (2014).

26 Holdgate, M. The wetting of insect cuticles by water. *Journal of Experimental Biology* **32**, 591-617 (1955).

27 Chen, L., Zhao, X. & Pan, Y. Establishment of a Standard Method for Boundary Slip Measurement on Smooth Surfaces Based on AFM. *Applied Sciences* **9**, 1453 (2019).

28 Janssen, D., De Palma, R., Verlaak, S., Heremans, P. & Dehaen, W. Static solvent contact angle measurements, surface free energy and wettability determination of various self-assembled monolayers on silicon dioxide. *Thin Solid Films* **515**, 1433-1438 (2006).

29 Lyu, P. *How Do I Compute Lift and Drag?*, <https://www.comsol.com/blogs/how-do-i-compute-lift-and-drag/> (2015).

30 Owens, N. F., Gingell, D. & Rutter, P. R. Inhibition of cell adhesion by a synthetic polymer adsorbed to glass shown under defined hydrodynamic stress. *Journal of cell science* **87**, 667-675 (1987).

31 Jiménez Bolaños, S. & Vernescu, B. Derivation of the Navier slip and slip length for viscous flows over a rough boundary. *Physics of Fluids* **29**, 057103 (2017).

32 Ghidaoui, M. S., Zhao, M., McInnis, D. A. & Axworthy, D. H. A review of water hammer theory and practice. *Appl. Mech. Rev.* **58**, 49-76 (2005).

Appendix E: Overview of Approach to Particle Tracking Simulation Incorporating Surface Interactions

In this dissertation, the foundation of a particle tracking simulation was created for predicting bacteria attachment considering bacteria-surface DLVO interactions (Appendix E). This functionality is not available in COMSOL Multiphysics. Instead, a combination of COMSOL and MATLAB were used for the simulations. 3D fluid dynamic simulations were completed using COMSOL and the resulting velocity fields were exported for use in MATLAB particle tracking functions. The current version of the MATLAB code works by treating bacteria as colloids that are flowing through a rectangular prism. The colloids experience fluid drag, gravity/buoyancy, DLVO forces, and Brownian motion. There are two MATLAB functions: Track and fDLVO.

E.1 Track Function

The code for the Track simulation is as follows:

```
function [DE,FS] = Track(t,z,dh,zs,pc,fr,W,H,c,zi,step)
%% Track
% This function does particle tracking for colloidal particles in a defined
% velocity field.
   % t = duration of simulation (s)
   % z = zeta potential of particle (mV)
   % dh = hydrodynamic diameter of particle (nm)
```

```
    % zs = zeta potential of surface (mV)
    % pc = particle count (number of particles in simulation)
    % fr = flow regime. The current options are 1 (Curved) or 2 (Straight).
            % These are the fluid velocities that
            % were exported from COMSOL.
    % W = width of microfluidic chamber (micrometers)
    % H = height of microfluidic chamber (micrometers)
    % c = concentration of salt (salt molecule is assumed to have one
            % cation and one anion) (mM)
    % zi = valence of ions in symmetrical electrolye (no units)
    % step = step size between DLVO calculations (nm)
% Details on the COMSOL Multiphysics simulation
    % The velocity field (fr) is imported from COMSOL Multiphysics output.
    % It should have only positive x, y, and z coordinates. It's corner
    % should touch the origin, and water should flow in the positive x
    % direction. The only wall should be the bottom and possibly the side
    % surfaces. The y direction should be the width and the z direction
    % should be the height.
%% Set Up the Code
tic % measure time of simulation
% Clear out clutter
    close all
format % Standard number format (not format long)
set(0,'DefaultFigureWindowStyle','docked')
    % Figures are automatically docked when they open.
%% Constants and Variables
mu = 8.9e-4; % viscosity of water (Pa*s)
g = 9.8; % acceleration due to gravity (m/s2)
k = 1.38e-23; % Boltzmann's constant (J/K)
T = 293.15; % Temperature is 20°C (K)
a = dh/2/1e9; % hydraulic radius of particle (m)
rhow = 997; % density of water (kg/m3)
rhop = 4*rhow; % assumed density of particle (kg/m3)
Vp = 4/3*pi*a^3; % volume occupied by particle (m3)
mp = 4/3*pi*a^3*rhop; % mass of particle (kg)
[DLVO,CD] = fDLVO(z,dh,zs,c,zi,step,mp,H); % DLVO Calculations
xi = 6*pi*mu*a; %friction coefficient from p. 79 of "Particle Deposition
    % & Aggregation" (kg/s)
tao = mp/xi;
    % This is the "typical timescale for a single [Brownian] random walk,
    % also known as the relaxation time for the particle's momentum" (s)
        % "Particle Deposition & Aggregation" page 77
h = 0.0000002; % h = time step of simulation (s)
% If the time step is smaller than the colloid relaxation time, then
```

```
% displacement due to brownian motion should be based on the time step, and
% not the relaxation time.
   if h < tao
      tao = h;
   end
P = zeros(round(t/h),9,pc); % holder for particle locations and velocities
   % Data rows are for each time point
   % Data columns are: x y z vx vy vz vxb vyb vzb
      %vxb is the x-component of the instantaneous brownian velocity
      %vyb is the y-component of the instantaneous brownian velocity
      %vzb is the z-component of the instantaneous brownian velocity
   % Each entry in the third matrix dimension is a different particle
% Generate numbers for the Brownian motion
   ktm = 3*k*T/mp;
      % This is the average squared velocity of a Brownian particle. It
      % can be understood by examining equation 4.18 on page 77 of
      % "Particle Deposition & Aggregation." Each translational velocity
      % component has an expected squared velocity of k*T/mp. Using the
      % pythagorean theorem, the squared velocity magnitude is 3*k*T/mp.
      % Ideally, I could improve this calculation by using random numbers
      % and the Maxwell-Boltzmann distribution to give less idealistic
      % velocities for Brownian motion. However, this would also likely
      % come at a large computational cost, since more particles would be
      % needed to find the average outcome.
   sqrtktm = sqrt(ktm); % Expected Brownian particle velocity magnitude
% Load the flow regime (v is a matrix containing component velocities at
% different locations):
   % Before loading the flow regime, complete the following steps:
      % Export u, v, and w as a .txt file with no headers. The columns
         % correspond with x y z vx vy vz. The folder path is
         % L:\CEE\swalker\Lab group materials\DATA\',...
         % 'Daniel\5 Particle Simulations\Velocity Components
      % Rename the file extension from .txt to .csv
      % Open the .csv file and convert the text to columns (use "Text to
         % Columns" button on the "Data Tools" section of the "Data"
         % tab. Use "Space" as the delimiter and check "Treat
         % consecutive delimiters as one." Click finish.
      % Save the file with a .xlsx extension and delete the .csv file.
   % Use the following commands in MATLAB to save the velocity data in
      % matrix form. One benefit of this procedure is to reduce code run
      % time by a half a minute because downloading files from the
      % L-drive is slow.

     % v = readmatrix(['L:\CEE\swalker\Lab group materials\DATA\',...
```

```
    %       'Daniel\5 Particle Simulations\Velocity Components\',...
    %       '1 Curved.xlsx']);
    % save('1 Curved.mat','v')

    % v = readmatrix(['L:\CEE\swalker\Lab group materials\DATA\',...
    %       'Daniel\5 Particle Simulations\Velocity Components\',...
    %       '2 Straight.xlsx']);
    % save('2 Straight.mat','v')
  if fr == 1
     load('1 Curved.mat', 'v')
  elseif fr == 2
     load('2 Straight.mat', 'v')
  end
  % Remove rows in v with "NaN" entries (not a number):
     v(any(isnan(v),2),:) = [];
  % Change position length scale from micrometers to meters:
     v(:,1:3) = v(:,1:3)*1e-6;
  % The velocities are already in the units of m/s.
% Make interpolated functions of the velocity components to make particle
% tracking go smooth:
  vx = scatteredInterpolant(v(:,1),v(:,2),v(:,3),v(:,4));
  vy = scatteredInterpolant(v(:,1),v(:,2),v(:,3),v(:,5));
  vz = scatteredInterpolant(v(:,1),v(:,2),v(:,3),v(:,6));
%% Initial Particle Positions and Velocities
% Create randomized locations for particles at inlet, with y- and z-
% coordinates normalized:
  dist = rand(pc,2);
% Assign particle locations at the inlet:
  P(1,1,:) = 10e-6; % x-coordinates of initial positions (m)
  P(1,2,:) = dist(:,1)*W/4*1e-6; % y-coordinates of initial positions (m)
     % The particles are not close to side walls to avoid calculation
     % for particles bouncing, which is computationally expensive.
     % Otherwise, particles could drift into space where fluid
     % velocities are unspecified.
  P(1,3,:) = dist(:,2)*H/12*0*1e-6 + a + 0.25*100e-9;
     % z-coordinates of initial positions (m).
     % The particles are not close to top to avoid calculation for
     % particles bouncing, which is computationally expensive.
     % Otherewise, particles could drift into space where fluid
     % velocities are unspecified. The particles are at least far enough
     % away from the bottom to avoid DLVO interactions.
% Assign particle velocities at the inlet:
  P(1,4,:) = vx(P(1,1,:),P(1,2,:),P(1,3,:));
  P(1,5,:) = vy(P(1,1,:),P(1,2,:),P(1,3,:));
```

```
    P(1,6,:) = vz(P(1,1,:),P(1,2,:),P(1,3,:)) - Vp*g*(rhop-rhow)/xi;
        % This makes the beginning of the simulation go more smoothly by
        % setting the initial particle velocity based on the balance
        % between gravity, buoyancy, and drag force. Otherwise, the stiff
        % drag force equation could yield chaotic results with progressive
        % iterations.
%% Move and Track Particles
% Progress the particle along it's path at each time step:
for i = 2:round(t/h)
    % Generate randomized brownian motion (relative component velocities)
        % Generate coeffiecents that distribute motion randomly among the
        % coordinate axes:
            rando = rand(pc,3); % random numbers between 0 and 1
            random = rando./sum(rando,2);
                % Coefficients of squared velocities that add to make 1
            coefficients = sqrt(random);
        % Generate -1 or 1 to make component motion negative or positive:
            d = round(rand(pc,3)) + 1; % Randomly generate a 1 or 2
            options = [-1 1]; % velocites can positive or negative
            direction = options(d); % Randomly choose positive or negative
        Brownian = coefficients.*direction*sqrtktm; % Brownian velocities
        P(i-1,7:9,:) = Brownian'; % Brownian velocities
    % Move the particle based on the velocity in the last time step and
    % brownian motion:
        P(i,1:3,:) = P(i-1,1:3,:) + P(i-1,4:6,:)*h + P(i-1,7:9,:)*tao;
            % This type of brownian motion calculation only moves the
            % particle by a small amount, so it shod be fine. For a 1 um
            % particle, it moves 0.6 nm in a given time step and smaller
            % particles move smaller distances. Unfortunately, this method
            % fails to account for how a DLVO energy barrier would affect
            % the motion. Still 0.6 nm is a small distance, so this should
            % be fine.
    % Don't let the particle pass through a wall (bottom wall):
        m = find(P(i,3,:) < 0 + a + 0.2e-9); % find indices of ghost particles
        P(i,3,m) = P(i-1,3,m); % reverted back to previous position
        P(i-1,6,m) = -0.5*P(i-1,6,m); % Inelastic collision
    % Adjust the x-component of the particle velocity based on the previous
    % velocity and fluid drag (but not Brownian motion):
        P(i,4,:) = squeeze(P(i-1,4,:))... % Previous velocity
            + xi*(squeeze(vx(P(i-1,1,:),P(i-1,2,:),P(i-1,3,:))) - squeeze(P(i-
1,4,:)))/mp*h; % Fluid drag
            % The drag force is based on equations 4.31 and 4.33 on page 79
            % & 81 of "Particle Deposition & Aggregation." Calculated drag
            % is based on the motion of a single unbound hard/soft sphere.
```

```
            % The calculation takes a combined approach based on the
            % methods for hard and soft spheres. It uses the hydraulic
            % radius associated with a soft sphere, but ignores dipole
            % effects, since "the reduction due to dipole field usually
            % amounts, at most, to a few percent" (page 82).
    % Adjust the y-component of the particle velocity based on the previous
    % velocity and fluid drag (but not Brownian Motion):
        P(i,5,:) = squeeze(P(i-1,5,:))... % Previous velocity
            + xi*(squeeze(vy(P(i-1,1,:),P(i-1,2,:),P(i-1,3,:))) - squeeze(P(i-
1,5,:)))/mp*h; % Fluid drag
    % Adjust the z-component of the particle velocity based on the previous
    % velocity, fluid drag, gravity/buoyancy, and DLVO Forces (but not
    % Brownian Motion)
        vz1 = squeeze(P(i-1,6,:)); %Previous velocity
        vz2 = xi*(squeeze(vz(P(i-1,1,:),P(i-1,2,:),P(i-1,3,:))) - squeeze(P(i-
1,6,:)))/mp*h; % fluid drag
        vz3 = (rhow/rhop-1)*g*h; % gravity/buoyancy
        vz4 = DLVO(round((squeeze(P(i,3,:))-a)/(step*1e-9))+1)'*h; % DLVO
        P(i,6,:) = vz1 + vz2 + vz3 + vz4;
% disp(['Time to complete time step # ' num2str(i) ':'])
% toc
end
%% Particle Slide --> Particle Stick
% If the particle has been close to a wall/surface for 100 time steps,
    % assume it attaches to the wall and therefore, change it's position to
    % make it stationary:
PS = squeeze(P(:,3,:)); % z-coordinates over time for each particle
PS1 = PS < 1e-9 + a; % Find where particles are within 1nm of wall.
PS2 = movmean(PS1,[99 0],1); % Take averages over 100 time steps
PS3 = PS2 == 1; % Find where particle is close to wall for 100 steps
PS3(1:99,:) = 0; % Ignore the first 99 time steps
[PS4,PS5] = find(PS3);
for i = 1:length(PS4) % Make sliding particles stationary
    P(PS4(i):end,1,PS5(i)) = P(PS4(i),1,PS5(i));
    P(PS4(i):end,2,PS5(i)) = P(PS4(i),2,PS5(i));
    P(PS4(i):end,3,PS5(i)) = P(PS4(i),3,PS5(i));
end
%% Deposition Efficiency
% Count the number of particles that have an opportunity to interact with
% the surface
    Collisions = sum(squeeze(P(:,3,:)) < a+CD);
    CountCollisions = sum(Collisions > 0); % # of collisions
    CountBoth  = sum(P(end,3,:) < a+CD); % # of depositions
    CountPrimary = sum(P(end,3,:) < a+1e-9); % # of primary depositions
```

```
    CountSecondary = CountBoth - CountPrimary; % # of 2ndary depositions
    DE = CountBoth/CountCollisions; % Deposition Efficiency
    FS = CountSecondary/CountBoth; % Fraction Secondary
%% Clean Up the Code
set(0,'DefaultFigureWindowStyle','normal')
toc % measure time of simulation
end
```

E.2 fDLVO function

The Track function calls the function fDLVO, which is as follows:

```
function [DLVOacceleration,CD] = fDLVO(z,dh,zs,c,zi,step,mp,H)
%DLVO This function calculates the forces for spere-plate interactions.
    % z = zeta potential of particle (mV)
    % dh = hydrodynamic diameter of particle (nm)
    % zs = zeta potential of surface (mV)
    % c = concentration of salt (salt molecule is assumed to have one
            % cation and one anion) (mM)
    % zi = valence of ions in symmetrical electrolye (no units)
    % step = step size between DLVO calculations (nm)
    % These parameters are specifically for making the function compatible
        % with the function "Track" (particle tracking simulation):
        % mp = mass of particle (kg)
        % H = height of microfluidic chamber (micrometers)
%% Electrical Double Layer Repulsion
% Simple Parameters
    a = dh/2*1e-9; % Particle radius (m)
    sd = (0:step:100)*1e-9; % separation distance (m)
    Psi = z/1000; % approximated surface potential of colloid (V)
    PsiSurf = zs/1000; % approximated surface potential of surface (V)
% Debye-Huckel parameter: kappa (inverse debye length)
    e = 1.6e-19; % Elementary charge (C)
    T = 293.15; % Temperature is 20°C (K)
    k = 1.38e-23; % Boltzmann's constant (J/K)
    N = 6.022e23; % Number of ions in a mol (no units)
    epsilon_0 = 8.854e-12; % Permitivity of vacuum (C/[V*m])
    epsilon_r = 80; % Relative permitivity of water (no units)
        % Note to self: This is okay for water around 20°C and 0-30 mM KCl
    epsilon = epsilon_r*epsilon_0; % Permitivity of water (C/[V*m])
    C = c; % concentration of salt (mol/m3)
    kappa = sqrt(e^2*N*2*C*zi^2/(epsilon*k*T));
```

```
        % inverse debye length (m-1)
        % Equation 2.13 from "Particle Depostion & Aggregation" textbook
% Electrical Double Layer Repulsion (EDL)
    E1 = epsilon*a/4; % first portion of EDL equation
    E2 = 2*Psi*PsiSurf; % second portion of EDL equation
    E3 = log((1+exp(-kappa*sd))./(1-exp(-kappa*sd))); % third portion
    E4 = Psi^2 + PsiSurf^2; % fourth portion
    E5 = log(1-exp(-2*kappa*sd)); % fifth portion
    EDL = E1*(E2*E3+E4*E5); % EDL repusion potential energy (J)
        % Equation 21 from "Mutual Coagulation of Colloid Dispersions"
            % (Hogg et al. (1966)). The plate was approximated by making
            % one of the radii approach infinity. The (Psi^2 + PsiSurf^2)
            % was distributed into the brackets.
        % Conditions for validity of equation 21:
            % "Double layer thickness is small compared to particle size."
                % good for a > 10/kappa and "not too bad" for a > 5/kappa
            % Zeta potentials less than 25 mV. Good approximation for zeta
                % potentials less than 50 - 60 mV. By this point, there is
                % strong repulsion anyway.
            % Separation distance is much smaller than particle radius.
                % h^2/a^2 < 0.0975    (I made this up)
    edl = EDL/(k*T); % EDL repulsion potential energy (kT)
%% Van der Waals Attraction
lambda = 100e-9; % Dielectric wavelenth (m)
    % Dielectric wavelength is called the characteristic wavelength of
    % the dispersion interaction on p. 74 of "Particles in Water" by J.
    % Gregory. It "can generally be assumed to be of the order of 100
    % nm."
A = 0.2e-20; % Hamaker constant (J)
    % On page 47 of "Particle Depositin & Aggregation", it says this:
    % "For practically all aqueous dispersions, Hamaker constants lie
    % in the range 0.3-10X10^-20 J. Dense mineral particles have values
    % towards the upper end of this range, whereas low-density,
    % especially biological, materials have quite low values."
VDW = -A*a./(6*sd)./(1 + 14*sd/lambda); % Van der Waals Potential (J)
    % Equation 19 from "Approximate Expressions for Retarded van der Waals
    % Interactions" (Gregory (1981)). It "can be used up to separations of
    % about 20% of the sphere radius." For greater separation distance, use
    % Equation 12 (don't use Equation 12 for "interaction at close
    % approach").
vdw = VDW/(k*T); % Van der Walls Attraction Potential Energy (kT)
%% Overall DLVO Calculation
dlvo = vdw + edl; % Interaction Energy (kT)
DLVO = VDW + EDL; % Interaction Energy (J)
```

```
%% Custom Code for Particle Tracking
dDLVO = -gradient(DLVO,step*1e-9); % DLVO force (N)
aDLVO = dDLVO/mp; % Total acceleration enacted on particle by DLVO (m/s2)
DLVOacceleration = [aDLVO zeros(1,H*1000/step)]; % DLVO effect at large
   % separation distances is negligible.
% Find the separation distance that will be used to specify that a particle
% collided with the surface (and that the particle was retained)
   ISRA = find(aDLVO == max(aDLVO)); % Index of strongest repulsive
acceleration
   ICD = find(aDLVO == min(aDLVO(ISRA:end))); % Index of collisiondivide
   CD = sd(ICD) + step*1e-9; % Location of collision divide
end
```

E.3 Undergraduate Summer Research Project

There is still plenty of room for improvement with this code. It could serve well for an undergraduate student summer research project if the COVID-19 pandemic limits laboratory visits. Here is a description of a such a project:

Prerequisites:

- Comfortable with programming in MATLAB.
- Talent for chemistry/physics.
- Access to the book titled “Particle Deposition and Aggregation: Measurement, Modeling, and Simulation.”
- Access to a fluid dynamic simulation software (optional).

Project timeline:

1. Literature Review: 2.5 weeks
    a. What is classic DLVO theory?
    b. Familiarize yourself with the MATLAB functions Track and fDLVO.

c. Under what conditions does classic DLVO theory provide good predictions for particle attachment?
d. In what situations would particle tracking with DLVO interactions included be useful?
e. Who else has published work with DLVO-informed particle tracking simulations? What are strengths and limitations of those simulations?
f. How do those strengths and limitations compare to the current versions of Track and fDLVO? What are three ways that the code can be improved to make it more useful or novel?

2. Networking: 1 week
    a. Select three established scientists in addition to Dr. Walker that could provide valuable feedback on the findings of your literature review and the merits of your potential project ideas (some ideas are provided below).
    b. Ask Dr. Walker if she can connect you with scientists for some dialogue.
3. MATLAB Improvement – Choose one or more of the following or choose your own path: 3 weeks
    a. Make the simulation applicable to custom geometries with irregularly-shaped surfaces. The code is currently only applicable to simulations of fluid flow in rectangular prisms with some other constraints.
    b. Enhance the code so that it can be run using cluster computing.

c. Incorporate extended DLVO calculations into the code.

d. Use the Maxwell Boltzmann distribution to give the particles a distribution of Brownian velocities. The duration of the Brownian walks (tao) could also be given a distribution.

e. Make sure the simulation step size is small enough to avoid particles magically becoming unstuck from walls when they bounce off of the walls.

f. Account for the fact that particle velocity should be adjusted when the particle jumps across a region where DLVO forces matter (because Brownian motion doesn't account for DLVO barriers).

g. Consider incorporating a fluid drag force correction factor that accounts for the particle's distance from a wall (λ, see Table 4.2 on page 80 of the textbook titled "Particle Deposition & Aggregation"*)*.

4. Research presentation: 1 week

    a. Create a research poster to present your work.